Some aspects of the

Atlantic ocean circulation

Rezwan Mohammad

Department of Meteorology
STOCKHOLM UNIVERSITY, 2005

Some aspects of the

Atlantic ocean circulation

Rezwan Mohammad

Department of Meteorology
STOCKHOLM UNIVERSITY, 2005

Some aspects of the Atlantic ocean circulation
Rezwan Mohammad

ISBN 91–7155–047–X, pp. 1–23

Doctoral thesis
Doctoral dissertation May 20, 2005

Stockholm University
Department of Meteorology
SE–106 91 Stockholm
Sweden

Typeset by LaTeX
Printed by Duvbo tryckeri AB
Stockholm 2005

Abstract

The present thesis deals with the ocean circulation from two viewpoints: *Pro primo*, the dependence of the global thermohaline ocean circulation (THC) on the parameterization of the small-scale vertical mixing processes in the interior of the ocean, and, *pro secundo*, the dynamics of the circulation in the Nordic Seas. The THC is found be crucially dependent on the parameterization of the small-scale vertical mixing, two types of which have been compared: The commonly used constant diffusivity and a, physically more plausible, stability-dependent parameterization. For constant diffusivity the circulation weakens when the equator-to-pole surface density difference is decreased, consonant with commonly held prejudices. However, for stability-dependent diffusivity the circulation is enhanced. This conclusion has been reached using two investigative techniques, viz. a scale analysis as well as a numerical zonally-averaged and equatorially symmetric THC model. However, if asymmetric flows are considered, the dynamics become more complex to interpret. It has, nevertheless, been concluded that when the degree of asymmetry of the surface-density distribution is taken to be fixed, the response of the circulation to changes of the surface-density distribution corresponds to that from the symmetric investigation.

The studies of the Nordic Seas are mainly based on satellite-altimetric data providing Sea-Level Anomalies (SLAs). These are utilized to estimate the seasonal cycle as well as the inter-annual variability of the depth-integrated flows. The seasonal cycle is examined using the winter-to-summer difference of the barotropic flow, with focus on the entire region as well as on two sections extending from a common point in the central Norwegian Sea to Svinøy on the Norwegian coast and to the Faroe Islands, respectively. The total barotropic transport is estimated to be around 10 Sv larger during winter than in summer, of which 8 Sv are associated with the barotropic re-circulation gyre in the interior of the Norwegian Sea, the remainder being linked to the Atlantic inflow across the Iceland-Scotland Ridge. The inter-annual variability of the circulation in the Nordic Seas is investigated on the basis of a theoretical analysis permitting independent calculation of the barotropic flow along closed isobaths using SLA data as well as wind data. The barotropic flow based on SLA data is found to co-vary with the flow estimated using wind data.

Preface

I have hard to believe that seven years at MISU have been passing so quick, two years as an undergraduate student and almost five more years as graduate student. The PhD studies at MISU has been very educative and the scientific atmosphere is very inspiring.

Many colleagues have been contributing to this work with their ideas, comments and discussions, and of course, the first ones I think of are my supervisors Johan Nilsson and Peter Lundberg. Johan has given me all his support and encouragement and most important a stimulation to broaden my scientific mind. This thesis have not been what it is today without your constructive ideas. I would like to give you all the credits and acknowledge possible. Peter Lundberg has always been supporting me with his cheering words (especially when the situation was somewhat dubious), his great sense of humor and not at least his guidance for considering things in a wider perspective. Furthermore, I am very grateful for your effort to improve my english language.

I would also like to take the opportunity to thank Thomas Rossby, Jonas Nycander, Göran Broström, Peter Sigray and Branko Grisogono for valuable comments and interesting discussions.

Birgitta, Birgitta, Pat and Solveig have always been willing to help me out from troubles. A special thank to Eva Tiberg who sorted out administrative things for me. Michael Burger has patiently been answering all my stupid computer questions and Janne, Leif and Nils have been helping me with practical things since I am all fingers and thumbs. Ulla Hammarstrand has arranged that I have been given the chance to teach which I really appreciate, specially the laborative exercises in Numerical methods and Baroclinic instability.

Then a big thanks to all PhD students for your support. My room mates Jenny Nilsson, Greger Bengtsson, Anne Kubin and Henrik Ernstson: Thank you all for endless and encouraging discussions about everything and nothing. Also thanks to Radovan Krejčí for the encouraging slap on my back.

And I do not want to forget to mention my cultivated lunch company including Johan, Jonas, Göran and Anders Engqvist leaded by Kristofer Döös. You made the food of Lantis taste much better.

At last my poor family and friends who have given all their support and patience when I had to spend my time in front of the computer instead of socializing together with them. A lot of gratitude to all of you.

আমি আমার এই কাজটি আমার শ্রদ্ধেয় মা রেহানার প্রতি উৎসর্গ করছি। তুমি, যে এই কাজটি সম্পন্ন করতে আমাকে শক্তি, সাহস ও প্রেরণা যুগিয়েছ। যে তুমি আমাকে বুঝতে শিখিয়েছ যে পৃথিবীতে অসম্ভব বলে কিছু নেই।

List of papers

PAPER I **The role of diapycnal mixing for the equilibrium response of thermohaline circulation**

REZWAN MOHAMMAD AND JOHAN NILSSON

Ocean Dynamics, 2004, **54**(1), 54–65

PAPER II **Symmetric and asymmetric modes of the thermohaline circulation**

REZWAN MOHAMMAD AND JOHAN NILSSON

Under review in Tellus, Series A

PAPER III **An altimetric study of the Nordic-Sea region seasonal cycle**

REZWAN MOHAMMAD, JOHAN NILSSON AND PETER LUNDBERG

Under review in Deep Sea Research Part I

PAPER IV **Inter-annual variability of the along-isobath flow in the Norwegian Sea**

REZWAN MOHAMMAD

Stockholm University, Department of Meteorology, DM-report 94, 2005

Thesis summary

1 Introduction

Over the last decades the global thermohaline circulation (THC) has attracted ever-increasing scientific attention. This is due to its importance for the global climate, where the meridional overturning plays a significant role for evening out the global radiative imbalance between the equatorial and the polar regions. Paleo studies show, however, that over geological time-scales considerable climate fluctuations have taken place (as exemplified by e.g. the presence of tropical fossils in the Arctic), to a considerable extent associated with changes of the THC.

The focus of the present thesis dealing with the thermohaline circulation will primarily be on the Atlantic Ocean. This is partly because of the importance of the North Atlantic THC for the climate of Western Europe, but also since the Atlantic is the most comprehensively investigated ocean basin, having been subjected to wide variety of field surveys as well as theoretical studies.

The first systematic oceanographic investigation of the Atlantic (Thomson, 1878) was thus undertaken in connection with the R/V Challenger expedition 1873–1876, generally regarded as the ground-breaking event which launched the modern biological, chemical as well as physical ocean sciences. Although neither reversing thermometers nor standardized techniques for determining sea-water salinity had been developed at this time, ingenious use of maximum-minimum thermometers made it feasible for the Challenger scientists to measure reasonably accurate vertical temperature profiles down to great depths. Fig. 1, reproduced from a rarely encountered study due to Wild (1877), thus shows the observed north-south vertical temperature distribution along approximately the 30°W meridian in the Atlantic. Already in this early representation we recognize the cold- and warm-water spheres of the ocean, the latter in modern oceanographic mod-

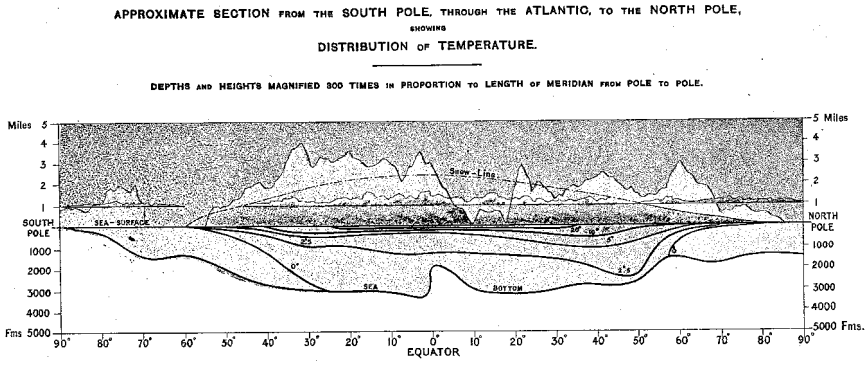

FIGURE 1: Atlantic temperature section, reproduced from Wild (1877).

elling jargon commonly denoted the thermocline.

Around fifty years later (Spieß, 1928) the first comprehensive "modern" oceanographic survey of the Atlantic (in particular its southern parts) was carried out in 1925–1927 by the R/V Meteor, equipped with Nansen bottles, reversing thermometers, titration apparatus for determining sea-water salinity, and, not least important, an echosounder for bathymetric observations. (Note, incidentally, that use of this recently perfected technical device lead to the discovery of the Mid-Atlantic Ridge.) This two-year cruise established the overall features of the Atlantic hydrography more-or-less as we know them today, cf. the meridional salinity section along 30°W in Fig. 2.

Since these pioneering investigations considerable scientific development, has, however, taken place. This holds true not least as regards theoretical modelling, a topic which in the present thesis is pursued in papers I and II. These two investigations, based on a simplified two-dimensional representation of the ocean, deal with the large-scale features of the Atlantic thermohaline circulation, particularly how the meridional transports and the thermocline characteristics are affected, and even controlled, by the internal mixing in the ocean.

The idealized two-dimensional rectangular basin which was used to represent the Atlantic for modelling purposes is, however, not altogether appropriate. The meridional circulation is in reality subject to a number of topographic constraints. One of the most important of these is exerted by the Greenland-Scotland Ridge, across which the comparatively warm and high-saline North Atlantic surface waters must pass on their way to the convection areas in the Nordic Seas. In this region wintertime atmospheric

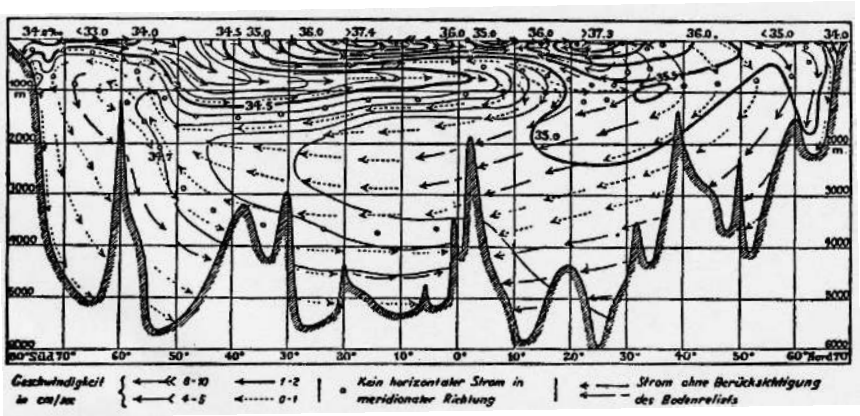

FIGURE 2: Atlantic salinity section as deduced by Merz and Wüst (Spieß, 1928).

cooling leads to the production of dense deep water, which ultimately closes the global "conveyor belt" by making its way southward into the Atlantic proper, mainly via the Faroe-Bank Channel and the Denmark Strait.

The transport of North Atlantic surface waters into the Nordic Seas is not only responsible for maintaining the present climate of Western Europe, it is also crucial for the viability of commercially important fish stocks. This latter feature to a considerable extent explains why systematic oceanographic investigations of the Atlantic inflow as well as of the hydrographic conditions in the Nordic Seas began well over a hundred years ago. The pioneering efforts were made during the 1876–1878 R/V Vøringen expedition (Mohn, 1885, 1887) focusing on the Norwegian Sea. The Greenland and Iceland Seas were surveyed during the R/V Sofia and R/V Ingolf expeditions in 1883 and 1894–1895, respectively (Nordenskiöld, 1885; Knudsen, 1899).

Standardized techniques were at this time coming into use for hydrographic observations; other investigations were, however, still carried out in a rather makeshift fashion, hence Nordenskiöld (1885) classical account of an attempted drifter experiment during the R/V Sofia expedition:

> *"... Under det att Sofia ångade fram i det härliga vädret på den mellan Färöarnas höga klippsträndер alldeles stilla sjön, tömde några af oss på däck en flaska af en ypperlig madera, som herr William Schönlank i Berlin förärat expeditionen. Såsom vid dylika tillfällen ofta plägar ske, kastades den tömda flaskan*

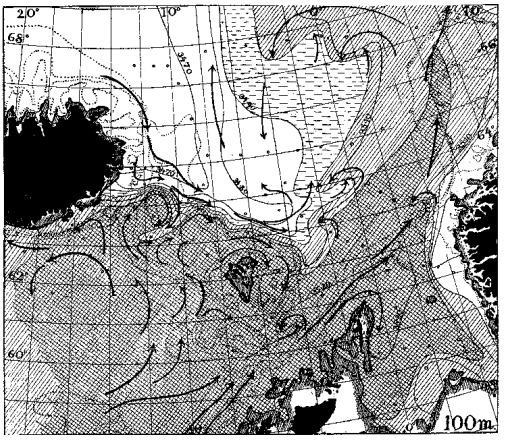

FIGURE 3: Surface currents in the southern Norwegian Sea (Helland-Hansen and Nansen, 1909).

> *öfver bord, sedan den åter blifvit korkad och några visitkort med helsningar m.m. i densamma inlagda. Denna gång inträffade det mindre vanliga, att flaskan dref oskadad i land . . . "*

The first comprehensive overview of the hydrography as well as the circulation of the Norwegian Sea was, however, provided by Helland-Hansen and Nansen (1909) on the basis of their field investigations in 1904–1905. The overall analysis and description of the oceanographic conditions which these investigators presented still holds true to a remarkably high degree. As an example hereof it is well worth underlining that the main characteristics of the surface-current distribution in the southern Norwegian Sea Fig. 3 proposed by Helland-Hansen and Nansen (1909) still remain valid today, i.e. after almost a full century. This is particularly noteworthy in view of the fact that recording current meters did not enter the arsenal of the field oceanographer until the early 1960s.

A more recent addition to the presently available battery of observational methods is satellite altimetry, whereby the sea-surface topography can be directly observed. Papers III and IV of the present thesis thus deal with the practical application of this technique to examine the barotropic transports in the Nordic Seas, with particular reference to the possibility of quantifying the Atlantic inflow in the Faroe region as well as examing the recirculation taking place in the interior of the Norwegian Sea. In view of the varied methodological approaches to oceanographic problems

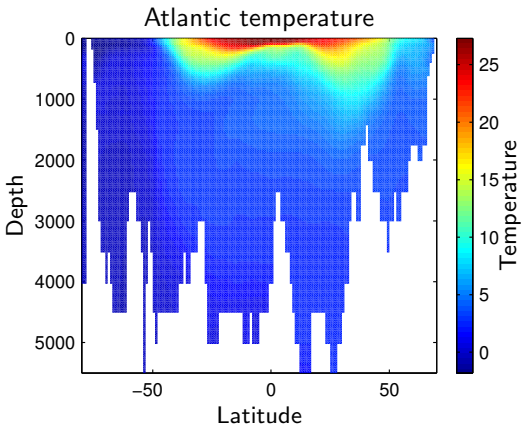

FIGURE 4: Atlantic vertical temperature section along 30°W.

outlined above, it has, as presumably will become evident in what follows, been concluded by the present author that the most constructive forward path lies in the judicious application of a pragmatic combination of the different techniques.

2 Model studies

The fully modern picture of the Atlantic hydrography emerged when Conductivity-Temperature-Depth (CTD) probes came into widespread use around 30 years ago. As an example of what has been accomplished using these fully modern observational techniques, Fig. 4 shows the present-day image of the thermal stratification characterizing a meridional NS section extending along the the Atlantic. The recent advances in our knowledge are particularly keenly appreciated when a comparison is made with Fig. 1 and 2, representing the current insights available in the 1880s and 1920s, respectively.

Not least due to these observational advances, numerical modelling of the ocean circulation has come to play an increasingly important role for climate predictions such as the ones advanced by the Integovernmental Panel on Climate Change (IPCC). It must, however, be kept in mind that the ocean models which this august body espouses are comprehensive and three-dimensional with the attendant advantages concerning resolution and inclusion of various processes. Nevertheless it is not given *a priori* that cru-

cial physical processes are correctly represented. A prime example hereof is the parameterization of the internal small-scale vertical mixing in the ocean interior, which generally is formulated in a rather conventional terms. In order to test the effects of more subtle parameterizations it proves convenient to base the investigations on meridionally averaged models, particularly in order to reduce ambiguities when interpreting the model results.

During the last two decades there has been a wide-spread interest in issues concerning the thermohaline circulation and a number of simplified models have been used to study its fundamental properties (e.g. Bryan, 1986; Marotzke et al., 1988). Papers I and II of the present thesis are based on a zonally averaged two-dimensional numerical thermohaline model similar to the ones used in previous studies focusing on an idealized model basin (Wright and Stocker, 1991; Rahmstorf, 2000). The model is used to study the rôle of small-scale vertical mixing for the symmetric and asymmetric circulation modes. The model is forced thermally as well as by mixed boundary conditions. The thermal forcing is a symmetric restoring surface temperature with cooling in the polar regions and heating in the tropics. Mixed boundary conditions imply that the model system is forced thermally as well as by a freshwater flux, the latter represented by a prescribed symmetric surface salinity flux with precipitation in the polar regions and evaporation in the tropics. The surface salinity flux is associated with the atmospheric meridional transport of water vapor.

Before examining the model studies constituting papers I and II of the present thesis, it is important to underline that for the symmetric modes of the thermohaline circulation the dynamics can be described on the basis of classical thermocline scaling (Welander, 1986). Here the key quantities are the equator-to-pole surface density difference, $\Delta\rho$, and the small-scale vertical mixing, κ. For the latter quantity, the dynamical effects of two different assumptions of the physical nature of the small-scale vertical mixing are compared: (1) constant diffusivity, which is frequently used in ocean-circulation models and (2) the more physically plausible parameterization where the rate of energy supplied for the mixing is constant, implying that the diffusivity is dependent on the stability (e.g. Huang, 1999; Nilsson and Walin, 2001). The analysis suggests that the thermocline depth scales as $H \sim \kappa^{1/3} \cdot \Delta\rho^{-1/3}$ and the strength of the circulation as $\psi \sim \kappa^{2/3} \cdot \Delta\rho^{1/3}$. For constant diffusivity this implies that the relation between the strength of the circulation and the equator-to-pole density difference is $\psi \sim \Delta\rho^{1/3}$. Assuming that the mixing energy is constant, the diffusivity is dependent on the vertical stratification. The parameterization of the vertical mixing presented in the appended paper is $\kappa \sim \Delta\rho^{-1}$, indi-

cating that $\psi \sim \Delta\rho^{-1/3}$. Numerical results from a zonally and equatorially symmetric two-dimensional as well as a three-dimensional model (Nilsson et al., 2003), corroborate the outcome of the scale analysis. Hence, the response of the circulation is fundamentally different for the two parameterizations of the mixing: When the equator-to-pole density difference increases, the circulation is amplified for constant diffusivity, whereas it weakens for stability-dependent diffusivity. As will be seen, however, the results for equatorially asymmetric circulations are more subtle. The results from the symmetric-flow scale analysis do not apply for asymmetric flows and the corresponding model results do not, at first glance, point in the same direction as those from the symmetric case.

2.1 The symmetric mode

Paper I focuses on the parameterization of the small-scale vertical mixing. How this is done proves to be crucial for the response of the THC to changes of the equator-to-pole surface temperature gradient and the atmospheric meridional freshwater transport, these two quantities being the dominating external factors affecting the THC.

The commonly held view of the THC response is that a more pronounced equator-to-pole surface density gradient results in a stronger circulation. Increased freshwater forcing curtails the density gradient and, consequently, also the circulation. This argument is, however, dependent on how the parameterization of the small-scale vertical mixing is undertaken. Our knowledge of these processes in the interior of the ocean is poor, and hence the vertical mixing is commonly assumed to be fixed and independent of the density stratification. However, a more physically reasonable assumption is that the mixing (and thus also the diffusivity) is suppressed by a strong stratification and that the diffusivity increases as the stratification becomes weaker.

Nilsson and Walin (2001) found that if the diffusivity is assumed to be stability-dependent, the circulation is enhanced by a weaker equator-to-pole density difference caused by the surface salinity flux. This result contradicts generally held views and thus deserves further consideration.

Paper I pursues this line of inquiry on the basis of scale analysis as well as a simple zonally averaged numerical thermohaline circulation model. Since a one-hemisphere basin is employed, the study is restricted to equatorially symmetric circulations.

The following highly simplified picture of the THC underlies the scale analysis: A thin warm-water layer floats above dense deep water (cf. Fig. 4).

The warm water of low density spreads from the tropics towards the poles, where it cools and hereby assumes a higher density. In some well-localized areas the water becomes sufficiently dense to sink, hereby forming deep water. This flows back through the deep ocean towards lower latitudes, where it eventually up-wells and transgresses the thermocline on its way towards the surface. (In the World Ocean this circulation is, in fact, asymmetric with respect to the equator. In paper I this feature is neglected for reasons of simplicity, whereas the skewness will be taken into account in paper II.)

The scale analysis, together with the frequently used assumption that the diffusivity is constant, implies that the strength of the circulation scales as $\psi \sim \Delta\rho^{1/3}$. On the other hand, if the production rate of potential energy available for small-scale mixing (from e.g. winds and tides) is taken to be constant, which is a physically more plausible assumption, the THC scales as $\psi \sim \Delta\rho^{-1/3}$.

The physical mechanisms underlying these results are related to how the thermocline depth H responds to changes of $\Delta\rho$. In the constant-diffusivity case $H \sim \Delta\rho^{-1/3}$, which hampers the circulation when $\Delta\rho$ is increased, but not to such a degree that the response of the circulation is reversed. In the stability-dependent case $H \sim \Delta\rho^{-2/3}$, i.e. a more pronounced dependence than in the constant-diffusivity case. Somewhat counter-intuitively, this results in a curtailed circulation.

It is now of interest to examine how these results correspond to those from the numerical model describing a zonally averaged Boussinesq fluid in hydrostatic balance. The model domain is a single-hemispheric basin with solid vertical walls at equator and pole and an impermeable bottom at constant depth (i.e. neither topography nor continents). No transports are allowed through these boundaries, and at the surface the temperature is restored towards a prescribed temperature distribution, viz. heating at low latitudes and cooling at the pole. Furthermore the surface salinity is dynamically controlled by a prescribed vertical salinity flux arising from net evaporation and precipitation at low and high latitudes, respectively.

The vertical diffusivity is parameterized in two ways: As constant and as stability-dependent with $\kappa \sim \Delta\rho^{-1}$. The model behavior for each of these cases is compared.

Two types of model experiments are presented in paper I: Simulations with only thermal forcing, and with thermal as well as freshwater forcing (the latter case denoted mixed boundary conditions). For the "thermal" simulations no freshwater forcing was applied, implying that the density only is a function of temperature. The simulations are initiated from a reference state, whereafter the equator-to-pole temperature difference ΔT

is repeatedly incremented, the model runs each time being permitted to attain a new steady state.

The results from these simulations are presented in Fig. 5 of paper I, which shows the strength of the overturning circulation versus ΔT. The main conclusion is that the two parameterizations give rise to fundamentally different results: For constant diffusivity the overturning is enhanced with increasing ΔT, whereas in the stability-dependent case the results are reversed, i.e. the circulation weakens with increasing temperature forcing. These results corroborate those from the scale analysis and also agree with the outcome of three-dimensional modeling (Nilsson et al., 2003).

Analogous simulations also including freshwater forcing have additionally been undertaken. ΔT was held fixed throughout these experiments, while the freshwater forcing R was slightly increased before each consecutive numerical integration. These mixed-boundary results proved to be somewhat complex, since now the surface-density distribution is dynamically determined, whereas in the thermally forced simulations it was prescribed.

The results were found to be more-or-less in agreement with those from the thermally forced simulations. Increased freshwater forcing implies a weakened equator-to-pole density difference, corresponding to a smaller temperature difference in the thermally forced simulations. Hence, for an increased freshwater forcing the circulation weakens in the constant-diffusivity case, but is enhanced when the diffusivity is taken to be stability-dependent.

Paper I also includes a discussion of the salinity-dominated reversed circulation as well as an analysis of the feedback mechanisms between the circulation and the salinity field which underlie the time-dependent results forming a part of the investigation.

The main conclusion to be drawn is that constant and stability-dependent diffusivities in a single-hemispheric THC model give rise to fundamentally different results, which, however, conform to predictions from scale analysis. A logical next step, undertaken in paper II, is to generalize these results to a two-hemispheric model permitting asymmetric circulations.

2.2 The asymmetric mode

In paper II the analysis from paper I is extended to asymmetric flows using the same numerical THC model, but with the modeling domain encompassing both hemispheres.

Also here the cases with solely thermal forcing and with mixed forcing are studied separately, since the dynamics characterizing the thermally

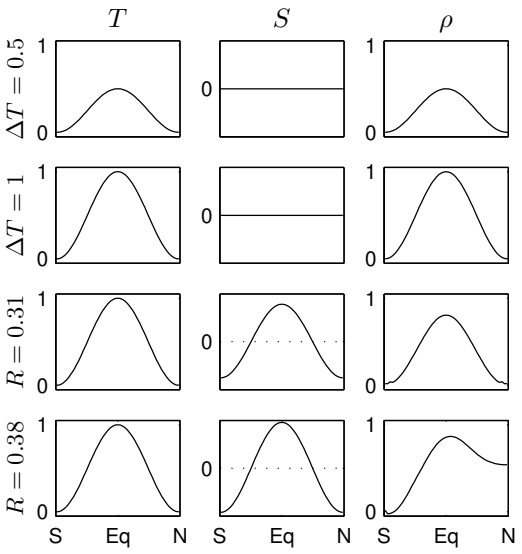

FIGURE 5: Surface distributions from the model. The left-hand, middle, and right-hand column shows the thermal forcing, the freshwater forcing, and the resulting steady-state surface-density distribution, respectively. The two upper rows show symmetric cases with different thermal forcing ($\Delta T = 0.5$ and $\Delta T = 1$, respectively). The two lower rows show cases with different strengths of the freshwater forcing (symmetric and asymmetric, respectively). The x-axes shows the latitude and the y-axes the magnitude of the parameter in question. All units non-dimensionalized.

forced system are more straightforward to interpret. In this latter case the density is only a function of temperature, since haline effects are absent. It has, however, been shown that it is the surface density distribution in itself which determines the properties of the interior-basin circulation. This makes it possible to reproduce a circulation which is dynamically determined from mixed boundary conditions by solely using a thermal boundary condition. The way in which this is accomplished is by selecting a thermal boundary condition with a distribution identical to the dynamically determined density distribution for mixed boundary conditions.

The freshwater impact on the surface-density distribution is illustrated in Fig. 5. From the bottom row of diagrams illustrating an asymmetric state, it is recognized that the freshwater forcing acts to reduce the density in one hemisphere, resulting in an asymmetric surface-density distribution.

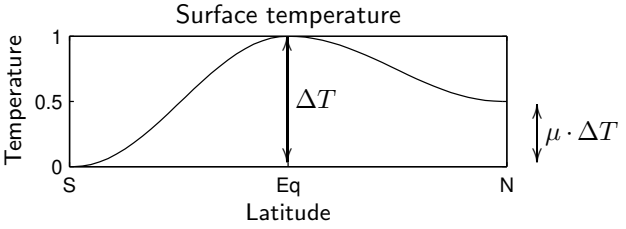

FIGURE 6: The distribution of the thermal forcing at $\mu = 0.5$. Units are non-dimensionalized.

The degree of asymmetry of the overturning circulation is controlled by the asymmetry of the surface-density distribution. Thus an attempt is made to analyze the asymmetric-state dynamics by first examining how the degree of asymmetry of the thermal forcing (i.e. no freshwater forcing) affects the system. The distribution of this thermal forcing is prescribed such that maximum heating takes place at the equator, cooling occurs at high latitudes, and there is a pole-to-pole temperature difference giving rise to the asymmetry. The degree of asymmetry is denoted μ, this being defined as the ratio between the pole-to-pole temperature difference and the equator-to-pole temperature difference ΔT, cf. Fig. 6.

Two types of simulations have been undertaken: Those where the degree of asymmetry is taken to be fixed ($\mu = 0.5$) and the magnitude of the forcing is varied, and those where $\Delta T = 1$ and μ is varied. As for the simulations reported in paper I, the numerical experiments were initiated from a reference state and the parameter (ΔT and μ, respectively) is slightly increased before each new simulation, which in turn is integrated until a steady state has been obtained.

For a fixed degree of asymmetry ($\mu = 0.5$) and a varying equator-to-pole temperature difference, the circulation is highly asymmetric and constituted by two circulation cells: a dominating forward-circulation cell (attaining its maximum in the northern hemisphere) extending well into the southern hemisphere, and a subordinate reversed-circulation cell confined to the surface layers in the southern high latitudes (cf. the upper panels in Fig. 7).

The first conclusion from the fixed-μ simulations is that only the vertical structure of the circulation is affected by variations of ΔT, the horizontal structure being more-or-less independent. This result is presented in Fig. 4 of paper II, from which it is seen that the vertical temperature profiles in

the constant-diffusivity case collapse when first normalized with ΔT and hereafter stretched with the theoretical thermocline depth scale derived in paper I.

It has also been concluded that the overturning response for a varying equator-to-pole temperature difference is consistent with the corresponding results from paper I, viz. for increasing ΔT the overturning is enhanced for constant diffusivity and weakened in the stability-dependent case (cf. Fig. 5 in paper II). Hence, the symmetric-flow scaling theory in paper I has proved to be applicable for asymmetric circulation states when the degree of skewness is retained constant.

The dynamical picture becomes more complex to interpret as the degree of asymmetry is varied. It is recognized that the symmetric-state scale analysis does not apply in this case. This analysis requires that the horizontal structure be preserved when the equator-to-pole surface density difference is varied, which was not the case when the degree of asymmetry was changed. Instead there is a spatial reorganization of the circulation, where the dominant cell grows spatially at the expense of the shrinking subordinate cell. This is seen from Fig. 6 in paper II, showing that the net poleward meridional heat transport remains more-or-less constant when μ is varied. It is also recognized that in this case there is no significant difference between the results from the constant and stability-dependent diffusivity parameterizations. A discussion of the physical mechanisms underlying this spatial reorganization is also included in paper II.

When mixed boundary conditions are applied, the effects of salinity make the dynamics more complicated. Simulations have also been performed in this case. These were initiated from the reference state, each numerical experiment being undertaken after having slightly increased the freshwater forcing R.

Below a certain threshold value of R the circulation is symmetric, the salinity acting to reduce the magnitude of the thermally imposed surface density, cf. Figs. 9 and 11 of paper II. Here the salinity and temperature fields are strongly correlated (cf. Fig. 7), as previously discussed in paper I. However, when the freshwater forcing exceeds a critical value, the symmetric mode becomes unstable and is transformed to a fundamentally different asymmetric steady state, cf. Fig. 10 of paper II where the salinity field is highly asymmetric and not correlated with the temperature (cf. Fig. 7).

As the freshwater forcing becomes larger the degree of asymmetry increases with R, whereas ΔT remains more-or-less constant (cf. Fig. 11 in paper II). This is in qualitative agreement with the results from the varying-μ simulations with only thermal forcing.

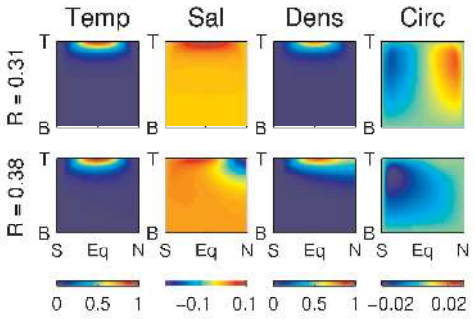

FIGURE 7: The temperature, salinity, density and streamfunction fields for a symmetric state (the upper panels) and for an asymmetric state (the lower panels). The x-axes shows the latitude and the y-axes the depth. All units are non-dimensionalized.

The overturning response as R increases is similar for both diffusivity parameterizations, cf. Fig. 12 in paper II. It is, however, recognized that for stability-dependent diffusivity the degree of asymmetry is more sensitive to changes of R than when the diffusivity is prescribed as constant.

The results from simulations with mixed boundary conditions where the freshwater forcing is kept fixed ($R = 0.5$) and ΔT is varied are also presented in paper II. In this case it was concluded that the the dominant-cell response differs for the two parameterizations. The overturning of the dominating cell weakens for stability-dependent diffusivity, whereas it is enhanced for constant diffusivity.

The overall conclusions from paper II are that the horizontal structure of the circulation varies with the degree of asymmetry, whereas the strength of the overturning is determined by the equator-to-pole density difference. When the freshwater forcing is varied and the thermal forcing is retained constant, it is mainly the degree of asymmetry which changes.

3 Altimetric studies

The discussion of papers I and II above has primarily focused on larger-scale aspects of the THC. There are, however, also important more-or-less local phenomena which affect this circulation. Thus processes in the Nordic Seas are of preeminent importance for the smooth operation of the present-day THC, since it is in this region that the winter-time convection which

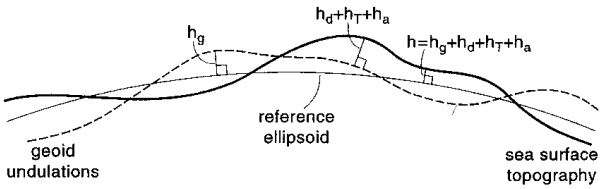

FIGURE 8: Schematic diagram showing the various components of the satellite-measured sea-surface height h.

transforms surface water of Atlantic origin to cold deep water takes place. The Greenland, Iceland and Norwegian Seas are, however, a somewhat inhospitable region for undertaking conventional oceanographic surveys, and thus satellite altimetry has proved to be a highly useful tool for examining the circulation characteristics of this area.

Investigations of the sea-surface elevation have played an important role for physical oceanography ever since the world-wide network of tidal gauges, on the basis of international agreements, begun to function as a unified observational system in the early 1880's. (This global network, incidentally, received its scientific baptism in the wake of the Krakatoa tsunami in 1883.) Due to remarkable technical developments in the field of microwave sensing, satellite altimetry has begun to play an increasingly important role during the last twenty years for studies of this type.

The measuring principles underlying this observational technique are schematically demonstrated in Fig. 8. This diagram shows, relative to a reference ellipsoid, the various contributions to the sea-surface height h measured in the course of an altimetric satellite mission such as e.g. TOPEX/-Poseidon. The components of h include the geoid undulations h_g, tidal variations h_T, atmospheric pressure loading h_a, and the dynamic sea-surface height h_d associated with geostropically-balanced barotropic currents. Since we have no *a priori* knowledge of the undulations of the geoid, it is recognized that all sea-level information originating from satellite data will be in the form of anomalies relative the long-term observational averages. In papers III and IV as well as in the subsequent overview, this quantity will be denoted SLA.

In the present thesis Nordic-Seas anomaly results have been analyzed in two ways. In paper III focus is thus on the 1992–2004 average seasonal (winter-to-summer) SLA-differences, whereas paper IV deals with the temporal evolution of the altimetric data series.

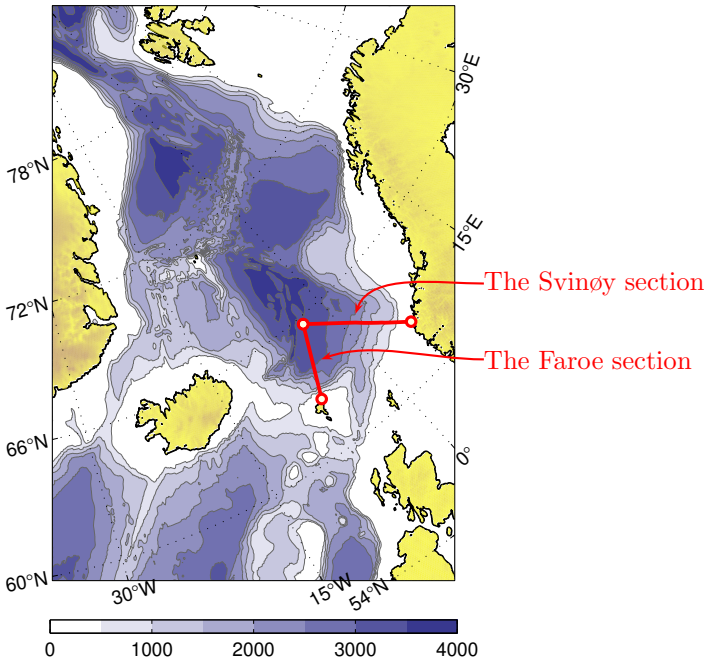

FIGURE 9: Map over the Nordic-Seas region showing the bathymetry. The Svinøy and Faroe sections are labeled in the figure.

3.1 Seasonal anomalies

In Paper III the seasonal variability of the circulation in the Nordic-Seas region is investigated, primarily on the basis of results from the classical Svinøy section and a section extending 500 km north-northeastwards from the Faroe Islands (cf. Fig. 9). The circulation is separated into barotropic and baroclinic parts, where the former is related to the primarily wind-driven horizontal redistribution of mass and the latter to variations of the hydrography. SLA-differences based on satellite-altimetric measurements (cf. Fig. 10) are used to estimate the seasonal variations of the barotropic circulation, and climatological hydrographic data are utilized for estimating the seasonal variations of the baroclinic circulation. The hydrographic data have insufficient temporal resolution to permit an analysis over monthly time-scales, and thus seasonally averaged anomaly data are used, with emphasis on the winter-to-summer differences.

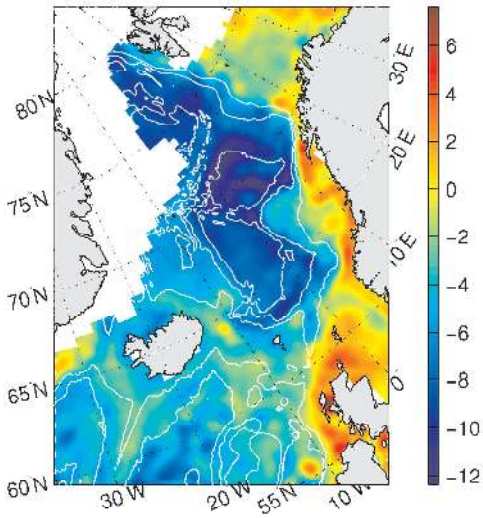

FIGURE 10: The winter-to-summer difference of the sea-surface height in cm. The white lines represent equidistant isobaths with 1000 m spacing.

Paper III also presents a method to estimate the depth-integrated baroclinic flow associated with the hydrography. From the results, shown in Fig. 2 of paper III, it can be seen that the magnitude of the winter-to-summer difference of the depth-integrated baroclinic flow is on the order of 5 Sv. It is also recognized that the baroclinic flow anomalies generally are associated with transports across the isobaths.

To obtain the depth-independent barotropic height anomaly η_0, the steric-height anomaly is subtracted from the SLA field shown in Fig. 3 of paper III. It becomes evident that η_0 is strongly correlated with the bathymetry, which suggests that the seasonal changes of the barotropic flow essentially take place along the isobaths (as indeed predicted by basic dynamic theory). From the figure it is also apparent that the sea level in the central Nordic Sea basin is depressed during winter, indicating that a large-scale re-circulation takes place in the interior of the Nordic Seas. Hence it is of considerable interest to examine whether this re-circulation can be separated from the Atlantic inflow of warm saline water over the Iceland-Scotland Ridge into the Nordic Seas. This investigation is undertaken using results from the Svinøy and Faroe sections (cf. Fig. 9).

The winter-to-summer difference of the total surface-layer velocity can be calculated using the SLA data and assuming that the flow is geostrophically balanced. Figs. 5 and 8 of paper III, pertaining to the Svinøy and Faroe transects, respectively, show the calculated normal-velocity anomalies, which mainly are directed eastwards. An exception is, however, encountered at bottom depths around 2500 m, where the flows are have the opposite direction. For the Svinøy section this feature can be seen in drifter data by Jakobsen et al. (2003). For the Faroe section it is argued that this is due to the presence of the Iceland-Faroe front, which on account of stronger forcing is more pronounced during winter than in summer. These winter-to-summer variations of the permanent Iceland-Faroe front are discussed by analyzing the salinity field for the Faroe section (cf. Fig. 7 of paper III).

The winter-to-summer differences of the depth-integrated barotropic and baroclinic transports (the latter estimated using the analytical methods derived in the appendix of paper III) are presented in Figs. 6 and 9 of paper III. From these results it is recognized that the baroclinic transport is much smaller than the barotropic one. However, the main conclusion to be drawn from these figures is that the accumulated barotropic transport anomaly is on the order of 10 Sv through both the Svinøy and Faroe transects. This is considerably larger than the classical estimate (Worthington, 1970) of the Iceland-to-Scotland surface-water inflow (7 Sv). This discrepancy is, most likely, associated with the central Norwegian-Sea re-circulation, which

has been examined using a salinity representation of the winter-to-summer barotropic transport difference, cf. Fig. 12 of paper III. This diagram shows that the transport anomalies pertaining to low-saline waters (characterized by salinities below 35) are associated with the re-circulation in the interior of the Nordic Seas, whereas the "high-saline" transport anomalies are linked to the Atlantic inflow. The magnitude of the re-circulation anomaly is 8 Sv, viz. in broad agreement with numerical-model results (Isachsen et al., 2003). The high-saline barotropic transport across the Svinøy transect was found to be around 3 Sv larger during winter than in summer, i.e. the same order of magnitude as that of estimates based on measurements (Orvik et al., 2001).

3.2 Low-frequency variability

The main focus of paper IV is on the variability of the barotropic flow and the wind stress in the Norwegian Sea over time-scales ranging from months to years. An analytical theory, inspired by some ideas due to Walin (1972), is presented for how the low-frequency wind forcing primarily generates a barotropic flow along contours of constant depth. After introducing some auxiliary assumptions (e.g. that the Coriolis parameter is constant and that the buoyancy field is horizontally uniform), is possible to calculate an averaged along-isobath velocity using sea-level information and bathymetric data. This isobath-averaged velocity can be calculated from the wind stress using a linear differential equation. Similar studies have been undertaken by Isachsen et al. (2003); Nøst and Isachsen (2003) as well as by Nilsson et al. (2005).

In paper IV the along-isobath velocity is estimated for the closed 2500-m isobath girdling the Norwegian and Lofoten basins. This is done in two ways: SLA data from satellite measurements yield $\overline{\mathcal{V}}_{\mathrm{SLA}}$, and wind data from a re-analysis model yield $\overline{\mathcal{V}}_{\mathrm{w}}$.

Before $\overline{\mathcal{V}}_{\mathrm{SLA}}$ and $\overline{\mathcal{V}}_{\mathrm{w}}$ were compared, it was concluded that the isobath-averaging method is capable of isolating a large-scale coherent signal from the SLA data. An auto-correlation analysis has also been undertaken to determine the damping parameter in the linear differential equation used for calculating $\overline{\mathcal{V}}_{\mathrm{w}}$.

The low-frequency variability of $\overline{\mathcal{V}}_{\mathrm{SLA}}$ and $\overline{\mathcal{V}}_{\mathrm{w}}$ proved to be essentially coherent, as seen from Fig. 5 of paper IV. However, the amplitudes differ by a factor of two, which can be due to e.g. steric and baroclinic effects, the choice of the damping parameter, and the resolution of the SLA and wind fields. Nevertheless, it has been concluded that the Norwegian-Sea

re-circulation gyre is predominantly forced by the local wind stress.

One of the main aims of paper IV is to compare and to, if possible, distinguish between the flow along closed isobaths and that along open isobaths extending over the Iceland-Scotland Ridge into the North Atlantic proper. The flow along an open isobath transgressing the classical Svinøy section (cf. Fig. 9) is thus also examined. Here the Norwegian Atlantic Slope Current (NwASC) is located over the depth interval 300–800 m (Skagseth, 2004), i.e. well separated from the re-circulation gyre. The working hypothesis is that the NwASC, originating in the Atlantic proper at the Irish-Scottish shelf, should be subjected to wind forcing taking place at a considerable distance from the Norwegian Sea.

The velocity of the NwASC at Svinøy was estimated using altimetry data, with an approximation of the averaged SLA difference along the 750-m isobath at Svinøy constituting a proxy for the NwASC.

The correspondence between this NwASC proxy and the re-circulation in the central Norwegian Sea is presented in Fig. 6 of paper IV. It is recognized that for certain periods the two flows co-vary, but there are also instances when the flows appear to be decoupled.

To investigate the extent to which the NwASC is coherent with the large-scale wind patterns, the NwASC proxy was compared to the NAO index as well as to the integrated wind stress along the 500-m isobath. The result of these comparisons is that there is a fair degree of agreement between the NwASC proxy and these wind indices.

4 Overview and outlook

The present study is partly based on the use of zonally-averaged modelling techniques, partly on the application of satellite-altimetric observations. It is hoped that the considerations presented in this thesis summary has helped to convince the reader that a viable path for future climate studies may lie in a fruitful combination of modelling and empirical studies. As regards the latter type of investigations, the present thesis has had its focus on satellite altimetry. It is, however, important to underline that standard hydrography of the type most recently obtained on a world-wide scale in connection with the international WOCE programme also has an important role to play. An interesting example of a climatologically relevant long-duration hydrographic time-series is provided by the classical Faroe-Shetland section, also known as the Nolsøy-Flugga transect with reference to its endpoints. Regular surveys of this important choke-point for the inflow of Atlantic surface water to the Norwegian Sea began towards the

end of the 19th century (Turrell et al., 1999). Since this section is still regularly surveyed, the results constitute one of the longest oceanographical series available for climatological research.

When attention is directed toward the field of numerical modelling, it is relevant to underline that it is highly likely that within the foreseeable future nonhydrostatic global models will be implemented for the entire ocean-atmosphere system (Held and Suarez, 1994). These models will presumably be capable of doing better justice to convection processes (of crucial importance for the global THC) than those operational today. Hence one might speculate that many present-day modelling results will stand a risk of losing their immediate relevance. Not least in view of this in view of this dystopic perspective it must be emphasized that the highly simplified 2-dimensional ocean-circulation models applied in the present thesis may be somewhat more resistant to the winds of change. Another appealing feature of these models is that they only are expected to provide lowest-order results for identifying critical processes, which, it is hoped, will remain invariant.

To conclude, it is thus suggested that it is not *a priori* given that highly complex three-dimensional modelling of the atmosphere-ocean system represents the only way ahead for climatological studies. The presents thesis has attempted to demonstrate that simplified models as well as empirical observations also may have an important role to play.

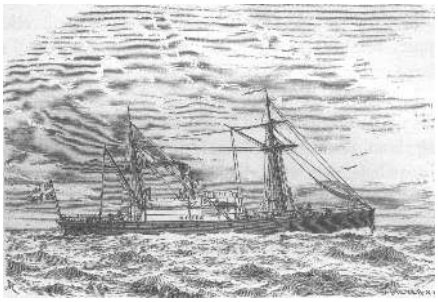

Bibliography

Bryan, F., 1986. High-latitude salinity effects and interhemispheric thermohaline circulations. Nature 323 (6086), 301–304.

Held, I., Suarez, M. J., 1994. A proposal for the intercomparison of the dynamical cores of atmospheric general circulation models. Bulletin of the American Meteorological Society 75 (10), 1825–1830, doi:10.1175/1520-0477(1994)075<1825:APFTIO>2.0.CO;2.

Helland-Hansen, B., Nansen, F., 1909. The Norwegian Sea, its physical oceanography. based on the Norwegian researches 1900–1904. Report on Norwegian fishery and marine investigations 2 (2), 1–359.

Huang, R. X., 1999. Mixing and energetics of the oceanic thermohaline circulation. Journal of Physical Oceanography 29 (4), 727–746, doi:10.1175/1520-0485(1999)029<0727:MAEOTO>2.0.CO;2.

Isachsen, P. E., LaCasce, J. H., Mauritzen, C., Häkkinen, S., 2003. Wind-driven variability of the large-scale recirculating flow in the Nordic Seas and Arctic Ocean. Journal of Physical Oceanography 33 (12), 2534–2550, doi:10.1175/1520-0485(2003)033<2534:WVOTLR>2.0.CO;2.

Jakobsen, P. K., Ribergaard, M. H., Quadfasel, D., Schmith, T., Hughes, C. W., 2003. Near-surface circulation in the northern North Atlantic as inferred from Lagrangian drifters: Variability from the mesoscale to interannual. Journal of Geophysical Research 108 (C8), 3251, doi:10.1029/2002JC001554.

Knudsen, M., 1899. Hydrografi. Den Danske Ingolf-expedition 1 (2).

Marotzke, J., Welander, P., Willebrand, J., 1988. Instability and multiple steady states in a meridional-plane model of the thermohaline circulation. Tellus, Series A 40 (2), 162–172.

Mohn, H., 1885. Die Strömungen des Europäischen Nordmeeres. Petermanns Geographische Mitteilungen 7.

Mohn, H., 1887. Nordhavets dyber, temp. og ströminger. Den Norske Nordhavs-Expedition, 1876–1878 2 (2).

Nilsson, J., Broström, G., Walin, G., 2003. The thermohaline circulation and vertical mixing: Does weaker density stratification give stronger overturning? Journal of Physical Oceanography 33 (12), 2781–2795, doi:10.1175/1520-0485(2003)033<2781:TTCAVM>2.0.CO;2.

Nilsson, J., Broström, G., Walin, G., 2005. Steady f-plane circulation arising from a prescribed buoyancy distribution in basins with sloping boundaries; or the role of bottom friction for creating a thermohaline circulation, submitted to Journal of Marine Research.

Nilsson, J., Walin, G., 2001. Freshwater forcing as a booster of thermohaline circulation. Tellus, Series A 53 (5), 629–641, doi:10.1034/j.1600-0870.2001.00263.x.

Nordenskiöld, A. E., 1885. Den andra Dicksonska expeditionen till Grönland. Beijer förlag, Stockholm.

Nøst, O., Isachsen, P., 2003. The large-scale time-mean ocean circulation in the Nordic Seas and Arctic Ocean estimated from simplified dynamics. Journal of Marine Research 61 (2), 175–210, doi:10.1357/002224003322005069.

Orvik, K. A., Skagseth, Ø., Mork, M., 2001. Atlantic inflow to the Nordic Seas: current structure and volume fluxes from moored current meters, VM-ADCP and SeaSoar-CTD observations, 1995-1999. Deep Sea Research Part I 48 (4), 937–957, doi:10.1016/S0967-0637(00)00038-8.

Rahmstorf, S., 2000. The thermohaline ocean circulation: a system with dangerous thresholds? Climatic Change 46 (3), 247–256, doi:10.1023/A:1005648404783.

Skagseth, Ø., 2004. Monthly to annual variability of the Norwegian Atlantic Slope Current: Connection between the northern North Atlantic and the Norwegian Sea. Deep-Sea Research Part I 51 (3), 349–366, doi:10.1016/j.dsr.2003.10.014.

Spieß, F., 1928. Die Meteor-Fahrt — Forschungen und Erlebnisse der Deutschen Atlantischen Expedition 1925–1927. Reimer, Berlin.

Thomson, S. C. W., 1878. The Voyage of the Challenger. The Atlantic. Harper & Brothers, New York.

Turrell, W. R., Slesser, G., Adams, R. D., Payne, R., Gillibrand, P. A., January 1999. Decadal variability in the composition of faroe shetland channel bottom water. Deep Sea Research Part I: Oceanographic Research Papers 46 (1), 1–25, doi:10.1016/S0967-0637(98)00067-3.

Walin, G., 1972. On the hydrographic response to transient meteorological disturbances. Tellus 24, 169–186.

Welander, P., 1986. Thermohaline effects in the ocean circulation and related simple models. In: Willebrand, J., Anderson, D. L. T. (Eds.), Large-Scale Transport Processes in Oceans and Atmosphere. D. Reidel publishing company, pp. 163–200.

Wild, J. J., 1877. Thalassa: an essay on the depth, temperature and currents of the ocean. Marcus Ward & Co., London.

Worthington, L. V., 1970. The Norwegian Sea as a Mediterranean basin. Deep-Sea Research 17, 77–84.

Wright, D. G., Stocker, T. F., 1991. A zonally averaged ocean model for the thermohaline circulation. Part I: Model development and flow dynamics. Journal of Physical Oceanography 21 (12), 1713–1724, doi:10.1175/1520-0485(1991)021<1713:AZAOMF>2.0.CO;2.

Paper I

The role of diapycnal mixing for the equilibrium response of thermohaline circulation

Rezwan Mohammad and Johan Nilsson

Ocean Dynamics, 2004, **54**(1), 54–65

Abstract

Using a zonally averaged, one-hemispheric numerical model of the thermohaline circulation, the dependence of the overturning strength on the surface equator-to-pole density difference is investigated. It is found that the qualitative behavior of the thermohaline circulation depends crucially on the nature of the small-scale vertical mixing in the interior of the ocean. Two different representations of this process are considered: constant vertical diffusivity and the case where the rate of mixing energy supply is taken to be a fixed quantity, implying that the vertical diffusivity decreases with increasing stability of the water column. When the stability-dependent diffusivity parameterization is applied, a weaker density difference is associated with a stronger circulation, contrary to the results for a fixed diffusivity. A counterintuitive consequence of the stability-dependent mixing is that the poleward atmospheric freshwater flux, which acts to reduce the thermally imposed density contrast, strengthens the thermally dominated circulation and its attendant poleward heat transport. However, for a critical value of the freshwater forcing, the thermally dominated branch of steady states becomes unstable, and is succeeded by strongly time-dependent states that oscillate between phases of forward and partly reversed circulation. When a constant vertical diffusivity is employed, on the other hand, the thermally dominated circulation is replaced by a steady salinity-dominated state with reversed flow. Thus in this model, the features of the vertical mixing are essential for the steady-state response to freshwater forcing as well as for the character of flow that is attained when the thermally dominated circulation becomes unstable.

1 Introduction

The view that freshwater forcing, associated with the meridional atmospheric transport of water vapor, curtails and destabilizes the thermohaline circulation is deeply rooted inside as well as outside the scientific community. The argument behind this notion is straightforward and based on two considerations; *pro primo*, the fact that the freshwater forcing creates a salinity field that reduces the thermally imposed equator to pole-density difference and *pro secundo*, the assumption that the thermohaline circulation is favored by a strong equator-to-pole density difference. Furthermore, this view seems to be supported by the results from a large body of numerical ocean circulation studies (e.g. Marotzke et al., 1988; Weaver et al., 1993; Park and Bryan, 2000).

Contrary to established wisdom, however, a number of recent investigations (Lyle, 1997; Huang, 1999; Nilsson and Walin, 2001) have concluded that it is fully possible that the thermohaline circulation may intensify, rather than slow down, in response to a weaker equator-to-pole density difference. The relation between vertical mixing and the stratification is at the heart of this remarkable result, and the underlying physics are straightforward: Consider thermohaline circulation in a one-hemisphere basin, where a thermocline separates the warm poleward-flowing water in the upper ocean from the cold water beneath. Suppose now that the equator-to-pole density difference suddenly is reduced and that the ocean adjusts to the new forcing. Regardless of the details of vertical mixing, we will observe two changes after the adjustment; the speed of the poleward-flowing warm water has decreased, and the depth of the thermocline has increased. The latter change serves to augment the net poleward flow, whereas the former acts to hamper it. It is here the properties of vertical mixing, which controls the response of thermocline depth, become crucial: If the turbulent vertical diffusivity is assumed to be fixed — the standard assumption in ocean modeling — the net poleward flow will decline. On the other hand, if the diffusivity increases as the stratification becomes weaker — a physically reasonable behavior — the net poleward transport may amplify. Based on these considerations, Nilsson and Walin (2001) advanced the idea that the reduction in the equator-to-pole density difference caused by the salinity field may serve to strengthen the thermohaline circulation, rather than to weaken it.

In fact, the numerical one-hemisphere simulations due to Huang (1999) and Nilsson et al. (2003) have demonstrated that if the vertical mixing is suppressed by strong stratification, the strength of thermohaline circulation

decreases with increasing equator-to-pole density difference. Both these studies dealt with purely thermal flows, forced by a prescribed distribution of sea-surface temperature. However, when the circulation is forced by a prescribed sea surface temperature as well as by a freshwater flux (i.e. mixed boundary conditions), the surface density distribution becomes a function of the flow. As pointed out by Stommel (1961), this implies that there may exist multiple equilibria. In addition to the thermally dominated circulation of the forward type — the mode studied by Huang (1999) and Nilsson et al. (2003) — there generally exist equilibria with reversed flow where the salinity field dominates the density distribution (e.g. Welander, 1986; Thual and McWilliams, 1992; Weaver et al., 1993). Further, there may exist an upper bound on the freshwater forcing, beyond which an equilibrium with forward circulation cannot be attained.

A main purpose of the present study is to explore how the representation of vertical mixing affects the overturning dynamics when the circulation is forced by mixed boundary conditions. To address this issue, a two-dimensional numerical model has been employed and simulations have been carried out for a broad range of surface forcing. The model is a zonally-averaged representation of thermohaline circulation in a single-hemisphere basin. As a preliminary to the numerical investigation, a scale analysis of thermohaline flows is presented. Basically, this analysis follows that of Nilsson and Walin (2001). However, a theoretical investigation of the dynamics in the limit where the thermocline depth approaches the ocean bottom represents a novel contribution; an issue followed up in the analyses of the numerical simulations. It is emphasized that this is an idealized study addressing a problem of basic importance for the dynamics of the thermohaline circulation. As with all idealized models, there are caveats associated with this study. Thus in the concluding section, the relevance of our findings for the real ocean are subjected to a critical discussion.

2 Scaling analysis

Our first step is to apply a simple scale analysis to the thermohaline circulation in order to judge how its strength is related to the equator-to-pole density difference and the specifics of the vertical mixing. As background it is instructive to consider a meridional cross-section of potential density distribution in the Atlantic basin (cf. Fig. 1). These observations suggest that, as a first approximation, the ocean may be regarded as stratified where a thin upper layer of light water is separated from a deep, nearly homogeneous layer of dense water by a pycnocline. Furthermore the obser-

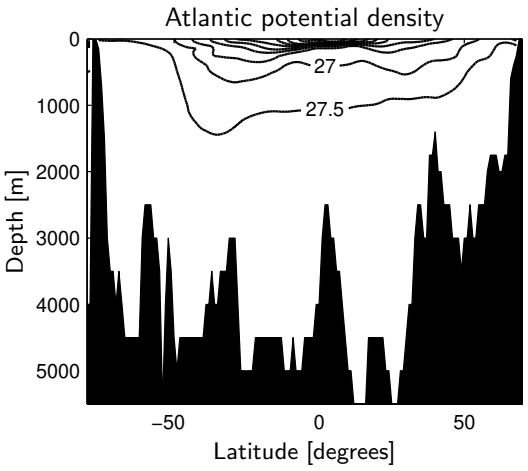

FIGURE 1: Meridional potential density cross-section in the Atlantic basin along 30° west latitude. Density in units of kg/m^3−1000. Contour interval is 0.5 kg/m^3. Data is from Levitus (1982).

vations indicate that the equator-to-pole density difference at the surface to lowest order equals the vertical density difference at low latitudes.

In what follows a one-hemispheric basin is considered[1] (cf. Fig. 2). The equator-to-pole density difference at the surface ($\Delta\rho$) is prescribed, whereas the depth of the pycnocline (H) and the circulation (ψ) are to be predicted. The depth of the basin is denoted D, the poleward volume transport is ψ_{I} and the diapycnal volume transport upwards is ψ_{II}. Here the depth of the pycnocline is assumed to be small, $H/D \ll 1$. (The case when the pycnocline depth is large, $H \sim D$, is dealt with separately.)

In the scale analysis the circulation is assumed to be in hydrostatic and geostrophic balance, which implies (Welander, 1986) that the thermal wind relation is valid:

$$\frac{\partial v}{\partial z} = -\frac{g}{f\rho_0} \cdot \frac{\partial \rho}{\partial x}.$$

Here x and z are the independent coordinates in the zonal and vertical directions, respectively, v is the meridional velocity, g the gravity, f the Coriolis parameter, ρ the density, and ρ_0 a reference density. Furthermore,

[1]Here, the one-hemisphere geometry may be viewed as a conceptual representation of a general thermohaline flow where the low-latitude upwelling is routed towards the sinking regions in near-surface currents; see also the discussion in the concluding section.

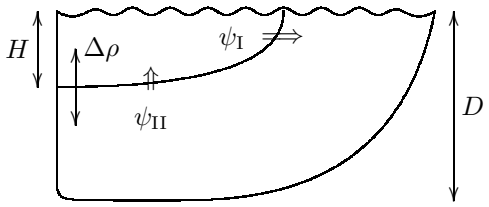

FIGURE 2: Sketch of a simple one-hemisphere two-layer system.

vertical advection is assumed to balance vertical diffusion (Munk, 1966):

$$w\frac{\partial\rho}{\partial z} = \frac{\partial}{\partial z}\left(\kappa\frac{\partial\rho}{\partial z}\right),$$

where w is the vertical velocity and κ is the diffusivity coefficient representing the vertical small-scale mixing.

To estimate the overturning circulation, the poleward and diapycnal flows have to be determined. The former quantity is scaled using the thermal wind relation, where the zonal density gradient is assumed to be proportional to that in the meridional direction, a conjecture which is supported by results from three-dimensional modeling (e.g. Wright and Stocker, 1991; Wright et al., 1998; Park and Bryan, 2000). This proportionality implies that the poleward volume transport scales as

$$\psi_{\mathrm{I}} \sim \frac{g}{f\rho_0}\cdot\Delta\rho\cdot H^2. \tag{1}$$

Assuming that the advective-diffusive balance controls the stratification, the diapycnal flow scales as

$$\psi_{\mathrm{II}} \sim A\cdot\frac{\kappa}{H}, \tag{2}$$

where A is the area of the low-latitude stratified part of the basin where the upwelling occurs. Note that in a more general case, where the globally integrated thermohaline circulation is considered, A should be interpreted as the effective area of the low-latitude upwelling in all ocean basins.

In a steady state the poleward and diapycnal flows must be equal, yielding the following relation between the pycnocline depth and the density difference:

$$H \sim \left(\frac{f\rho_0 A}{g}\right)^{1/3}\cdot\kappa^{1/3}\cdot\Delta\rho^{-1/3}. \tag{3}$$

Substituting this result in eq. (1) or (2) the steady-state overturning is obtained:

$$\psi \sim \left(\frac{gA^2}{f\rho_0}\right)^{1/3} \cdot \kappa^{2/3} \cdot \Delta\rho^{1/3}, \tag{4}$$

which shows that the strength of the overturning is controlled by density as well as by vertical diffusivity.

2.1 Vertical mixing

The postulated physical basis of the vertical mixing, which controls the relation between diffusivity and density difference, plays an important role. A classical assumption concerning the vertical mixing is to keep the diffusivity fixed, viz. independent of the vertical stability. This parameterization, which is frequently used in ocean-circulation models, implies that the overturning scales as

$$\psi \sim \Delta\rho^{1/3}. \tag{5}$$

The strength of the overturning is enhanced as the density difference increases, consonant with the established view (Park and Bryan, 2000). Note, however, that the response of the overturning to changes in $\Delta\rho$ is weaker than linear: According to eq. (3), the pycnocline depth decreases with $\Delta\rho$ as $H \sim \Delta\rho^{-1/3}$, which, in view of eq. (1), acts to curtail the overturning. An increase of $\Delta\rho$ does not only yield stronger meridional velocities, but also a more shallow pycnocline which inhibits the strengthening of the poleward transport.

Although κ frequently is assumed to be fixed in ocean modeling, straightforward energy considerations suggest that κ in fact depends on the vertical density difference (which is roughly proportional to the equator-to-pole density difference $\Delta\rho$). In a stratified fluid, small-scale vertical mixing (quantified in terms of κ) creates potential energy (Munk and Wunsch, 1998) as

$$\mathcal{E} = \rho_0 \int \kappa N^2 \, \mathrm{d}z, \tag{6}$$

where $\mathcal{E}$ is the rate of increase in potential energy per unit area and N the buoyancy frequency, defined by

$$N^2 = -\frac{g}{\rho_0}\frac{\partial\rho}{\partial z}.$$

It is reasonable to assume that the rate of energy supply to small-scale mixing from e.g. winds and tides is constant, which implies that also $\mathcal{E}$, the

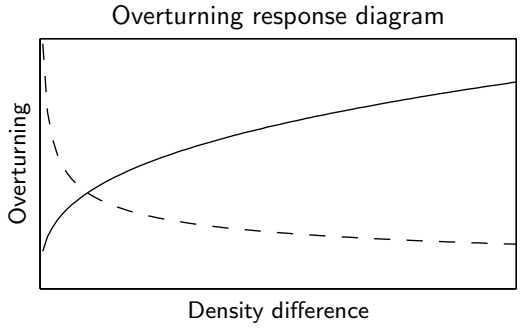

FIGURE 3: Qualitative response diagram showing overturning as a function of the density difference between equator and pole for constant (solid) and stratification-dependent (dashed) diffusivity, respectively, according to the scale analysis (eq. 5 and 8).

production rate of potential energy, should be constant. This argument, originally advanced by Kato and Phillips (1969), when applied to eq. (6) yields the following dependence of the vertical diffusivity coefficient on the density difference:

$$\kappa \sim \frac{\mathcal{E}}{g\Delta\rho}. \tag{7}$$

Thus, if the rate of energy supply available for small-scale vertical mixing is taken to be fixed, a stronger vertical density difference implies a smaller diffusivity. Using this result in eq. (4) yields that the overturning scales as

$$\psi \sim \Delta\rho^{-1/3}. \tag{8}$$

As seen from Fig. 3, the two representations of mixing give rise to strikingly different overturning characteristics. If the diffusivity is constant the overturning intensifies with an increasing equator-to-pole density difference, whereas it weakens if the diffusivity is dependent on the vertical stability.

The pycnocline depth decreases with density difference ($H \sim \Delta\rho^{-2/3}$, cf. eq. 3) more rapidly than in the previous case when the diffusivity was taken to be constant, having the somewhat counter-intuitive consequence that the circulation slows down.

2.2 Effects of finite basin depth

For fixed mixing energy, the overturning increases beyond bounds when $\Delta\rho$ approaches zero (cf. eq. 8). This raises the question whether the scale

analysis is valid in the regime when the density difference is small.

According to eq. (3) also the pycnocline depth becomes unbounded as $\Delta\rho$ approaches zero. As a result the pycnocline will eventually approach the bottom of the basin, $H \sim D$. When this occurs, the depth scale of the stratification is controlled by the geometry rather than by the advective-diffusive balance (eq. 2), which becomes redundant. Hence the circulation is only governed by the thermal wind relation:

$$\psi \sim \frac{gD^2}{f\rho_0} \cdot \Delta\rho. \tag{9}$$

According to this result the strength of the circulation responds in a linear fashion to changes in $\Delta\rho$. This result is independent of the representation of the diffusivity and is consequently valid for constant as well as stability-dependent diffusivity.

For fixed diffusivity, the response to changes of the density difference is weaker in the regime where $\Delta\rho$ is large ($H/D \ll 1$) than in the regime where it is small ($H \sim D$). Nevertheless, the derivative of the response has the same sign in both regimes. However, for fixed mixing energy the derivative changes sign between the regimes. The response is negative for large $\Delta\rho$, whereas it is positive for small $\Delta\rho$. Consequently the strength of the circulation should assume a maximum for the specific density difference that yields $H \sim D$, which can be determined using eq. (3):

$$\Delta\rho_m \sim \left(\frac{f\rho_0 A\mathcal{E}}{g^2}\right)^{1/2} \cdot D^{-3/2}.$$

Applying this result to eq. (9) the maximum strength of the circulation is:

$$\psi_m \sim \left(\frac{A\mathcal{E}}{f\rho_0}\right)^{1/2} \cdot D^{1/2}.$$

Thus, the maximum possible overturning strength increases with the basin depth as well as with the rate of increase in potential energy due to mixing (i.e. $A\mathcal{E}$). However, it may be noted that ψ_m is not very sensitive to changes in these parameters; for instance a doubling of D yields only an increase in ψ_m of about 40 %.

3 The model

These results spurred us to investigate whether the two representations of the diffusivity yield similar results in an idealized numerical thermohaline

circulation model. We use a zonally-averaged, two-dimensional, thermohaline circulation model similar to the ones previously employed in various climate studies (Marotzke et al., 1988; Wright and Stocker, 1991), although the model domain in the present study is taken to encompass solely one hemisphere.

3.1 Governing equations

Essentially, the derivation of the zonally averaged model equations follows Marotzke et al. (1988). The model describes a Boussinesq fluid in hydrostatic equilibrium, confined within a basin of constant depth (D) and zonal width (B) that has the meridional length L. The horizontal momentum equation is

$$\gamma v = -\frac{1}{\rho_0}\frac{\partial p}{\partial y}, \tag{10}$$

where v is the zonally averaged meridional velocity, γ is a closure parameter relating flow speed and pressure gradient, ρ_0 is the reference density, p is the zonally averaged pressure and y is the meridional coordinate. The basic closure hypothesis underlying eq. (10) is that the east-west and the north-south pressure gradients are proportional (see e.g. Wright et al., 1998, for an extensive discussion of flow representations in zonally averaged models). The hydrostatic balance is given by

$$\frac{\partial p}{\partial z} = -\rho g, \tag{11}$$

where ρ is the zonally averaged density and z is the vertical coordinate. Conservation of mass yields:

$$\frac{\partial v}{\partial y} + \frac{\partial w}{\partial z} = 0, \tag{12}$$

where w is the zonally averaged vertical velocity. The conservation of heat and salt is given by

$$\frac{\partial}{\partial t}\begin{pmatrix}T\\S\end{pmatrix} + v\frac{\partial}{\partial y}\begin{pmatrix}T\\S\end{pmatrix} + w\frac{\partial}{\partial z}\begin{pmatrix}T\\S\end{pmatrix} = \frac{\partial}{\partial z}\left(\kappa\frac{\partial}{\partial z}\begin{pmatrix}T\\S\end{pmatrix}\right), \tag{13}$$

where T and S is the zonally averaged temperature and salinity, respectively, and κ is the vertical diffusivity. For simplicity a linear equation of state is used:

$$\rho(S,T) = \rho_0\left(1 - \alpha T + \beta S\right), \tag{14}$$

where α and β are expansion coefficients for heat and salt, here taken to be constants. For this two-dimensional system it proves convenient to introduce a meridional streamfunction ψ:

$$Bv = -\frac{\partial \psi}{\partial z}, \qquad Bw = \frac{\partial \psi}{\partial y},$$

where ψ satisfies mass conservation (eq. 12) and B is the zonal width of the basin.

By eliminating the pressure in the horizontal momentum balance (eq. 10) and the hydrostatic balance (eq. 11), rewriting the velocity in terms of the streamfunction, and, using the equation of state (eq. 14), the following relation is obtained:

$$\frac{\partial^2 \psi}{\partial z^2} = -B \cdot \frac{g}{\gamma} \cdot \left(\beta \frac{\partial S}{\partial y} - \alpha \frac{\partial T}{\partial y} \right). \tag{15}$$

This equation is used to calculate the streamfunction from temperature and salinity.

It is relevant to note that this zonally averaged model can be scaled using the same procedure as outlined in section 2. If this is carried through, one finds that the pycnocline depth obeys

$$H \sim (\gamma \rho_0 L^2 / g)^{1/3} \cdot \kappa^{1/3} \cdot \Delta\rho^{-1/3},$$

and the overturning obeys

$$\psi \sim (g L^4 / \gamma \rho_0)^{1/3} \cdot (B/L) \cdot \kappa^{2/3} \cdot \Delta\rho^{1/3}.$$

The scale dependence of H and ψ on κ and $\Delta\rho$ derived in section 2 thus also applies for the zonally averaged model, which is a consequence of the horizontal momentum closure (10) employed here.

3.2 Boundary conditions

We are dealing with a basin of meridional extent L and depth D. No transport takes place through the solid boundaries, implying that $\psi = 0$ here. Neither heat nor salinity fluxes through the bottom are permitted, viz.

$$\frac{\partial T}{\partial z} = \frac{\partial S}{\partial z} = 0.$$

At the surface the temperature is prescribed:

$$T_{\text{top}}(y) = \frac{\Delta T}{2} \cdot \left(1 + \cos\left(y \cdot \frac{\pi}{L} \right) \right),$$

where the temperature has a maximum ΔT at the equator and equals zero at the pole. The salinity is dynamically controlled through a prescribed salinity flux F at the surface:

$$F(y) = -F_0 \cdot \cos\left(y \cdot \frac{\pi}{L}\right) = -\kappa \frac{\partial S}{\partial z},$$

where F_0 is the magnitude of the maximum salinity flux. The physical interpretation of this prescribed distribution is that maximal net evaporation and precipitation take place at the equator and pole, respectively.

3.3 Parameterization of the diffusivity

The two different representations of mixing described above have been implemented for the model. In the first case κ is prescribed as a constant, κ_0, and is thus independent of the density stratification. In the second case κ is taken to be inversely proportional to $\overline{\Delta\rho}$ (cf. eq. 7), which is the horizontal average of the top-to-bottom density difference. Specifically κ has been given the form:

$$\kappa = \kappa_0 \cdot \frac{\Delta\rho_r}{\overline{\Delta\rho}},$$

where $\Delta\rho_r$ is a density difference used for reference purposes, and

$$\overline{\Delta\rho} = \frac{1}{L}\int_0^L (\rho_{\text{top}} - \rho_{\text{bottom}})\, \mathrm{d}y,$$

where the integrand is the vertical density difference between the surface and the bottom. In order to prevent too high κ-values for weak density differences, an upper limit is set at $10 \cdot \kappa_0$.

3.4 Numerical procedures

Eq. (13) is discretized using a leap-frog scheme and the calculations are initiated using Eulerian forward stepping. At each time step the streamfunction is calculated by integrating eq. (15) twice. The spatial derivatives are discretized using centered differences. A staggered grid is employed, with the streamfunction in the corners and temperature and salinity at the center. The temperature and salinity resolutions are 51×41 in the horizontal and vertical direction respectively.

In order to ensure numerical stability, horizontal diffusion, Asselin filtering and horizontal three-point smoothing of the streamfunction are included in the computational scheme. The horizontal diffusivity constant

is taken to be 160 m^2/s and the Asselin time-filter constant is set to 0.1. Note that the horizontal diffusivity was taken to be as small as possible but yet large enough to suppresses numerical noise and instability. The present diffusivity value should be so low that it has no significant effect on the large scale flow. Convective adjustment following Yin and Sarachik (1994), has furthermore been incorporated to inhibit unstable stratification.

The fluid is initially at rest, at which time the temperature and salinity are taken to be constant in the basin. The time step used in the simulations is 12 hours. The model is run until a steady state has been reached.

3.5 Reference state

We introduce a reference state that broadly corresponds to the present-day ocean, specified by the following parameters: $\Delta T_r = 25$ °C, $\kappa_0 = 10^{-4}$ m^2/s, $D = 3000$ m, $B = 6000$ km, $L = 6000$ km, $\alpha = 2 \cdot 10^{-4}$ $°C^{-1}$, $\beta = 8 \cdot 10^{-4}$, $\gamma = 1.8 \cdot 10^{-3}$ s^{-1}. Note that γ should be regarded as a tuning parameter, here adjusted so that the model yields ocean-like results for the parameter values introduced above. Note further that the freshwater forcing is zero in the reference state and that the thermally induced equator-to-pole density difference, $\Delta\rho_r$, is 5 kg/m^3.

The reference state is the steady-state model solution that in the absence of freshwater forcing results from this parameter specification. In the reference state, the two mixing representations yield, by construction, an identical vertical diffusivity and consequently also identical model solutions. Fig. 4 shows the temperature distribution as well as the streamfunction for this thermally forced reference state. The resulting circulation is of the forward, thermally-dominated type, characterized by "narrow" sinking at high latitudes and "broad" upwelling at low latitudes. Note that the thermal stratification, with its well-defined thermocline, displays qualitative similarities with the real ocean.

It should be underlined that the reference state is characterized by a single non-dimensional parameter:

$$\sigma = (\gamma \rho_0 L^2/g)^{1/3} \cdot \kappa^{1/3} \cdot \Delta\rho^{-1/3} \cdot D^{-1}, \tag{16}$$

which controlls the ratio between the thermocline depth and the basin depth. Provided that this parameter is chosen to yield a realistic thermocline depth, the actual strength of the overturning is basically irrelevant for the dynamics of the model.

To compare the present simulations with previous numerical and analytical investigations, it is useful to introduce a non-dimensional measure of

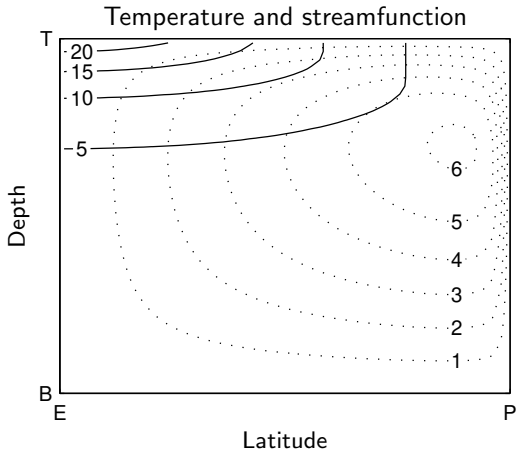

FIGURE 4: Reference state temperature (solid lines) and streamfunction (dotted lines) in the basin at steady-state, described in the text in section 3.5. The numbers are given in °C and Sv respectively. The x-axis is in the meridional direction and the y-axis in the vertical. E is the equator, P the pole, T the top and B the bottom.

the freshwater forcing, which is here termed R. This parameter is defined as the ratio between the haline buoyancy flux, due to the surface salinity flux, and the thermal buoyancy flux associated with the simulated poleward heat transport in the reference state (say Q_r). The former buoyancy flux is given by $\beta F_0 BL/\pi$; which implies that

$$R = \frac{\beta F_0 BL c_p \rho_0}{\alpha Q_r \pi}, \tag{17}$$

where c_p is the heat capacity of seawater. Note that it is F_0 that sets the strength of surface salinity flux and that $Q_r = 0.15$ PW.

It can be noted that the present tuning produces an overturning strength and a heat transport that are similar to those obtain from three dimensional models in comparable geometry (see e.g. Nilsson et al., 2003). The observed northward heat transport in the Atlantic, on the other hand, is on the order of 1 PW. This discrepancy in heat transports is related to wind-driven circulation as well as to the fact that the real Atlantic receives thermocline water that has upwelled in the Indo-Pacific basin.

4 Results

Two types of numerical experiments are presented in what follows: Those with only thermal forcing, and those where the circulation is forced by mixed boundary conditions. The thermal forcing is provided by the equator-to-pole surface temperature gradient, where the magnitude ΔT is changed for each simulation and the resulting steady-state is subsequently examined. For the experiments with mixed boundary conditions, a fixed equator-to-pole temperature gradient, $\Delta T = \Delta T_r$, is applied, whereas R the strength of the freshwater forcing, is varied for each simulation.

4.1 Thermal forcing

When the system only is subjected to thermal forcing, the salinity is set to zero and thus density is only a function of temperature. The investigation has been carried through on the basis of a series of experiments with the forcing being increased for each simulation, whereafter the overturning strength at steady-state has been measured. The magnitude of the forcing is given by ΔT and the strength of the steady-state overturning is measured by the maximum value of the streamfunction in a centrally located column, $\max_{z\in[0,D]}[\psi(y \sim L/2, z)]$. Fig. 5 shows the overturning strength as a function of the equator-to-pole temperature difference. In this diagram the results from the numerical experiments, together with the relationships obtained from the scale analysis (eq. 5, 8 and 9), are shown for the fixed as well as the stability-dependent diffusivity.

In the regime where the equator-to-pole temperature difference is sizable ($\Delta T \gtrsim 5$ °C), there is a qualitative difference between the overturning response for the two different diffusivity parameterizations. In agreement with the scale-analysis results (cf. eq. 5 and 8), the strength of the overturning intensifies with equator-to-pole temperature difference using the constant-diffusivity parameterization, whereas it becomes weaker for the stability-dependent diffusivity parameterization.

This may be contrasted with the behavior in the regime where the equator-to-pole temperature difference is small ($\Delta T \lesssim 5$ °C). Here the overturning strength increases with the temperature difference for both diffusivity representations. Consonant with the scale-analysis results (cf. eq. 9) the overturning strength is essentially proportional to the density contrast.

According to the theoretical considerations the response of the overturning is intimately related to the response of the thermocline depth, given as $H \sim \Delta T^{-1/3}$ and $H \sim \Delta T^{-2/3}$, respectively, for the two different diffusivity representations (cf. eq. 3). In order to investigate how the thermocline

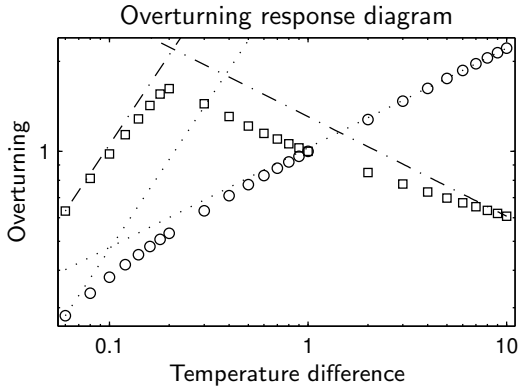

FIGURE 5: Response of the overturning as function of equator-to-pole temperature difference, ΔT, for constant (circles) and stratification dependent (squares) diffusivity, respectively. The flow is thermally forced and the overturning as well as the temperature difference is normalized at $\Delta T = \Delta T_r$. Numbers are non-dimensional. Dotted and dash-dotted lines are results of the scale analysis for constant and stratification dependent diffusivity, respectively (cf. eq. 5, 8 and 9). Axes are logarithmic.

depth varies with temperature difference in the model, a thermocline depth index H_T is defined as

$$H_T = \int_{-D}^{0} \frac{T(z) - T_{\text{bottom}}}{T_{\text{top}} - T_{\text{bottom}}} \, \mathrm{d}z, \tag{18}$$

where T_{top} and T_{bottom} is the temperature at the surface and bottom, respectively. The variation of thermocline depth with temperature difference is shown in Fig. 6. The variation of H_T in the model follows the predictions of the scale analysis in the regime where $\Delta T \gtrsim 5$ °C. In the region where $\Delta T \lesssim 5$ °C the thermocline depth index saturates close to 0.5, implying that the thermocline effectively has reached the bottom ($H \sim D$).

The overturning response in Fig. 5 and the thermocline depth response in Fig. 6 (shown for data from a column near the center of the basin) proved to be uniformly valid in the greater part of the basin. The exception is the region poleward of the global maximum of the streamfunction where downwelling occurs.

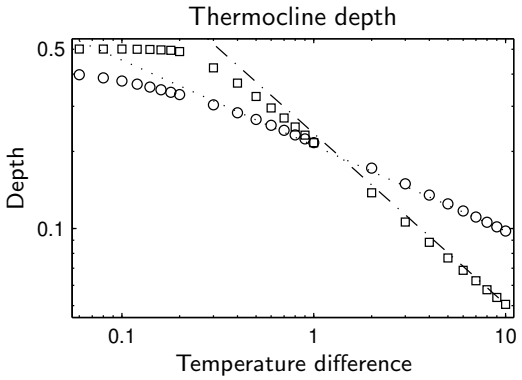

FIGURE 6: Thermocline depth index (cf. eq. 18) for constant (circles) and stratification-dependent (squares) diffusivity. The flow is thermally forced. Thermocline depth index for a column in the center of the basin as a function of equator-to-pole temperature difference. The depth index is normalized with the basin depth D and the temperature difference with ΔT_r. Numbers are non-dimensional. Dotted lines and dash-dotted lines are results from the scale analysis for constant and stratification dependent diffusivity, respectively. Axes are logarithmic.

4.2 Mixed boundary conditions

After noting the different responses depending on the representation of the diffusivity, it is of interest to analyze how freshwater forcing affects the circulation. The density is now a function of temperature as well as salinity, and consequently the salinity-flux and temperature boundary conditions jointly force the circulation. Note that, in contrast to the case when only thermal forcing is applied, the equator-to-pole surface density difference is not prescribed but dynamically determined by the flux condition at the surface. The thermal forcing is taken to be constant, but the intensity of the freshwater forcing is slightly varied between each simulation. In what follows the thermally dominated forward circulations are first analyzed, whereafter salinity-dominated, reversed circulations are dealt with separately. The steady state at $R = 0$ is identical to that obtained for the thermally forced simulation at $\Delta T = \Delta T_r$.

Fig. 7 shows the resulting strength of the streamfunction (defined above) as a function of the freshwater forcing. When the strength of the freshwater forcing is increased the circulation weakens for the constant-diffusivity case. The opposite is true when the stability-dependent diffusivity parameterization is used: A stronger freshwater forcing is now associated with a strong

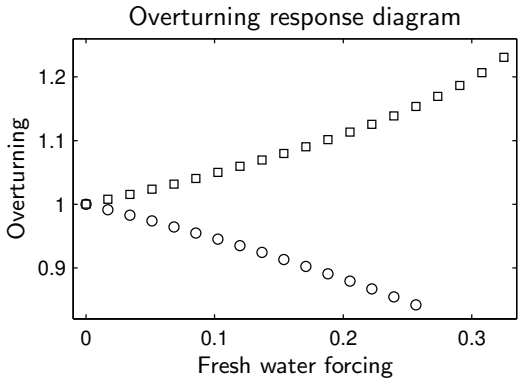

FIGURE 7: Response diagram of the overturning as function of the strength of the freshwater forcing, R, for constant (circles) and stratification-dependent (squares) diffusivity, respectively. Heat and freshwater force the circulation. The overturning is normalized at $R = 0$. Numbers are non-dimensional.

overturning. This is in broad agreement with the results from the thermally forced simulations (cf. Fig. 5): As the freshwater forcing is increased, the salinity contrast is magnified, implying that the equator-to-pole density difference weakens. This corresponds to a weaker equator-to-pole temperature difference in the simulations using only thermal forcing.

It should be emphasized that no steady forward circulations are found when $R > 0.33$. The underlying reason has to do with feedbacks between the circulation and the salinity fields, an issue which deserves a discussion. In the case with only thermal forcing there is a negative feedback between the temperature difference and the heat flux since a greater temperature difference results in an enhanced heat flux, independent of the diffusivity representation. The existence of solely a negative feedback implies that there is one single stable equilibrium state for each ΔT. However, the freshwater forcing introduces an additional feedback mechanism which makes the dynamics more complex.

To begin with, it should be recognized that the freshwater forcing acts to increase the equator-to-pole salinity contrast, regardless of the magnitude of the salinity contrast. In a steady state the advective salinity flux is the only mechanism capable of balancing the freshwater forcing. The feedback between the salinity difference and the advective salinity flux determines the stability of the system when it departs from a steady state. The essentials of this feedback are contained in the linearized evolution of a small perturbation on the basic equator-to-pole salinity contrast $\overline{\Delta S}$, as

the following schematic relation describes:

$$\frac{\mathrm{d}\Delta S'}{\mathrm{d}t} \propto -\Delta S' \cdot \overline{\psi} - \overline{\Delta S} \cdot \psi',$$

where overbars denote basic-state quantities and primes denote perturbations. The first r.h.s. term represents how the basic-state flow affects a perturbation in the salinity contrast. This part of the feedback is independent of the relation between density and circulation and is hence also independent of the diffusivity representation. It is negative definite, since the advection counteracts the salinity perturbation. The second r.h.s. term describes the interaction between a flow perturbation and the basic salinity contrast. This feedback depends on the relation between density difference and circulation. For constant diffusivity, as well as in the classical box model due to Stommel (1961), a positive perturbation in the salinity contrast gives rise to a decrease of the advection (relative the basic state). This will amplify the initial perturbation in the salinity contrast, hereby making this part of the feedback positive. Thus, the two feedback components counteract each other and the net feedback can be negative as well as positive. For the stability-dependent diffusivity, on the other hand, a positive perturbation in the salinity contrast implies an enhanced circulation. This will dampen out the salinity perturbation (implying that the second r.h.s. term constitutes a negative feedback). Hence, the total feedback is always negative.

Can these theoretical considerations serve to illuminate the model results? For the case when $\psi \sim \Delta\rho^{1/3}$ (corresponding to fixed diffusivity) and when the freshwater forcing is weak, the negative component of the feedback predominates. However, it weakens as the freshwater forcing gets stronger and the salt contrast builds up, whereas the positive part of the feedback becomes stronger. Freshwater forcing consequently destabilizes the circulation. At some stage the positive part of the feedback overwhelms the negative one and the system becomes unstable. Thus, there is no stable forward circulation when the freshwater forcing is stronger, but a reversed circulation is possible (a topic to be dealt with below). This behavior of the feedback proves to be qualitatively the same as in Stommel's model (Stommel, 1961). The present discussion suggests that the numerical model with fixed diffusivity yields an overturning that weakens with the density contrast up to a point where a forward circulation can not be found. Instead a steady-state reversed circulation is obtained.

For stability-dependent diffusivity ($\psi \sim \Delta\rho^{-1/3}$) the response should be fundamentally different, since the feedback always is negative. In the absence of a positive feedback the system should be stable, independent of the

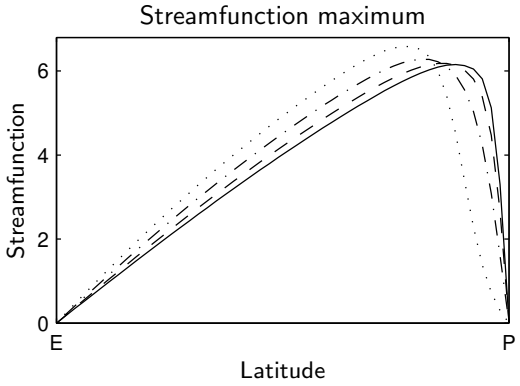

FIGURE 8: The meridional variation of the maximum of the streamfunction in each column with different freshwater forcings using stratification dependent diffusivity. The solid line shows the maximum of the streamfunction for no freshwater forcing ($R = 0$), the dashed line for $R = 0.10$, the dash-dotted for $R = 0.22$ and the dotted for $R = 0.32$. Numbers are given in Sv. The x-axis is in the meridional direction. E is the equator and P the pole.

strength of the freshwater forcing, i.e. no threshold levels should exist. Furthermore, salinity perturbations should be attenuated more rapidly when the freshwater forcing is strong. However, this is not the case in the numerical simulations. For $R > 0.33$ the model does not attain stable steady states but oscillating transient states. When attempting to explain why the model does not comply with the theoretical considerations, the effects of a finite basin depth could be relevant. According to the scale analysis, a bottom influence could reverse the relation between flow and density difference (cf. section 2.2). The pycnocline depth (not shown here) increases with freshwater forcing but has not reached the bottom when the forward circulation breaks down. At this stage $H_\rho < 0.3$, where H_ρ is defined similarly as H_T with temperature replaced by density. Thus bottom effects can be ruled out. A more probable explanation is that the scale analysis only applies in the region where upwelling occurs, i.e. equatorwards of the global maximum of the streamfunction. Fig. 8 shows the meridional variation of the maximum of the streamfunction. Equatorwards of the global maximum the streamfunction increases with the freshwater forcing while it decreases poleward of the global maximum. Thus, the discussion of feedbacks above does not apply in the poleward region. Here the feedback between salinity difference and advective salinity flux may well become positive. In fact in the simulation where the forward circulation broke down (at $R = 0.33$), a

salinity perturbation developed at high latitudes. As time progressed this perturbation grew in magnitude and extent. As a result, the cell of forward circulation receded equatorwards and vanished temporarily to be replaced by a reversed circulation. Eventually a quasi-periodic state was attained (discussed below).

Finally it is worth mentioning that the dependence of maximum heat flux on the freshwater forcing is similar to that of the overturning (cf. Fig. 7). Thus for constant diffusivity, the heat flux decreases with freshwater forcing, a dependence which is well established. A somewhat peculiar effect is that for the fixed-energy parameterization, the heat flux increases with freshwater forcing. Hence it is possible to maintain a strong heat flux for a weak density contrast.

Time-dependence

It was noted above that when the freshwater forcing exceeded $R = 0.33$, no steady-state solutions with forward circulation were obtained when the model had stability-dependent vertical mixing. For stronger freshwater forcing, the flow exhibited pronounced time-dependence. Although this issue lies outside the main focus of the present study, the dynamics of the time-dependent states warrant a brief comment. Consider to begin with Fig. 9(a), which shows the time evolution of the streamfunction at the center of the basin (for $R = 0.33$). As illustrated, the flow undergoes a quasi-periodic oscillation, alternating between a strong forward circulation and a weak reversed circulation. By inspecting the distribution of ψ in two the extreme phases of the oscillation (see Fig. 9(b) and 9(c)), the following picture emerges. In the phase of weak flow at the center of the basin, there are two distinct circulation cells: Forward flow occurs in the southern domain, whereas the northern domain is characterized by a weak reversed circulation. Formation of rather warm and saline deep water occurs between the two cells. In phases of strong flow, the forward circulation occupies the bulk of the basin. Here, broad down-welling occurs in the northern half of the basin. Thus, the oscillation brings the system from an essentially thermally dominated forward state to a hybrid state with partly reversed flow, and back again. Throughout the cycle, the haline- and thermal-density contributions are comparable in the northern part of the basin, which causes the density contrast to be weak in this region.

The oscillation described here kinematically resembles the "thermohaline flushings" that have been reported from several studies based on three-dimensional ocean models (e.g. Weaver et al., 1993). As in a typical cycle of

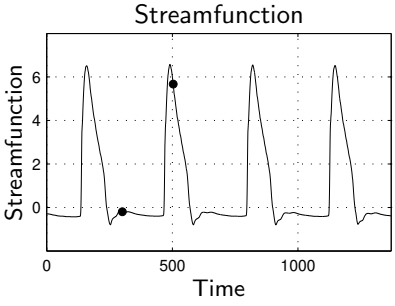

(a) Streamfunction at the center of the basin as a function of time with freshwater forcing at $R = 0.33$ using stratification dependent diffusivity. The bullets mark the weak and strong phases shown in Fig. 9(b) and 9(c), respectively. Numbers are given in Sv and years respectively.

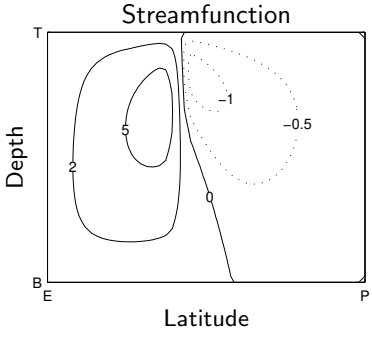

(b) Streamfunction at the weak phase at $t = 301$ years with freshwater forcing at $R = 0.33$ using stratification dependent diffusivity. Numbers in Sv. Solid contour lines corresponds to positive values and dotted to negative. The x-axis is in the meridional direction and the y-axis in the vertical. E is the equator, P the pole, T the top and B the bottom.

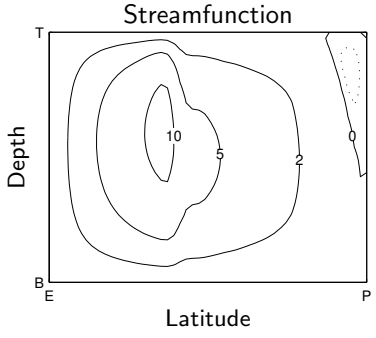

(c) As Fig. 9(b) but at the strong phase at $t = 503$ years.

FIGURE 9: Transient streamfunction.

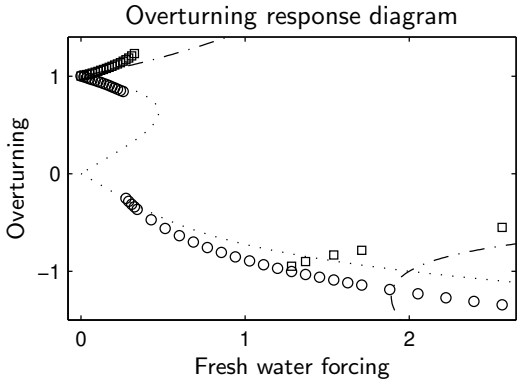

FIGURE 10: Response of the overturning as function of the strength of the freshwater forcing, R, for constant (circles) and stratification-dependent (squares) diffusivity, respectively. Heat and freshwater force the circulation. Dotted and dash-dotted lines lines are predictions from the conceptual model of Nilsson and Walin (2001) for constant and stratification dependent diffusivity, respectively. The overturning is normalized at $R = 0$. Numbers are non-dimensional.

thermohaline flushing, the present model produces relatively long dormant periods, followed by short bursts of intense forward circulation. It should be stressed, however, that the stability-dependent vertical mixing is crucial for the oscillations in our two-dimensional model; only steady equilibria are found when a constant vertical diffusivity is employed. Three-dimensional models, on the other hand, produce flushing cycles when the vertical diffusivity is taken to be fixed, as exemplified by the study of Weaver et al. (1993).

Reversed circulation

When the salinity field dominates the density distribution, the flow and the equator-to-pole density gradient become reversed. In this regime, narrow sinking occurs in low latitudes, which is compensated by broad upwelling over the rest of the basin. As the stratification is controlled by salinity, a stronger freshwater forcing now implies a more pronounced density difference. Essentially, this is the opposite of the state of affairs in the thermally dominated regime with forward circulation.

Fig. 10 provides an overview of all steady states that have been obtained in the numerical investigation. The figure also indicates the predictions from the conceptual model of Nilsson and Walin (2001) (illustrated

by the dotted lines). Consider first the reversed flow obtained when the model has constant diffusivity. As for the forward circulation, a stronger density difference implies a stronger circulation. Accordingly, the increase in circulation with increasing freshwater forcing, illustrated in Fig. 10, is expected. It is worth noting that the predictions from Nilsson and Walin (2001) describe reasonably accurately the forward as well as the reversed circulation in this case. Note further that no effort has been made to obtain reversed flow for weak freshwater forcing.

It proved more challenging to obtain stationary reversed flows when the stability-dependent mixing was employed. However, after extended numerical integrations a few equilibria were obtained. Fig. 10 shows that the reversed circulation slows down when the freshwater forcing increases. This behavior is analogous to the dynamics in the forward regime: A stronger freshwater forcing yields an enhanced (salinity-dominated) density contrast. This implies reduced vertical mixing which causes the thermocline depth to decrease to such an extent that the overturning slows down, despite an increased equator-to-pole density difference. As evident from Fig. 10, in this case the numerically simulated reversed circulation only qualitatively follows the conceptual model of Nilsson and Walin (2001). It is nevertheless of interest to note that the conceptual model predicts a threshold freshwater forcing, below which steady reversed circulation should be possible. The reason is that there now is a positive feedback between perturbations in salinity and circulation: A weaker salinity contrast yields a stronger flow, which in turn further reduces the salinity contrast. Thus it is essentially the same mechanism that destabilized the forward circulation when the vertical diffusivity is fixed.

5 Discussion

In our two-dimensional numerical model, the nature of the vertical mixing proved to be crucial for the response of the circulation to changes in the surface fluxes of heat and freshwater. When the vertical mixing was represented by a fixed vertical diffusivity, the forward circulation increased with increasing equator-to-pole density difference. This is the generally anticipated behavior, which has been reproduced in many numerical investigations (e.g. Park and Bryan, 2000). In contrast, when the vertical diffusivity decreased with stratification (at a rate that implied a fixed mixing energy) the opposite result was obtained: A weaker density difference yielded a stronger forward circulation.

This qualitative difference in the response of the circulation was encoun-

tered in the simulations with only thermal forcing as well as in those with mixed boundary conditions. For the stratification dependent mixing, the forward circulation intensified with increasing freshwater forcing. To our knowledge, this remarkable thermohaline response has not been reported from previous numerical investigations. A closer inspection of these simulations revealed that while the flow intensified in the bulk of the basin, it slowed down at high latitudes. The local freshwater hampering of the high-latitude circulation eventually destabilized the steady forward equilibrium; despite stronger freshwater forcing serving to augment the circulation in the greater part of the basin. However, the branch of thermally-dominated steady states was not succeeded by a salinity-dominated branch with reversed circulation (as was the case when a fixed diffusivity was employed). Rather, quasi-periodic flows resulted, which oscillated between phases of forward circulation of varying spatial extent and strength. It is interesting to note that the conceptual model due to Nilsson and Walin (2001) describes the simulated response of the forward circulation to freshwater forcing rather well for both mixing representations; see Fig. 10. However, the predictions of this model concerning the stability of the forward circulation proved to be less applicable to our numerical simulations. According to the conceptual two-layer model, the forward circulation should remain stable until the freshwater forcing is so strong that the pycnocline approaches the sea floor when stability-dependent mixing is employed. The forward circulation in the numerical model broke down well before that stage was reached. The most likely explanation is that the two-layer model, although relevant for steady state flows, does not resolve the spatial structure of the perturbations destabilizing the numerical model.

Are the results from this idealized study of relevance for the thermohaline circulation in the real ocean? To approach this question, it must be recognized that our knowledge of the vertical mixing in the ocean interior is far from complete (e.g. Toole and McDougall, 2001). Currently it is not known with any degree of precision how the turbulent vertical diffusivity would change in response to an altered vertical stratification in the World Ocean. Keeping this basic difficulty in mind, it is thus most relevant to ask whether the thermohaline circulation in more realistic models would be as sensitive to the nature of vertical mixing as it proved to be in our one-hemisphere zonally averaged model. To begin with, it can be stated that our model produces relations between the prescribed equator-to-pole temperature difference and the overturning strength that are similar to those obtained by Nilsson et al. (2003), who studied one-hemisphere flows using a three-dimensional model. Accordingly, for the purely thermally-

forced flows, the present zonally averaged model seems to give a reasonable description of the meridional overturning dynamics.

5.1 Relevance for two-hemisphere flows

The use of a one-hemisphere basin is an obvious limitation and motivates a comment of the relevance of our results for thermohaline flows in a two-hemisphere basin. Focusing on thermally forced flows, it can be noted that the studies by Klinger and Marotzke (1999) and Marotzke and Klinger (2000) demonstrate that even a weak pole-to-pole temperature (i.e. density) difference yields a flow that is strongly asymmetric with respect to the equator. Obviously, the present theoretical and numerical considerations provide no information on the dynamics controlling the asymmetry of these two-hemisphere flows. However, Klinger and Marotzke (1999) noted that the thermocline depth and the net overturning (i.e. the combined sinking in the two hemispheres) of the asymmetric flows scaled essentially as in the one-hemisphere case: In their simulations (where a fixed diffusivity was employed) the net overturning followed roughly $\Delta T^{1/3}$, where ΔT represented the largest equator-to-pole temperature difference (i.e. characterizing the hemisphere where the bulk of the sinking occurred). Based on the results of Klinger and Marotzke, it seems plausible that the present results apply qualitatively also for the net overturning of an asymmetric two-hemisphere flow, which essentially should be controlled by the basin-averaged vertical diffusivity and the maximum density contrast.

In the simulations with mixed boundary conditions, the one-hemisphere geometry introduces an additional problem: it excludes the possibility of equatorially asymmetric perturbations, which have a destabilizing influence of the symmetric thermally-dominated circulation in a two-hemisphere basin (Weijer and Dijkstra, 2001; Nilsson et al., 2004). It is well established that in a two-hemisphere basin the thermohaline circulation tends to attain an equatorially asymmetric state, rather than a state of reversed circulation, as the freshwater forcing is increased (Marotzke et al., 1988; Thual and McWilliams, 1992; Klinger and Marotzke, 1999). Welander (1986) suggested that the asymmetric thermohaline circulation conceptually can be viewed as a hybrid state, with thermal dominance in one hemisphere and haline dominance in the other. This idealized picture may suggest that our results concerning the effect of vertical mixing on the circulation in the forward and reversed regimes, respectively, can be translated to asymmetric circulations in a two-hemisphere system. However, this is probably misleading as there tends to be an element of pole-to-pole circulation in the

asymmetric regime, rather than two independent cells with different directions of flow (e.g. Klinger and Marotzke, 1999). Accordingly, the effect of a coupling between mixing and stratification on asymmetric two-hemisphere thermohaline circulation warrants further study.

5.2 Concluding remarks

It must further be emphasized that in our one-hemisphere model, the production and sinking of dense water must be balanced by the upwelling sustained by vertical mixing in the ocean interior. In the World Ocean, however, the wind directly forces upwelling in the Southern Ocean (Toggweiler and Samuels, 1995; Rahmstorf and England, 1997), where the surface Ekman drift carries cold water equatorwards. In fact, results from the conceptual model of Saenko and Weaver (2003) suggest that the overturning strength in the real ocean is probably less sensitive to the equator-to-pole density difference and the nature of vertical mixing than it is in our idealized one-hemisphere model; if the wind-forced Southern Ocean upwelling is fixed, it provides a baseline for the strength of the global overturning.

Furthermore, it should be underlined that our results concern the steady-state response of the thermohaline circulation to variations in the freshwater forcing. In the context of climate change – past as well as future – it may rather be the response of the thermohaline circulation to transient and abrupt changes of the surface forcing that matters. This transient type of response is of immediate relevance for how the thermohaline circulation will respond to future global warming (see e.g. Rahmstorf, 2000; Marotzke, 2000). In this context it is interesting to mention a recent coupled ocean-atmosphere study concerning the sensitivity of the Atlantic thermohaline circulation reported by Otterå et al. (2003). Starting from present-day climatic conditions, they introduced a strong fresh-water perturbation in the northern North Atlantic (0.2 Sv kept constant). Initially the Atlantic thermohaline circulation declined; however, after some fifty years the circulation started to regain strength and eventually stabilized. In the ocean model, Otterå et al. employed a stability-dependent vertical mixing. Based on analyses of the model result, they concluded that enhanced vertical mixing played an important role for the stabilization of the Atlantic circulation. Thus, it seems highly motivated to further explore to what extent the nature of vertical mixing may affect the dynamics of the thermohaline circulation.

Acknowledgments

This work was supported by the Swedish National Space Board and the Swedish Research Council. We would like to thank professor Peter Lundberg for discussions and valuable comments. We would also like to thank two anonymous reviewers for their constructive suggestions.

Bibliography

Huang, R. X., 1999. Mixing and energetics of the oceanic thermohaline circulation. Journal of Physical Oceanography 29 (4), 727–746, doi:10.1175/1520-0485(1999)029<0727:MAEOTO>2.0.CO;2.

Kato, H., Phillips, O. M., 1969. On the penetration of a turbulent layer into a stratified fluid. Journal of fluid mechanics 37, 643–655.

Klinger, B. A., Marotzke, J., 1999. Behavior of double-hemisphere thermohaline flows in a single basin. Journal of Physical Oceanography 29 (3), 382–399, doi:10.1175/1520-0485(1999)029<0382:BODHTF>2.0.CO;2.

Levitus, S., 1982. Climatological atlas of the world ocean. NOAA Professional paper 13, 173 pp.

Lyle, M., 1997. Could early cenozoic thermohaline circulation have warmed the poles? Paleoceanography 12 (2), 161–167, doi:10.1029/96PA03330.

Marotzke, J., 2000. Abrupt climate change and thermohaline circulation: Mechanisms and predictability. Proceedings of the National Academy of Sciences (U.S.A.) 97, 1347–1350, doi:10.1073/pnas.97.4.1347.

Marotzke, J., Klinger, B. A., 2000. The dynamics of equatorially asymmetric thermohaline circulations. Journal of Physical Oceanography 30 (5), 955–970, doi:10.1175/1520-0485(2000)030<0955:TDOEAT>2.0.CO;2.

Marotzke, J., Welander, P., Willebrand, J., 1988. Instability and multiple steady states in a meridional-plane model of the thermohaline circulation. Tellus, Series A 40 (2), 162–172.

Munk, W. H., 1966. Abyssal recipes. Deep-Sea Research 13, 707–730.

Munk, W. H., Wunsch, C., 1998. Abyssal recipes II: energetics of tidal and wind mixing. Deep-Sea Research, Part I 45 (12), 1977–2010, doi:10.1016/S0967-0637(98)00070-3.

Nilsson, J., Broström, G., Walin, G., 2003. The thermohaline circulation and vertical mixing: Does weaker density stratification give stronger overturning? Journal of Physical Oceanography 33 (12), 2781–2795, doi:10.1175/1520-0485(2003)033<2781:TTCAVM>2.0.CO;2.

Nilsson, J., Broström, G., Walin, G., 2004. On the spontaneous transition to asymmetric thermohaline circulation. Tellus, Series A 56 (1), 68–78, doi:10.1111/j.1600-0870.2004.00044.x.

Nilsson, J., Walin, G., 2001. Freshwater forcing as a booster of thermohaline circulation. Tellus, Series A 53 (5), 629–641, doi:10.1034/j.1600-0870.2001.00263.x.

Otterå, O. H., Drange, H., Bentsen, M., Kvamstø, N. G., D., J., 2003. The sensitivity of the present-day atlantic meridional overturning circulation to freshwater forcing. Geophysical Research Letters 30 (17), 1898, doi:10.1029/2003GL017578.

Park, Y.-G., Bryan, K., 2000. Comparison of thermally driven circulations from a depth-coordinate model and an isopycnal-layer model. Part I: Scaling-law sensitivity to vertical diffusivity. Journal of Physical Oceanography 30 (3), 590–605, doi:10.1175/1520-0485(2000)030<0590:COTDCF>2.0.CO;2.

Rahmstorf, S., 2000. The thermohaline ocean circulation: a system with dangerous thresholds? Climatic Change 46 (3), 247–256, doi:10.1023/A:1005648404783.

Rahmstorf, S., England, M. H., 1997. Influence of southern hemisphere winds on North Atlantic deep water flow. Journal of Physical Oceanography 27 (9), 2040–2054, doi:10.1175/1520-0485(1997)027<2040:IOSHWO>2.0.CO;2.

Saenko, O. A., Weaver, A. J., 2003. Southern ocean upwelling and eddies: sensitivity of the global overturning to the surface density range. Tellus Series A 55 (1), 106–111, doi:10.1034/j.1600-0870.2003.201518.x.

Stommel, H., 1961. Thermohaline convection with two stable regimes of flow. Tellus 13 (2), 224–230.

Thual, O., McWilliams, J. C., 1992. The catastrophe structure of thermohaline convection in a two-dimensional fluid model and comparison with low-order box models. Geophysical and Astrophysical Fluid Dynamics 64 (1–4), 67–95.

Toggweiler, J. R., Samuels, B., 1995. Effect of Drake Passage on the global thermohaline circulation. Deep-Sea Research, Part I 42 (4), 477–500, doi:10.1016/0967-0637(95)00012-U.

Toole, J. M., McDougall, T. J., 2001. Mixing and stirring in the ocean interior. In: Siedler, G., Church, J., Gould, J. (Eds.), Ocean Circulation and Climate. Vol. 77. Academic Press, Inc., pp. 337–356.

Weaver, A. J., Marotzke, J., Cummins, P. F., Sarachik, E. S., 1993. Stability and variability of the thermohaline circulation. Journal of Physical Oceanography 23 (1), 39–60, doi:10.1175/1520-0485(1993)023<0039:SAVOTT>2.0.CO;2.

Weijer, W., Dijkstra, H. A., 2001. A bifurcation study of the three-dimensional thermohaline ocean circulation: The double hemispheric case. Journal of Marine Research 59 (4), 599–631.

Welander, P., 1986. Thermohaline effects in the ocean circulation and related simple models. In: Willebrand, J., Anderson, D. L. T. (Eds.), Large-Scale Transport Processes in Oceans and Atmosphere. D. Reidel publishing company, pp. 163–200.

Wright, D. G., Stocker, T. F., 1991. A zonally averaged ocean model for the thermohaline circulation. Part I: Model development and flow dynamics. Journal of Physical Oceanography 21 (12), 1713–1724, doi:10.1175/1520-0485(1991)021<1713:AZAOMF>2.0.CO;2.

Wright, D. G., Stocker, T. F., Mercer, D., 1998. Closures used in zonally averaged ocean models. Journal of Physical Oceanography 28 (5), 791–804, doi:10.1175/1520-0485(1998)028<0791:CUIZAO>2.0.CO;2.

Yin, F. L., Sarachik, E., 1994. An efficient convective adjustment scheme for ocean general circulation models. Journal of Physical Oceanography 24 (6), 1425–1430, doi:10.1175/1520-0485(1994)024<1425:AECASF>2.0.CO;2.

Paper II

Symmetric and asymmetric modes of the thermohaline circulation

Rezwan Mohammad and Johan Nilsson

Under review in Tellus, Series A

Abstract

On the basis of a zonally averaged two-hemisphere ocean model, the present study investigates how the asymmetric thermohaline circulation depends on the equator-to-pole as well as the pole-to-pole density difference. Numerical experiments are conducted with prescribed surface density distributions as well as with mixed boundary conditions. Further, two different representations of the small-scale vertical mixing are considered, viz. constant and stability-dependent vertical diffusivity. The numerical results reveal that the horizontal structure of the flow is determined by the degree of equatorial asymmetry of the surface-density distribution, whereas the strength of the flow is controlled primarily by the equator-to-pole density difference. Provided that the shape of the surface density is invariant, the dependence of the strength of the asymmetric flow on the equator-to-pole density difference essentially follows the classical thermocline scaling pertaining to symmetric flows. In this case, the two diffusivity representations yield the opposite overturning responses to changes of the surface boundary conditions. However, if the shape of the surface density is changed, the symmetric scale analysis does not suffice to describe the dynamical response, which chiefly entails a spatial reorganization of the dynamical fields; in this respect there is no qualitative difference between the two parameterizations of the vertical mixing. For an asymmetric flow, subjected to mixed boundary conditions, an increase of the freshwater forcing primarily leads to an enhanced pole-to-pole density difference; an increase of the symmetric thermal forcing primarily augments the equator-to-pole density difference. Thus for a fixed freshwater forcing, an increase of the equator-to-pole temperature difference yields a weaker asymmetric circulation when the stability-dependent diffusivity is employed, whereas the reverse holds true for the constant diffusivity representation. Further, the numerical experiments show that the hysteresis characteristics of the asymmetric thermohaline circulation may be sensitive the nature of the small-scale vertical mixing.

1 Introduction

The small-scale vertical mixing, energetically sustained by winds and tides, is one of the key factors controlling the meridional overturning strength in the World Ocean (Wunsch and Ferrari, 2004). However, to quantify the importance of the vertical mixing for the driving of the meridional overturning has proved to be a challenging issue, which is still far from fully resolved: One school of thought (e.g. Munk and Wunsch, 1998) argues that the vertical mixing is crucial for the overturning as well as for its attendant heat transport; a contrary view (e.g. Toggweiler and Samuels, 1995) is that the overturning primarily is forced by wind-induced upwelling in the Southern Ocean.

The present study focuses on how the nature of the vertical mixing may impact on the overturning dynamics, in particular the equilibrium response of the overturning to changes in the surface boundary conditions. In order to study this issue in its purest and most simple form, all direct effects of wind-forced circulation are deliberately excluded from the present investigation. Thus, the primary aim here is to examine a process of geophysical relevance using a highly idealized representation of the ocean.

It is well established that, in the absence of wind forcing, the vertical diffusivity is a key factor controlling the meridional overturning strength in a single-hemisphere basin. Straightforward scaling arguments suggest that the overturning strength increases with the vertical diffusivity as well as with the equator-to-pole density difference, a relationship which has proved to be consonant with the outcome of many numerical studies (cf. Park and Bryan, 2000). Huang (1999) pointed out that if the energy supply to vertical mixing is taken to be fixed, the vertical diffusivity becomes inversely proportional to the vertical density difference. Under this assumption, the stronger density stratification associated with an enhanced equator-to-pole density difference serves to suppress the vertical diffusivity. A remarkable consequence of this coupling between the diffusivity and the stratification is that the overturning strength will decrease, rather than increase, with increasing equator-to-pole density difference. These somewhat counterintuitive results have recently been investigated using ocean circulation models of varying complexity (Huang, 1999; Nilsson et al., 2003; Mohammad and Nilsson, 2004; Otterå et al., 2003).

While the dynamical implications of stability-dependent diffusivity have been examined for a single-hemispheric basin, it is by no means straightforward to extrapolate these results to the overturning in the real ocean. A main difficulty is that the overturning in the World Ocean is asymmetric

with respect to the equator, a feature that can not be modeled using a single-hemisphere basin. In addition, wind-forced upwelling in the Southern Ocean is likely to exert control on the overturning strength (Toggweiler and Samuels, 1995; Rahmstorf and England, 1997; Klinger et al., 2003).

Before proceeding with the numerical modeling of a two-hemisphere basin which forms the core of the present study, it must again be underlined that the symmetric modes of the thermohaline circulation can be described using classical thermocline scaling (Welander, 1986). In this analysis the key quantities are the small-scale vertical mixing κ, the equator-to-pole surface density difference $\Delta\rho$, and the upwelling area A. The analysis yields that the thermocline depth should scale as

$$H \sim A^{1/3} \cdot \kappa^{1/3} \cdot \Delta\rho^{-1/3}, \tag{1}$$

and the strength of the circulation as

$$\psi \sim A^{2/3} \cdot \kappa^{2/3} \cdot \Delta\rho^{1/3}. \tag{2}$$

It should be noted that there currently exists no universal physical description of the vertical mixing in the ocean which predicts how κ depends on $\Delta\rho$ (cf. Toole and McDougall, 2001). When specifying κ it is of interest to compare the dynamical effects of two different assumptions of the physical nature of the small-scale vertical mixing: (i) constant diffusivity, as frequently used in ocean-circulation models, and (ii) a parameterization based on the more conservative hypothesis that the rate of energy available for the mixing is constant, viz. a stability-dependent diffusivity.

In the constant-diffusivity case the scaling implies that the relation between the strength of the circulation and the equator-to-pole density difference is $\psi \sim \Delta\rho^{1/3}$. If the mixing energy is taken to be constant, on the other hand, the diffusivity will depend on the vertical density difference according to $\kappa \sim \Delta\rho^{-1}$ (e.g. Huang, 1999; Nilsson and Walin, 2001). This yields the following scaling:

$$H \sim A^{1/3} \cdot \Delta\rho^{-2/3}, \tag{3}$$

$$\psi \sim A^{2/3} \cdot \Delta\rho^{-1/3}. \tag{4}$$

The response of the circulation thus differs fundamentally for the two parameterizations of the mixing: When the equator-to-pole temperature difference is taken to increase, the circulation is strengthened in the constant-diffusivity case, whereas it weakens for stability-dependent diffusivity.

The scope of the present study is thus to extend the previous analysis due to Mohammad and Nilsson (2004) in order to determine how a

stability-dependent vertical diffusivity affects the dynamics of equatorially asymmetric regimes of overturning. This issue will be investigated using the simplest possible geometry: a two-hemisphere basin. A zonally-averaged model similar to the ones previously employed in various climate studies (Wright and Stocker, 1991; Stocker et al., 1992; Wang and Mysak, 2000) will be employed in the numerical experiments. The presentation is organized as follows: The numerical model is described in section 2. The outcome of two sets of numerical experiments, the first employing thermal forcing only, and the other with mixed boundary conditions, is reported in section 3 and 4, respectively. In section 5, the main results are summarized and discussed.

2 The model

The zonally-averaged model employed for the present investigation is basically the one previously applied by Mohammad and Nilsson (2004). The main difference is that a two-hemisphere basin now will be used. Essentially, the derivation of the zonally averaged model equations follows Marotzke et al. (1988). The model describes a hydrostatic Boussinesq fluid, confined within a basin of constant depth D, zonal width B, and meridional length $2L$. The closure of the horizontal momentum equation is accomplished by assuming a proportionality between the east-west and north-south pressure gradients, which yields a linear relation between the meridional flow and pressure gradient (see e.g. Wright and Stocker, 1991; Wright et al., 1998).

The following equations govern the system:

$$\gamma v = -\frac{1}{\rho_0}\frac{\partial p}{\partial y}, \tag{5}$$

$$\frac{\partial p}{\partial z} = -\rho g, \tag{6}$$

$$\rho(T,S) = \rho_0\left(1 - \alpha T + \beta S\right), \tag{7}$$

$$\frac{\partial v}{\partial y} + \frac{\partial w}{\partial z} = 0, \tag{8}$$

$$\frac{\partial}{\partial t}\begin{pmatrix}T\\S\end{pmatrix} + v\frac{\partial}{\partial y}\begin{pmatrix}T\\S\end{pmatrix} + w\frac{\partial}{\partial z}\begin{pmatrix}T\\S\end{pmatrix} = \frac{\partial}{\partial z}\left(\kappa\frac{\partial}{\partial z}\begin{pmatrix}T\\S\end{pmatrix}\right). \tag{9}$$

Here v and w are the zonally-averaged meridional and vertical velocities, respectively, γ is a closure parameter relating flow speed and pressure gradient, ρ_0 is the reference density, p is the zonally averaged pressure, y is the meridional coordinate, z is the vertical coordinate, g is the gravity, T and S is the zonally averaged temperature and salinity, respectively, α and β are expansion coefficients for heat and salt, respectively, and κ is the vertical diffusivity.

No transports take place through the solid northern, southern and bottom boundaries. At the surface the salinity is dynamically controlled by a prescribed salinity flux F, given by

$$F(y) = -F_0 \cdot \cos\left(y \cdot \frac{\pi}{L}\right) = -\kappa \frac{\partial S}{\partial z},$$

where F_0 is the magnitude of the maximum salinity flux. The physical interpretation is that maximal net evaporation and precipitation takes place at the equator and the poles, respectively.

The sea-surface temperature is restored towards the following temperature distribution

$$T_{\text{top}}(y) = \begin{cases} \frac{\Delta T}{2} \cdot \left\{2\mu + (1-\mu) \cdot \right. \\ \left. \left[1 + \cos\left(y \cdot \frac{\pi}{L}\right)\right]\right\} & \text{for } y \leq 0, \\ \frac{\Delta T}{2} \cdot \left[1 + \cos\left(y \cdot \frac{\pi}{L}\right)\right] & \text{for } y > 0, \end{cases}$$

where ΔT is the equator-to-pole temperature difference[1]. The degree of sea-surface-temperature asymmetry is represented by a parameter μ, defined as the ratio between the pole-to-pole and the equator-to-pole temperature differences. Note that the sea-surface temperature is restored with a 1-day time scale, implying that the sea-surface temperature is essentially prescribed.

The diffusivity κ is parameterized in two ways: as constant (say κ_0) and in such a way that the rate of energy available for mixing (say $\mathcal{E}$) is constant, implying a stability-dependent diffusivity. Here $\mathcal{E}$, which equals the rate of increase in potential energy per unit area, is given by (see e.g. Munk and Wunsch, 1998)

$$\mathcal{E}(y) = \rho_0 \int \kappa N^2 \, \mathrm{d}z,$$

where N is the buoyancy frequency. In a stably stratified fluid, a non-zero κ thus leads to the creation of potential energy. Observations as well as

[1]The term equator-to-pole difference is here used to denote the difference between equator and the pole harboring the coldest (or most dense) surface water.

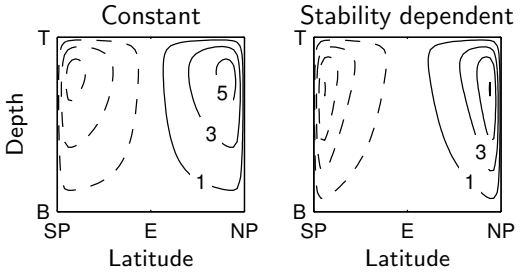

FIGURE 1: Reference-state streamfunction for constant (left panel) and stability-dependent diffusivity (right panel), respectively. Solid/dashed lines indicate positive/negative values. Note that although the diffusivity differs between the two models, they are tuned to have the same rate of potential energy generation in this reference state where $\mu = 0$ and $\Delta T = 25$ °C. The overturning strength is given in Sv.

theoretical considerations suggest that whereas κ is relatively uniform in the thermocline, it tends to increase towards the bottom, particularly in regions with rough bathymetry (e.g. Toole and McDougall, 2001; Simmons et al., 2004). For the sake of implicitly, however, the diffusivity κ is here taken to be vertically uniform over the entire depth, which implies that

$$\mathcal{E}(y) = g\kappa\Delta\rho(y),$$

where $\Delta\rho(y)$ is the vertical density difference between the bottom and the surface. When the diffusivity is stability-dependent $\mathcal{E}(y)$ is taken to be a constant specified by $\mathcal{E}_0$. This has the consequence that diffusivity varies horizontally according to

$$\kappa(y) = \frac{\mathcal{E}_0}{g\Delta\rho(y)}.$$

Here we choose $\mathcal{E}_0$ so that the global production of potential energy, i.e. $\int_{-L}^{L} \mathcal{E}(y)\,\mathrm{d}y$, is the same for both diffusivity representations in a reference state defined below. It should be noted that for the stability-dependent representation of the mixing, the vertical diffusivity increases with a decreasing stability of the water column. In order to preclude excessive κ-values in areas of weak density stratification, an upper limit is set at $10 \cdot \kappa_0$.

We introduce a reference state for which the freshwater forcing is taken to be zero (i.e. $F_0 = 0$) and the flow- and temperature-fields are symmetric (i.e. $\mu = 0$), see Fig. 1. The reference state is characterized by the following parameters: $\Delta T_r = 25$ °C, $\kappa_0 = 10^{-4}$ m^2/s, $D = 3000$ m, $B = 6000$ km,

$L = 6000\,\mathrm{km}$, $\alpha = 2 \cdot 10^{-4}\,{}^{\circ}\mathrm{C}^{-1}$, $\beta = 8 \cdot 10^{-4}$, $\gamma = 1.8 \cdot 10^{-3}\,\mathrm{s}^{-1}$. The thermally induced equator-to-pole density difference, $\Delta\rho_r$, is $5\,\mathrm{kg/m^3}$. Note that γ should be regarded as a tuning parameter, here adjusted so that the model yields ocean-like results for the parameter values introduced above. Note furthermore that the reference state will be employed to present the numerical results in non-dimensional form.

In the simulations conducted with mixed boundary conditions, the strength of the freshwater forcing is governed by a non-dimensional parameter R. This quantity is defined as the ratio between the haline buoyancy flux due to the freshwater forcing, and the thermal buoyancy flux associated with the meridional heat transport (say Q_r) in the reference state with zero freshwater forcing. The haline buoyancy flux is $\beta F_0 BL/\pi$, implying that

$$R = \frac{\beta F_0 B L c_p \rho_0}{\alpha Q_r \pi}, \tag{10}$$

where c_p is the heat capacity of sea water. Note that $Q_r = 0.16$ PW and $Q_r = 0.11$ PW in the reference simulations with constant and stability-dependent diffusivity, respectively.

3 Prescribed surface density

The asymmetric density field associated with a flow subjected to mixed boundary conditions is to some extent equivalent to the situation arising when a solely thermal asymmetric forcing is applied. Since the dynamics of a system forced by mixed boundary conditions are more complex, we will first study a thermally forced system without haline effects ($\beta = 0$), i.e. the density ρ is taken to only be dependent on the temperature T, $\rho = \rho(T)$.

When studying the response of the asymmetric modes it was found that the numerical results agreed qualitatively with the outcome of the scale analysis for the symmetric circulation mode if the degree of asymmetry was retained while the magnitude of the thermal forcing is varied (viz. a fixed μ and varying ΔT). When μ was varied (while ΔT was held constant) the results were less straightforward to interpret. It is thus instructive to first consider the asymmetric modes for a fixed μ and hereafter the case when μ is allowed to vary. Note that the majority of the results here are nondimensionalized with respect to the reference state, implying that the reference equator-to-pole temperature difference corresponds to $\Delta T = 1$.

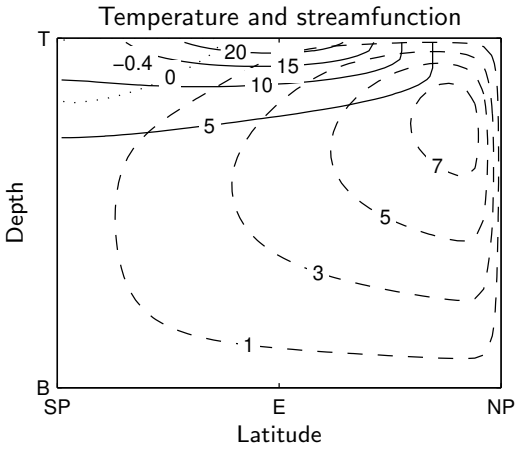

FIGURE 2: Steady-state temperature (solid lines) and streamfunction (dashed lines for positive values and dotted for negative) in the basin for $\mu = 0.5$, $\Delta T = 1$ and constant diffusivity. Values given in °C and Sv.

3.1 Fixed degree of asymmetry

In the numerical experiments reported in this section, the ratio between the pole-to-pole and the equator-to-pole temperature differences was held constant ($\mu = 0.5$), i.e. the shape of the forcing was retained. However, the equator-to-pole temperature difference ΔT was varied, and the model was integrated to a steady-state solution for each value of ΔT. Before studying the response of the overturning, it is instructive to examine the steady-state circulation for a given ΔT, cf. Fig. 2 where the circulation is highly asymmetric. A dominant circulation cell, attaining its maximum in the northern hemisphere, is seen to penetrate into the southern hemisphere to which a subordinate (i.e. weaker and more shallow) circulation cell is confined. Note that this latter cell is "squeezed" surfacewards in the extratropics.

Following Mohammad and Nilsson (2004), we introduce a thermocline-depth index that measures the vertical extent of the stratification. This quantity, to be compared with H in the scale analysis, is graphed in Fig. 3 versus the equator-to-pole temperature difference. For both representations of diffusivity, it is seen that the thermocline becomes more shallow with an increasing equator-to-pole temperature difference. When stability-dependent diffusivity is applied, however, the thermocline depth decreases more rapidly than in the constant-diffusivity case. It should also be noted

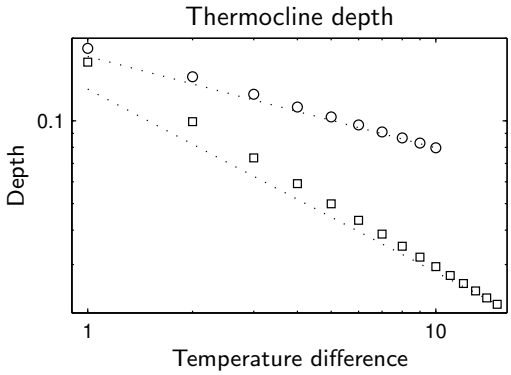

FIGURE 3: Thermocline depth index near the center of the southern hemisphere as a function of equator-to-pole temperature difference. The depth index is normalized with the basin depth D, the temperature difference with ΔT_r. Numbers are non-dimensional. Circles and squares represent results from the numerical model using constant and stability-dependent diffusivity, respectively, and dotted lines represent the results from the scale analysis. Axes are logarithmic.

the response of the thermocline-depth index is consonant with the predictions of the scale analysis, i.e. $H \sim \Delta T^{-1/3}$ and $H \sim \Delta T^{-2/3}$ for constant and stability-dependent diffusivity, respectively.

The good correspondence between the two sets of results shows that the scale analysis for symmetric flows also captures the asymmetric mode when μ is kept fixed at 0.5. It is expected that the numerical-model results will follow the scale relations also for other values of μ. It should be underlined that the results shown in Fig. 3 are representative of the response in the greater part of the basin, the most poleward regions being an exception. The overall numerical results also corroborate that the horizontal structure of the dynamical fields is independent of ΔT. It is only the vertical structure that is altered when ΔT is changed.

This can be further illuminated by analyzing the changes of the vertical temperature profiles as ΔT is increased (shown in Fig. 4 for constant diffusivity). First we plot the temperature profiles in a column near the center of the southern hemisphere in original dimensional form, shown in the left panel with one profile for each simulation corresponding to a specific ΔT-value. As this quantity is increased, the temperature in the whole column rises, the increase being largest in the thermocline. We hereafter normalize the profiles with ΔT, cf. the middle panel (where the order of the profiles has been reversed by the rescaling, the lowest-temperature pro-

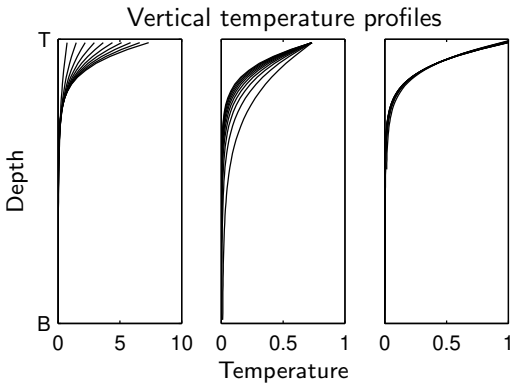

FIGURE 4: Vertical temperature profiles as functions of depth for constant diffusivity. The figures shows how the profiles merge after the analysis described in the text. Units in the left panel are in °C and non-dimensional in the other panels.

files now corresponding to the largest value of ΔT). Here it is evident that the thermocline becomes more shallow as ΔT is increased. Finally we stretch the vertical coordinate using the theoretical thermocline-depth scale ($H \sim \Delta T^{-1/3}$) as shown in the right panel. The profiles merge and we can once again conclude that the vertical structure is determined solely by ΔT, as assumed in the scale analysis.

A similar agreement between theory and numerical simulations is obtained for the response of the overturning-circulation strength to changes in ΔT, cf. Fig. 5. Thus the numerical results approximately follow the scale relations for a one-hemisphere flow: $\psi \sim \Delta T^{1/3}$ and $\psi \sim \Delta T^{-1/3}$ for constant and stability-dependent diffusivity, respectively. Here the strength of the overturning is measured by the maximum value of the streamfunction in a column located centrally in the hemisphere where the dominating circulation cell has its maximum, viz. $\max_{z\in[0,D]}[\psi(y \sim 3L/4, z)]$ where z is the vertical coordinate and D is the basin height. Although this diagram pertains to the maximum value of the streamfunction over a column in the dominating cell, it should be noted that analogous results are obtained also for the minor circulation cell.

The somewhat counter-intuitive result that the overturning strength decreases with increasing ΔT for the stability-dependent diffusivity parameterization relates to the fact that the intensity of the vertical mixing becomes weaker when the overall density difference is enhanced. The underlying dynamics can be illustrated as follows: In view of eq. (5), the

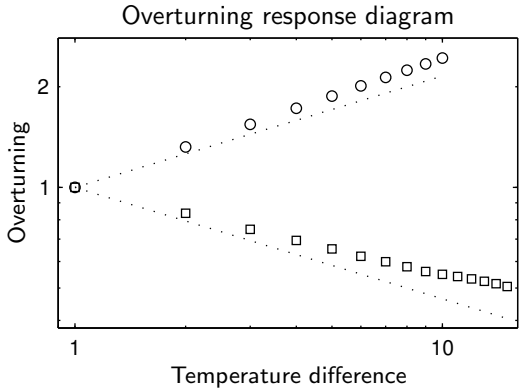

FIGURE 5: Overturning response versus the equator-to-pole temperature difference, ΔT. The overturning as well as the temperature difference are non-dimensional and normalized with respect to $\Delta T = \Delta T_r$. Circles and squares represent results from the numerical model using constant and stability dependent diffusivity, respectively, and dotted lines the scale analysis. Axes are logarithmic.

meridional velocity should scale as $v \sim \Delta T \cdot H$. Since $H \sim \Delta T^{-2/3}$ for the case with stability-dependent diffusivity, $v \sim \Delta T^{1/3}$. Hence the meridional velocity increases with increasing equator-to-pole temperature difference for both representations of the diffusivity. However, the volume transport associated with the overturning is proportional to $v \cdot H$. As a consequence, we obtain the scaling relation $\psi \sim \Delta T^{-1/3}$.

3.2 Varying degree of asymmetry

These numerical experiments were conducted by starting with a reference state where the thermal boundary condition is symmetric ($\mu = 0$ and $\Delta T = 1$) and hereafter increasing μ while holding ΔT fixed.

As illustrated in Fig. 2, varying the degree of asymmetry proved to completely change the structure of the temperature and streamfunction fields relative the symmetric circulation mode. The structural change between the symmetric and asymmetric modes can be described as follows: For symmetric thermal forcing the coldest water is found at the poles. When the pole-to-pole temperature difference, μ, is increased, the coldest surface water is still encountered at the poles in both hemispheres, whereas the warmest deep water is found at the south pole. Hence the horizontal temperature gradient is reversed below the thermocline. This is illustrated in Fig. 2 (for $\mu = 0.5$) with the isotherm labeled 5 °C deepening all the way

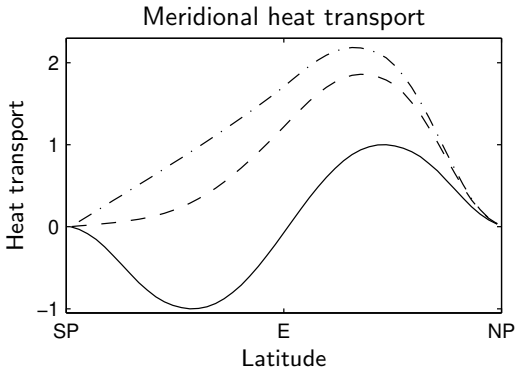

FIGURE 6: Meridional (northward) heat transport as a function of the latitude for constant diffusivity. The solid line represents the symmetric case when $\mu = 0$, the dashed line when $\mu = 0.5$ and the dash-dotted line the fully asymmetric case when $\mu = 1$. The heat transport is normalized with the maximum heat transport in the symmetric case.

towards the south pole, implying colder deep water at the equator than at the south pole.

The meridional heat transport, shown in Fig. 6, takes place from the equator towards the poles in the symmetric case. For $\mu = 0.5$ the transport southwards is weak or non-existent (despite the surface being colder at the south pole than at the equator), since the dominating circulation cell controls the heat transport in the southern hemisphere. The surface cooling in the southern hemisphere is most intense in the fully symmetric case and gets weaker as μ increases. In the completely asymmetric case there is no surface heat loss at all in the southern hemisphere, and the heat transport is directed northwards in the entire basin.

Fig. 7 shows the meridional heat transport versus the degree of asymmetry. The maximum poleward heat transport in the southern hemisphere is seen to decrease quite rapidly as μ grows, and becomes insignificant as μ approaches 0.5. The cross-equatorial northward heat transport for $\mu = 0.5$ is equally high as the maximum in the symmetric case. It should be emphasized that the responses for constant and stability-dependent diffusivities are qualitatively similar to changes in the degree of surface-density asymmetry.

Fig. 7 illustrates a key feature of the impact of asymmetric surface density forcing. Primarily, changes in the pole-to-pole density difference cause a spatial reorganization of the circulation. As the pole-to-pole density dif-

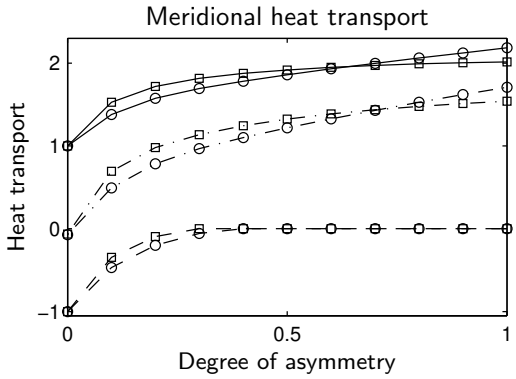

FIGURE 7: Meridional (northward) heat transport as a function of the degree of asymmetry for constant (circles) and stability-dependent diffusivity (squares). The solid and dashed lines show the maximum heat transport in the northern and southern hemisphere, respectively, and the dash-dotted line the heat transport at the equator. The heat transport is normalized with the maximum heat transport in the symmetric case.

ference is increased, the dominant cell grows spatially while the subordinate one shrinks. The decline in strength of the subordinate cell is nearly compensated for by a corresponding increase of the dominating cell. This state of affairs is visible in Fig. 7, showing that the net poleward heat transport is of the same order in the symmetric and the fully asymmetric cases (i.e. the maximum heat flux in the asymmetric case is roughly twice as large as in the symmetric case). This feature was also pointed out by Klinger and Marotzke (1999).

It is relevant to mention that these investigators, employing a three-dimensional model, conducted a similar investigation of the overturning-circulation response to asymmetric forcing. Qualitatively, their results agree with the outcome of the present investigation. One difference is, however, that the asymmetry of the circulation increases more rapidly with the pole-to-pole density difference in their three-dimensional model than it does for the present two-dimensional representation.

3.3 Dynamics of asymmetric circulations

As seen above, the horizontal structure of the circulation is considerably modified when the degree of asymmetry of the thermal forcing is varied. To illuminate the underlying dynamics we will discuss the difference between

the symmetric and the fully asymmetric case. We start by the following qualitative considerations: For a steady state and with constant diffusivity, the thermodynamic equation (9) is given by

$$v\frac{\partial T}{\partial y} + w\frac{\partial T}{\partial z} = \kappa\frac{\partial^2 T}{\partial z^2}.$$

The equivalent thermal wind equation (5) is

$$\frac{\partial v}{\partial z} = \frac{g\alpha}{\gamma}\frac{\partial T}{\partial y}.$$

Note that the prerequisite for a meridional circulation is that a horizontal temperature gradient be present. In its absence, v must be constant and equal to zero due to mass conservation and hence there will be no meridional circulation.

If we assume that the stratification is controlled by vertical advection and diffusion and that the vertical velocity is independent of depth, the following solution to the thermodynamic equation is obtained:

$$T(y,z) = T_s(y)\cdot e^{wz/\kappa}.$$

When $z \to -\infty$, $T \to 0$ which implies homogeneous bottom water with no horizontal gradients. Consonant with the advective-diffusive balance, the thermocline depth decreases with increasing w. The meridional derivative is

$$\frac{\partial T}{\partial y} = \left(\frac{\partial T_s}{\partial y} + T_s\frac{z}{\kappa}\frac{\partial w}{\partial y}\right)\cdot e^{wz/\kappa}.$$

The two derivatives $\frac{\partial T_s}{\partial y}$ and $\frac{\partial w}{\partial y}$ determining this temperature gradient may be of different signs and hence counteract one another. In the southern hemisphere an essential difference in the relative importance of these terms is found when comparing the symmetric and the fully asymmetric cases. For $\mu = 0$ there is a significant and dominating surface-temperature gradient, implying that $\frac{\partial w}{\partial y}$ is negligible. For $\mu = 1$ the opposite holds true, since the surface-temperature gradient is non-existent and $\frac{\partial w}{\partial y}$ alone must control the horizontal temperature gradient forcing the circulation.

This qualitative discussion is corroborated by Fig. 8 showing the meridional distribution of the vertical velocity. It is seen that the vertical velocity is more-or-less uniform for $\mu = 0$, and that the latitudinal variations of w are significant for $\mu = 1$. We can also note that even if there is no surface-temperature difference between the equator and the south pole when $\mu = 1$,

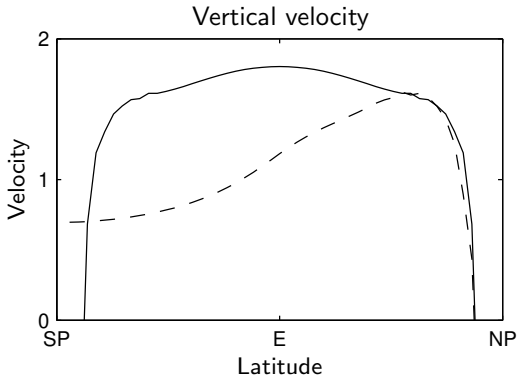

FIGURE 8: Vertical velocity as function of latitude at constant depth near the thermocline. The solid line pertains to the symmetric case ($\mu = 0$), and the dashed line to the fully asymmetric case ($\mu = 1$). Numbers are given in an arbitrary unit.

a meridional overturning circulation is maintained by the meridional density difference below the thermocline (cf. Fig. 2). This feature depends crucially on the meridional variations of the vertical velocity.

These considerations suggest that the advective-diffusive balance governs the stratification for the symmetric as well as the asymmetric flow regimes. For symmetric flows, the density gradient within the thermocline essentially mirrors the surface density gradient. For asymmetric flows, on the other hand, horizontal variations of the vertical velocity (yielding variations in the thermocline depth) are crucial for creating and maintaining the interior density gradients in the stagnant hemisphere.

4 Mixed boundary conditions

In the present section, the equilibrium response of the thermohaline circulation to changes of the surface freshwater flux will be examined. It should be noted that the surface freshwater flux in the real climate system is directly linked to the meridional moisture transport in the atmosphere. In all simulations considered here the sea-surface temperature is restored towards the equatorially-symmetric temperature profile specified in section 2. Following previous investigations (e.g. Marotzke et al., 1988; Thual and McWilliams, 1992; Klinger and Marotzke, 1999), numerical experiments with fixed thermal surface boundary conditions and varying freshwater forcing will be

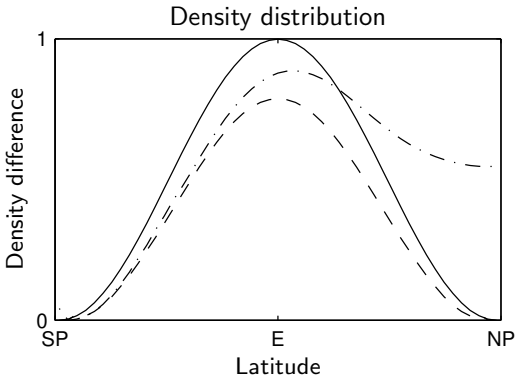

FIGURE 9: Distributions of surface density anomaly for $R = 0$ (solid line), $R = 0.31$ (dashed line) and $R = 0.38$ (dash-dotted line) in the constant-diffusivity case.

considered. In addition, also experiments with constant freshwater forcing and varying thermal surface forcing will be analyzed. The primary focus is on the dynamics of the asymmetric mode of thermohaline circulation, but a brief discussion of the symmetric mode is provided as a background. Note that the strength of the freshwater forcing is measured by the non-dimensional parameter R, being essentially the ratio between the haline and thermal buoyancy fluxes; see eq. (10).

4.1 Varying freshwater forcing

Here we consider the outcome of a suite of numerical calculations where R is gradually increased from zero while keeping the thermal surface forcing constant at $\Delta T = 1$. For each value of R in this suite, the model was integrated until it attained a steady state. As the freshwater forcing is increased, a symmetric salinity distribution develops that reduces the thermally imposed surface density gradient. In fact the temperature and salinity distributions are strongly correlated in the entire basin: waters with a high temperature also have a high salinity. As a consequence, the density contrast in the basin becomes weaker. This tendency is clearly illustrated in Fig. 9 and Fig. 11, pertaining to calculations using a constant vertical diffusivity. The results obtained using a stability-dependent diffusivity are qualitatively similar.

Below a threshold value of the freshwater forcing, the density field remains symmetric, while its amplitude becomes smaller. This decline of the

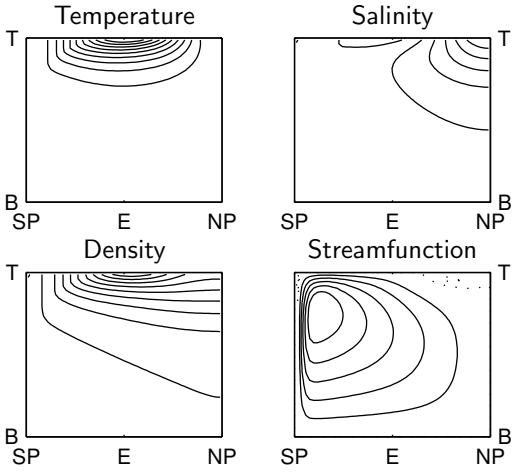

FIGURE 10: The structure of the temperature, salinity, density and streamfunction fields for an asymmetric steady-state solution forced by equatorially symmetric mixed boundary conditions, where $R = 0.38$ and constant diffusivity is applied. The isolines are for an arbitrary unit and are the same for the temperature and density fields. The streamfunction of the dominating cell and the subordinate cell is represented with solid lines and dotted lines, respectively. The x-axis is in the meridional direction and the y-axis in the vertical. E is the equator, SP and NP the south and north pole, respectively, T the top and B the bottom.

density contrast impacts on the strength of the symmetric overturning in accordance with the scaling relations, see eqs. (2) and (4). As illustrated in Fig. 12, the overturning strength becomes weaker when the freshwater forcing is increased in the model with constant diffusivity; the reverse holds true for the model with stability-dependent diffusivity. It should be noted that the meridional heat transport reflects the strength of the overturning. Thus, a noteworthy feature is that the nature of the vertical mixing decides whether the oceanic heat transport associated with a symmetric circulation will increase or decrease when the freshwater forcing is enhanced.

When the freshwater forcing exceeds a critical value, the flow undergoes a subcritical pitchfork bifurcation (Thual and McWilliams, 1992): the symmetric mode becomes unstable and is succeeded by a new asymmetric equilibrium solution (cf. Fig. 10). The underlying physics are that basin-scale antisymmetric perturbations now may amplify due to a positive feedback between flow- and salinity-anomalies (e.g. Walin, 1985; Vellinga, 1996; Dijk-

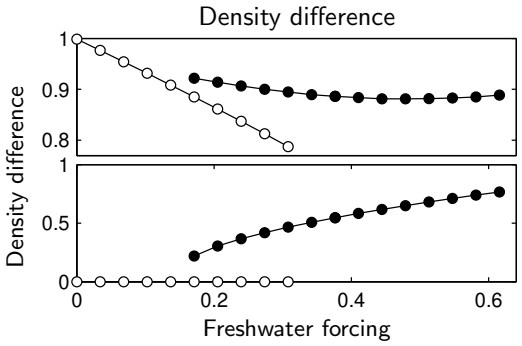

FIGURE 11: Surface density differences as function of freshwater forcing, R, pertaining to the constant diffusivity case. Upper and lower panels show the equator-to-pole and pole-to-pole surface density difference, respectively. The open circles represent the symmetric circulation mode and the filled circles the asymmetric mode. Note that the response of the surface density distribution is qualitatively similar in the case with stability-dependent diffusivity.

stra and Molemaker, 1997). The study due to Nilsson et al. (2004) suggests that the stability of the symmetric equilibrium is primarily controlled by the ratio between the haline and the thermal density differences and, furthermore, that the dynamics of the destabilizing antisymmetric perturbations are basically independent of the nature of the vertical mixing. Hence, the symmetric flow should become unstable when the ratio $\beta\Delta S/(\alpha\Delta T)$ exceeds a certain threshold, irrespective of how the vertical mixing is parameterized. For the present model the threshold value of $\beta\Delta S/(\alpha\Delta T)$, based on the surface fields, proved to be about 0.2. Note that the pitchfork bifurcation gives rise to two asymmetric equilibrium solutions, which are mirror images of one another. Which of these states is realized depends on the details of the perturbation destabilizing the symmetric flow.

Fig. 9 illustrates how the surface density distribution changes in the transition from a symmetric state to an asymmetric one. It is evident that the equator-to-pole density difference becomes slightly larger after the transition. More dramatic, however, is the associated growth of the surface density anomaly in the high northern latitudes, where a stable salinity stratification emerges. As the surface temperature field is virtually constant in the simulations, the changes of the surface density are entirely due to a reorganization of the salinity field (cf. Fig. 10).

We now focus on the response of the asymmetric mode to varying freshwater forcing. An inspection of Fig. 11 reveals that the degree of asymmetry

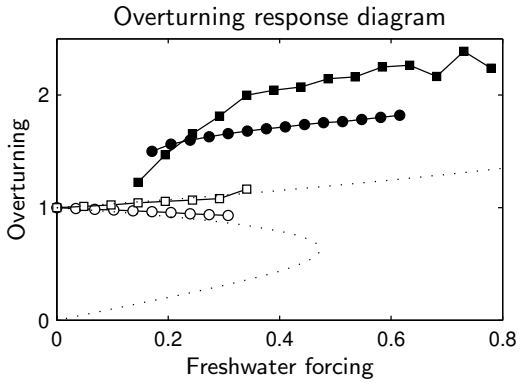

FIGURE 12: The overturning strength as function of R. Circles and squares pertain to constant and stability-dependent diffusivity, respectively, and open/filled symbols represent symmetric/asymmetric modes. The overturning is measured by its maximum value in a mid-latitude column located in the hemisphere where the dominating cell has its main abode for the asymmetric modes. Note the overturning strength is presented in nondimensional form and normalized to be unity when $R = 0$. The dotted lines show theoretical predictions due to Nilsson and Walin (2001). Note further that the asymmetric solutions obtained for the largest values of R, using stability-dependent mixing, exhibited a weak time dependence.

of the surface density field grows with the freshwater forcing. It should be noted that it is primarily the pole-to-pole density difference which changes, whereas the density difference between the equator and the pole (where the deep water is formed) remains essentially unchanged. Basically, the response of the distribution of density and flow is similar to that examined in section 3.2, where the asymmetry parameter μ was increased while keeping the equator-to-pole density difference fixed. Fig. 12 shows that the freshwater forcing enhances the intensity of the dominant cell, while the subordinate cell simultaneously declines. Note that this holds true for both representations of the mixing. Actually, in a qualitative sense, the flow response appears to be insensitive to the nature of the vertical mixing.

The response of the asymmetric modes to changes of the freshwater forcing can be understood as follows: First it should be recognized that the surface density in the polar region where the deep water is formed is basically unchanged: Due to pronounced sinking motion and the associated convective mixing, the surface water in this region will have the same salinity as the bulk of the deep water, i.e. essentially the mean oceanic

salinity (Wang et al., 1999). Near the opposite pole, where a stable salinity stratification is encountered, entirely different processes regulate the surface salinity. Even for a moderate degree of asymmetry, the subordinate cell is so weak that its advective salinity flux becomes negligible. Thus, in the stagnant hemisphere the high-latitude surface freshwater flux must be balanced by a vertical diffusive salinity flux. The upwelling associated with the main overturning cell serves to keep the halocline depth in the stagnant hemisphere relatively constant even though R is changed in the numerical experiments. Since the deep water salinity and the depth of the halocline remain essentially unchanged, the high-latitude surface salinity should decline linearly with increasing R in order to give rise to the required diffusive salinity flux. As a consequence, the pole-to-pole salinity difference (and thereby the density difference) will grow with increasing freshwater forcing. This furthermore serves to explain why the equator-to-pole density difference, reflecting the equatorial surface salinity, is relatively insensitive to R: Stronger freshwater forcing enhances the main overturning cell and its associated salinity transport. Thus a higher value of R leads to a stronger advective salinity flux within the dominant cell, which ameliorates the growth of the equatorial near-surface salinity.

It is relevant to note that the conceptual box model due to Rooth (1982) captures some qualitative aspects of the asymmetric flow simulated by the present numerical model. According to the model of Rooth, the pole-to-pole density difference as well as the overturning strength should be proportional to $R^{1/2}$ (Rahmstorf, 1996; Scott et al., 1999)[2]. As illustrated in Figs. 12 and 13, the dependence of the dominating cell on R is indeed slightly weaker than linear. However, the qualitative physical arguments given above suggested a linear R-dependence of the pole-to-pole density (i.e. salinity) difference. In fact, this would provide a somewhat better fit to the results displayed in Fig. 11. It is evident, however, that the numerically calculated pole-to-pole density differences conform strictly to neither the $R^{1/2}$-dependence nor to the R-dependence. Note furthermore that the model of Rooth predicts the existence of asymmetric steady states for arbitrarily weak freshwater forcing, a state of affairs in conflict with the outcome of many numerical investigations (cf. Thual and McWilliams, 1992; Vellinga, 1996; Dijkstra and Molemaker, 1997) including the present one.

While the response of the asymmetric flow to freshwater forcing is qualitatively similar for the two representations of diffusivity, there are two

[2]Note that Rooth's model yields the $R^{1/2}$-dependence when the pole-to-pole temperature difference is zero.

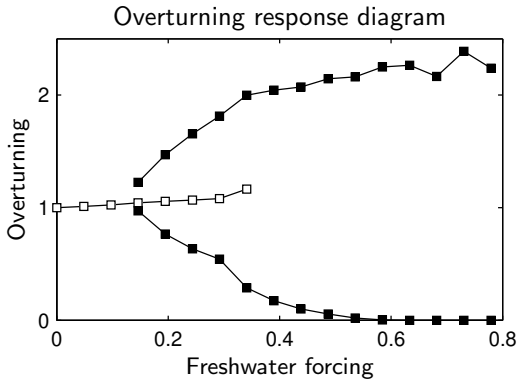

FIGURE 13: The overturning strength as function of R for stability-dependent diffusivity. Open/filled symbols represent symmetric/asymmetric modes. For the asymmetric mode, the responses of the dominating and the subordinate cells are shown, measured by the maximum overturning in a mid-latitude column in each hemisphere. Note that the subordinate cell vanishes for stronger freshwater forcing.

differences that deserve to be emphasized. First, the degree of asymmetry of the flow is more sensitive to the freshwater forcing when the diffusivity is stability dependent; compare the response of the dominating cell in Fig. 12. The underlying physics are related to the coupling between the density stratification and the vertical diffusivity, and can be illuminated as follows: In the stagnant hemisphere, where a stable salinity stratification forms, the vertical diffusivity is suppressed. In this region, the surface salinity must thus decrease further to accommodate the diffusive salinity flux dictated by the prescribed surface freshwater forcing. As a consequence, the pole-to-pole density difference and the strength of the dominating cell react more strongly to changes in the freshwater forcing in the model using the stability-dependent diffusivity.

Second, the stability-dependent diffusivity allows for equilibrium solutions, belonging to the asymmetric branch, which only shows a very weak degree of asymmetry; see Fig. 13. This has important consequences for the hysteresis characteristics of the system. Suppose that the flow is in an asymmetric state and that the freshwater forcing is very slowly decreased. For the case with stability-dependent diffusivity, the flow would gradually become less asymmetric, ending with a nearly continuous transition to the branch of symmetric equilibrium solutions. For the case with constant diffusivity, on the other hand, the transition to the symmetric branch would

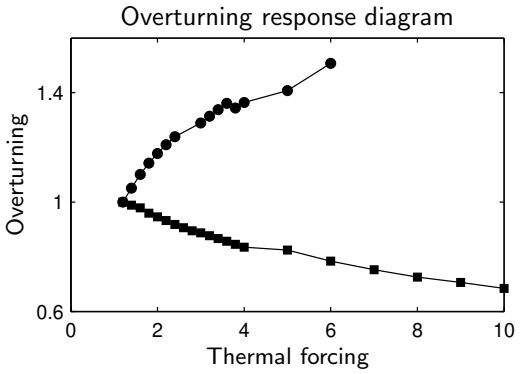

FIGURE 14: The response of the dominant cell to changes of ΔT for fixed freshwater forcing. Circles and squares pertain to constant and stability-dependent diffusivity, respectively. The overturning is measured by its maximum value in a mid-latitude column in the hemisphere where the dominating cell has its main abode. The overturning strengths are normalized at $\Delta T = 1$. Note that no asymmetric solutions were obtained for $\Delta T > 6$ when constant diffusivity was employed.

be abrupt and associated with a dramatic reorganization of the flow structure. It should be noted that the transition from the symmetric branch to the asymmetric one is abrupt for both representations of κ.

4.2 Varying thermal forcing

From a climate-change perspective, it is of interest to also examine how the asymmetric mode of thermohaline circulation responds to changes in the thermal boundary conditions for a fixed freshwater forcing. Therefore we have conducted a series of numerical calculations, starting with the asymmetric flows obtained for $R = 0.5$ and $\Delta T = 1$, where steady-state solutions were calculated for increasing values of ΔT, keeping the freshwater forcing constant. This implies that the steady-state meridional transport of salinity was the same in all simulations, although the salinity field was subjected to changes. Note also that for increasing ΔT, the parameter R decreases, demonstrating a decline of the relative strength of the freshwater forcing; see eq. (10).

The outcome of the numerical calculations can be summarized as follows. When the amplitude of the symmetric surface temperature was enhanced, the degree of asymmetry of the density field weakened, i.e. the ra-

tio between the pole-to-pole and equator-to-pole density differences became smaller. Primarily, this is attributable to a strengthening of the equator-to-pole density difference created by the temperature field. In fact the salinity field, and thereby also the pole-to-pole density difference, remained relatively constant for the solutions obtained in the range $1 < \Delta T < 3$. For stronger thermal forcing, however, the amplitude as well as the degree of asymmetry of the salinity field decreased with increasing ΔT. This behaviour was identified for both representations of the diffusivity. As shown in Fig. 14, the response of the dominating cell to changes in ΔT proved to be more subtle. In the model using stability-dependent diffusivity, the dominant cell becomes weaker when the equator-to-pole difference is enhanced, whereas the opposite holds true in the case of the constant-diffusivity model.

Essentially, the changes of the overturning strength can be understood on the basis of the results presented in section 3: The strength of an asymmetric flow is basically proportional to that of a symmetric flow forced by the same overall density difference; the degree of density asymmetry determines primarily the partitioning between the dominant and the subordinate cell. Thus for a constant freshwater forcing, an increase of ΔT impacts on the strength of the dominant cell in two different ways. To begin with, the associated reduction in the degree of asymmetry tends to decrease the dominant cell. However, the strength of the flow is also affected by the change of overall density contrast, which increases with ΔT. Thus if the vertical diffusivity depends on the stability of the water columns, the dominant as well as the subordinate cell should tend to decline in response to a stronger equator-to-pole temperature difference. For the dominant cell this response serves to reinforce the alterations induced by the reduced degree of asymmetry. Hence when the stability-dependent diffusivity is employed, the strength of the dominant cell should decline when ΔT is increased for a constant freshwater forcing.

Basically, the reverse applies if the vertical diffusivity is taken to be constant and thus independent of the density stratification. In this case, the overall amplitude of the flow should tend to grow with increasing ΔT. This tendency of the dominant cell to strengthen thus serves to counteract the change caused by the reduction of the density asymmetry. In the present numerical simulations, the enhancement of the equator-to-pole density difference controlled the dominant-cell response, which intensified as ΔT was augmented.

It should further be noted that the model based on stability-dependent mixing yielded asymmetric equilibrium solutions for all the ΔT values in

the suite of experiments. When constant diffusivity was employed, the asymmetric solution became unstable when ΔT exceeded 6. For stronger temperature differences, only symmetric steady states were obtained.

5 Discussion

The present study has focused on the dynamics of symmetric and asymmetric modes of the thermohaline circulation in a two-hemisphere basin. Using a zonally-averaged numerical model, the dependence of the circulation on the equator-to-pole as well as the pole-to-pole density difference has been systematically examined. When the latter quantity is zero, the thermohaline circulation is symmetric, and the dynamical response to changes of the surface boundary condition can be described with a simple scale theory showing that the response is sensitive to the physical representation of the small-scale vertical mixing (Welander, 1986; Nilsson and Walin, 2001; Mohammad and Nilsson, 2004). If, on the other hand, the pole-to-pole density difference is non-zero, the flow becomes asymmetric. In this case, the symmetric scale theory is still applicable, provided that the overall distribution of the surface density is preserved. However, if this distribution is permitted to change, the symmetric scale analysis does not suffice to describe the response of the circulation, which primarily entails a spatial reorganization of the dynamical fields. For an increasing pole-to-pole surface density difference, the dominating circulation cell is dilated at the expense of the subordinate cell (Wang et al., 1999). The combined overturning strength of the two cells only shows modest variations. Note that in this respect there is no qualitative difference with regard to the two parameterizations of the vertical mixing. In summary, the nature of the vertical mixing appears to be crucial for the equilibrium response of the asymmetric thermohaline circulation when changes of the surface boundary conditions lead to alterations of the density difference between the equator and the pole harboring the densest surface water (simply denoted the equator-to-pole density difference here).

We believe that the results from the present idealized model may serve to illuminate how the nature of vertical mixing affects the dynamics of a two-hemisphere thermohaline circulation. Thus, our investigation should provide some qualitative information concerning possible impacts of the vertical mixing on the overturning in the real ocean. However, we underline that several geophysically relevant processes and features are absent in the present model. Presumably, the absence of wind forcing and the use of a single basin lacking a periodic "Southern Ocean" are the most severe

idealizations underlying the present study. As demonstrated by Toggweiler and Samuels (1995) as well as Klinger et al. (2003), the impact of wind forcing on the overturning dynamics is significant in ocean basins with circumpolar communication. Furthermore, it would be relevant to examine whether the results from the presently employed zonally-averaged model are robust in the sense that they essentially can be reproduced by a three-dimensional general circulation model.

Keeping the idealized nature of the present model in mind, we proceed to speculate on the character of an asymmetric thermohaline circulation in a changed climate. Specifically, we consider a very slow shift of the climatic conditions, which involves an alteration of the surface heat- and freshwater-fluxes. For a single-hemisphere thermohaline circulation, the equilibrium response to such a change will depend crucially on the physics of the vertical mixing, as discussed by e.g. Huang (1999); Nilsson et al. (2003) as well as Mohammad and Nilsson (2004). What do the present results suggest about the response of an asymmetric circulation? Unlike the single-hemisphere case, the details of the changes in the surface forcing appear to decide whether the vertical mixing controls the response of the asymmetric flow. For instance an increase of the freshwater forcing primarily leads to an enhanced pole-to-pole density difference, implying that the dominant cell intensifies irrespective of the features of the vertical mixing. The underlying reason is that the area of the dominant cell expands across the equator into the stagnant hemisphere. Evidently, this structural reorganization has no counterpart in a single-hemisphere basin. It is relevant to note that results from ocean-circulation models reported by Wang et al. (1999) as well as Klinger and Marotzke (1999) also show that a spatially uniform increase in the surface freshwater forcing tends to promote the overturning cell that feeds the dominant deep-water formation site.

It should be noted, however, that a climate change is expected to be associated with alterations of the thermal forcing as well as of the freshwater forcing. Throughout the Earth's history, the meridional gradient of the surface air temperature has varied considerably, being weak during hot-house climate regimes (e.g. the Cretaceous) and strong during glacial climates, cf. Pierrehumbert (2002). The question then is how the hydrological cycle responds when the equator-to-pole temperature difference is altered. To limit the scope of our discussion, we focus on a warm climate characterized by an equator-to-pole temperature difference that is smaller than that of the present-day climate. Results from atmospheric general circulation models suggest that the atmospheric poleward flux of moisture in the midlatitudes should slightly increase in a warm low-gradient climate (Pierrehumbert,

2002; Caballero and Langen, 2005). It should be recognized, however, that the moisture flux is affected by two counteracting processes. First, the temperature increase, which permits a higher atmospheric moisture content. Second, the decrease in temperature gradient, which serves to curtail the midlatitude eddies that carry the moist air poleward. Depending on the details of temperature distribution in the hypothetical warm climate, the moisture flux could thus be stronger as well as weaker than that in the present-day climate (Caballero and Langen, 2005).

For the sake of argument, we assume that the moisture flux is enhanced in our hypothetical warm climate. Assuming further that the energy supply to small-scale mixing is invariant (i.e. stability-dependent diffusivity), we expect to observe the following changes of the asymmetric overturning circulation: To begin with, the combined effect of an increase in freshwater forcing and a decrease in ΔT will enhance the degree of asymmetry of the flow- and density-distributions. Moreover, the decline of the overall oceanic density contrast will be associated with a strengthening of the dominant cell; cf. section 3.1. Thus the present idealized study suggests that warm climates should be associated with a stronger overturning circulation and hereby a more rapid ventilation of the deep ocean. Evidently, this could have important implications for the biogeochemistry of the ocean. However, the sensitivity of the overturning strength on ΔT is rather weak (see Fig. 14). In fact, the present numerical results indicate that the oceanic heat transport would be diminished in the hypothetical warm climate, despite the overturning strength being enhanced. It deserves to be underlined that the overturning strength as well as the heat transport would decline if the vertical diffusivity instead would have remained constant.

Finally it is worth noting that these considerations bear some relevance for the question whether intense oceanic heat transport could have warmed the poles during past low-gradient climates (e.g. Lyle, 1997; Pierrehumbert, 2002). The present idealized-model results seem to suggest that it is not sufficient to keep the energy supply to small-scale mixing constant in order to drive an enhanced oceanic heat transport in a climate with a reduced equator-to-pole temperature difference. Rather, the rate of energy supply to the small-scale turbulent motion that sustains the vertical mixing presumably needs to be increased. In this context, it is of interest to note that Emanuel (2002) has proposed a mechanism for amplifying the oceanic heat transport in a warm low-gradient climate. Based on thermodynamical considerations, he has showed that the intensity of tropical cyclones should increase in a warmer climate. Thus, the response of the global tropical cyclone activity serves to enhance the wind-driven mixing in the ocean.

Provided that this mixing is sufficiently intense, the oceanic heat transport may be ramped up. Thus, as a final comment, the present work serves to illuminate the potential link between warm climatic regimes and alterations of the energy supply to small-scale mixing in the interior of the ocean.

Acknowledgments

This work was supported by the Swedish National Space Board and the Swedish Research Council.

Bibliography

Caballero, R., Langen, P. L., 2005. The dynamical range of poleward energy transport in an atmospheric general circulation model. Geophysical Research Letters 32, doi:10.1029/2004GL021581.

Dijkstra, H. A., Molemaker, M. J., 1997. Symmetry breaking and overturning oscillations in thermohaline-driven flows. Journal of Fluid Mechanics 331, 169–198, doi:10.1357/002224001762842208.

Emanuel, K., 2002. A simple model of multiple climate regimes. Journal of Geophysical Research 107 (D9), doi:10.1029/2001JD001002.

Huang, R. X., 1999. Mixing and energetics of the oceanic thermohaline circulation. Journal of Physical Oceanography 29 (4), 727–746, doi:10.1175/1520-0485(1999)029<0727:MAEOTO>2.0.CO;2.

Klinger, B. A., Drijfhout, S., Marotzke, J., Scott, J. R., 2003. Sensitivity of basinwide meridional overturning to diapycnal diffusion and remote wind forcing in an idealized Atlantic-Southern Ocean geometry. Journal of Physical Oceanography 33, 249–266, doi:10.1175/1520-0485(2003)033<0249:SOBMOT>2.0.CO;2.

Klinger, B. A., Marotzke, J., 1999. Behavior of double-hemisphere thermohaline flows in a single basin. Journal of Physical Oceanography 29 (3), 382–399, doi:10.1175/1520-0485(1999)029<0382:BODHTF>2.0.CO;2.

Lyle, M., 1997. Could early cenozoic thermohaline circulation have warmed the poles? Paleoceanography 12 (2), 161–167, doi:10.1029/96PA03330.

Marotzke, J., Welander, P., Willebrand, J., 1988. Instability and multiple steady states in a meridional-plane model of the thermohaline circulation. Tellus, Series A 40 (2), 162–172.

Mohammad, R., Nilsson, J., 2004. The role of diapycnal mixing for the equlibrium response of thermohaline circulation. Ocean Dynamics 54 (1), 54–65, doi:10.1007/s10236-003-0065-4.

Munk, W. H., Wunsch, C., 1998. Abyssal recipes II: energetics of tidal and wind mixing. Deep-Sea Research, Part I 45 (12), 1977–2010, doi:10.1016/S0967-0637(98)00070-3.

Nilsson, J., Broström, G., Walin, G., 2003. The thermohaline circulation and vertical mixing: Does weaker density stratification give stronger overturning? Journal of Physical Oceanography 33 (12), 2781–2795, doi:10.1175/1520-0485(2003)033<2781:TTCAVM>2.0.CO;2.

Nilsson, J., Broström, G., Walin, G., 2004. On the spontaneous transition to asymmetric thermohaline circulation. Tellus, Series A 56 (1), 68–78, doi:10.1111/j.1600-0870.2004.00044.x.

Nilsson, J., Walin, G., 2001. Freshwater forcing as a booster of thermohaline circulation. Tellus, Series A 53 (5), 629–641, doi:10.1034/j.1600-0870.2001.00263.x.

Otterå, O. H., Drange, H., Bentsen, M., Kvamstø, N. G., D., J., 2003. The sensitivity of the present-day atlantic meridional overturning circulation to freshwater forcing. Geophysical Research Letters 30 (17), 1898, doi:10.1029/2003GL017578.

Park, Y.-G., Bryan, K., 2000. Comparison of thermally driven circulations from a depth-coordinate model and an isopycnal-layer model. Part I: Scaling-law sensitivity to vertical diffusivity. Journal of Physical Oceanography 30 (3), 590–605, doi:10.1175/1520-0485(2000)030<0590:COTDCF>2.0.CO;2.

Pierrehumbert, R. T., 2002. The hydrological cycle in deep-time climate problems. Nature 419, 191–198, doi:10.1038/nature01088.

Rahmstorf, S., 1996. On the freshwater forcing and transport of the Atlantic thermohaline circulation. Climate Dynamics 12, 799–811.

Rahmstorf, S., England, M. H., 1997. Influence of southern hemisphere winds on North Atlantic deep water flow. Journal of Physical Oceanography 27 (9), 2040–2054, doi:10.1175/1520-0485(1997)027<2040:IOSHWO>2.0.CO;2.

Rooth, C., 1982. Hydrology and ocean circulation. Progress In Oceanography 11 (2), 131–149, doi:10.1016/0079-6611(82)90006-4.

Scott, J. R., Marotzke, J., Stone, P. H., 1999. Interhemispheric thermohaline circulation in a coupled box model. Journal of Physical Oceanography 29 (3), 351–365, doi:10.1175/1520-0485(1999)029<0351:ITCIAC>2.0.CO;2.

Simmons, H. L., Jayne, S. R., St. Laurent, L. C., Weaver, A. J., 2004. Tidally driven mixing in a numerical model of the ocean general circulation. Ocean Modelling 6 (3–4), 245–263, doi:10.1016/S1463-5003(03)00011-8.

Stocker, T. F., Wright, D. G., Mysak, L. A., 1992. A zonally averaged, coupled ocean-atmosphere model for paleoclimate studies. Journal of Climate 5 (8), 773–797, doi:10.1175/1520-0442(1992)005<0773:AZACOA>2.0.CO;2.

Thual, O., McWilliams, J. C., 1992. The catastrophe structure of thermohaline convection in a two-dimensional fluid model and comparison with low-order box models. Geophysical and Astrophysical Fluid Dynamics 64 (1–4), 67–95.

Toggweiler, J. R., Samuels, B., 1995. Effect of Drake Passage on the global thermohaline circulation. Deep-Sea Research, Part I 42 (4), 477–500, doi:10.1016/0967-0637(95)00012-U.

Toole, J. M., McDougall, T. J., 2001. Mixing and stirring in the ocean interior. In: Siedler, G., Church, J., Gould, J. (Eds.), Ocean Circulation and Climate. Vol. 77. Academic Press, Inc., pp. 337–356.

Vellinga, M., 1996. Instability of two-dimensional thermohaline circulation. Journal of Physical Oceanography 26 (3), 305–319, doi:10.1175/1520-0485(1996)026<0305:IOTDTC>2.0.CO;2.

Walin, G., 1985. The thermohaline circulation and the control of ice ages. Paleogeography, Paleoclimatology, Paleoecology 50, 323–332.

Wang, X., Stone, P. H., Marotzke, J., 1999. Global thermohaline circulation. Part I: Sensitivity to atmospheric moisture transport. Journal of Climate 12 (1), 71–82, doi:10.1175/1520-0442(1999)012<0071:GTCPIS>2.0.CO;2.

Wang, Z., Mysak, L. A., 2000. A simple coupled atmosphere-ocean-sea ice-land surface model for climate and paleoclimate studies. Journal of Climate 13 (6), 1150–1172, doi:10.1175/1520-0442(2000)013<1150:ASCAOS>2.0.CO;2.

Welander, P., 1986. Thermohaline effects in the ocean circulation and related simple models. In: Willebrand, J., Anderson, D. L. T. (Eds.), Large-Scale Transport Processes in Oceans and Atmosphere. D. Reidel publishing company, pp. 163–200.

Wright, D. G., Stocker, T. F., 1991. A zonally averaged ocean model for the thermohaline circulation. Part I: Model development and flow dynamics. Journal of Physical Oceanography 21 (12), 1713–1724, doi:10.1175/1520-0485(1991)021<1713:AZAOMF>2.0.CO;2.

Wright, D. G., Stocker, T. F., Mercer, D., 1998. Closures used in zonally averaged ocean models. Journal of Physical Oceanography 28 (5), 791–804, doi:10.1175/1520-0485(1998)028<0791:CUIZAO>2.0.CO;2.

Wunsch, C., Ferrari, R., 2004. Vertical mixing, energy and the general circulation of the oceans. Annual Review of Fluid Mechanics 36, 281–314, doi:10.1146/annurev.fluid.36.050802.122121.

Paper III

An altimetric study of the Nordic-Sea region seasonal cycle

Rezwan Mohammad, Johan Nilsson and Peter Lundberg

Under review in Deep Sea Research Part I

Abstract

The present study utilizes satellite altimetric data providing Sea-Level Anomalies (SLAs from 1992 to 2004) to investigate depth-integrated flows in the Nordic Seas. Focus is on the seasonal cycle of the transports, which most evidently manifests itself in the winter-to-summer differences. These flow anomalies are separated into barotropic and baroclinic parts using a seasonal hydrographic climatology. The baroclinic part is generally weaker than the barotropic component, which primarily is forced by wind (and constrained by conservation of potential vorticity to essentially follow the isobaths). We examine two sections in the Nordic Seas, extending from a common point in the central Norwegian Sea to Svinøy (on the west coast of Norway) and the Faroe Islands, respectively. The total barotropic transport through the sections proved to be 12 and 10 Sv stronger during winter than in summer, respectively. By associating the flow with water masses on the basis of their salinity properties, it is found that a transport of 8 Sv is associated with the re-circulation in the interior of the Nordic Seas, the remainder being related to seasonal changes of the Atlantic inflow across the Greenland-Scotland ridge. Localized negative transport anomalies are, somewhat unexpectedly, found in both sections over a well-defined isobath range centered on 2500 m. This is possibly due to these isobaths extending into the Arctic basin, where the wind-forcing anomaly does not conform to that encountered regionally in the Nordic Seas.

1 Introduction

The northward transport of warm and saline Atlantic surface waters across the Greenland-Scotland Ridge into the Nordic Seas is of great importance, not only as a link in the global thermohaline circulation, but also for giving rise to the comparatively mild climate characterizing northwestern Europe. This process was first examined by Helland-Hansen and Nansen (1909), but was not investigated systematically until the International Council for the Exploration of the Seas (ICES) coordinated the first large-scale overflow survey in 1960 (Dietrich, 1967). The resulting data set was, among other things, used for the first mass and heat budget pertaining to the Greenland, Iceland and Norwegian Seas (Worthington, 1970).

These pioneering investigations were primarily based on standard hydrographic surveys conducted using water bottles and reversing thermometers, a classical technique presently superseded by electronic methods, viz. the modern CTD. During the last decades, however, satellite-altimetric techniques have also become operational, hereby providing direct information about the sea-surface topography and, by inference, the large-scale geostrophically balanced barotropic surface transport. A number of interesting studies based on this methodology have focused on the Atlantic inflow to the Nordic Seas. These investigations have, however, to a significant extent been devoted to processes of a comparatively local nature (see e.g. Hátún and McClimans, 2003), or on the oceanic-scale forcing of the inflow well south of the Greenland-Scotland ridge (Orvik and Skagseth, 2003).

The present study will deal with conditions in the entire Nordic-Sea region, including the Iceland-Scotland gap where a large part of the Atlantic inflow takes place. The investigation, focusing on the important seasonal cycle, will be undertaken primarily on the basis of altimetry representing a merger of data from six different satellite missions. A primary aim is to examine the response of the depth-integrated circulation to the seasonal variations of the wind- and buoyancy-induced forcing. In this respect, the present study is related to the work reported by Isachsen et al. (2003), who analyzed the time-dependent wind-driven circulation in the Nordic Seas and Arctic Ocean. The present work will attempt to separate the seasonal variability of the depth-integrated circulation into a baroclinic part, related to variations in the hydrography, and a barotropic component, related to the horizontal redistribution of mass. Wind forcing dominates the variability of the barotropic part, whereas the baroclinic part is influenced by surface buoyancy fluxes as well as by wind-induced changes of the

buoyancy-advection.

We note that the present study is closely related to the investigation reported by Mork and Skagseth (2005), who also focus on the seasonal cycle of the Nordic Seas. An important difference between the studies, however, is that these investigators employ harmonic analysis to extract the annual cycle, whereas the present study uses the summer-to-winter difference to describe the annual variation. Further, Mork and Skagseth (2005) apply a spatial smoothing to their data, whereas we work with the spatial resolution provided by the original data. As will be demonstrated, the two approaches highlight slightly different aspects of the seasonal cycle in the Nordic Seas, hereby providing complementary information on the dynamics.

2 Data-set description

Two data sets, pertaining to the sea-surface elevation and the hydrography of the Nordic Seas, constitute the basis for the present investigation. When considering the former type of record, it is essential to note that only sea-level deviations from an average state can be measured using satellite altimetry, this due to insufficient knowledge of the absolute geoid.

The Sea-Level Anomalies (SLAs) to be used in the forthcoming analyses were made available by the CLS Space Oceanography Division. The data were provided on a weekly basis in gridded form with a spatial resolution better than 0.34×0.22 degrees, interpolated and assembled from numerous overpasses made by different satellites. Although time series encompassing the entire period 1992 to 2004 were made use of, the present study will primarily deal with the contrast between seasonal climatological averages. This restriction is mainly due to our ambition to focus on the fundamental processes which to lowest order govern the seasonal cycle of the Nordic Seas. It is, furthermore, also consonant with the properties of the hydrographic data set, which is not available in time-series form, but only as seasonal climatologies. The largest variations between seasons prove to be from winter (defined as January to March) to summer (July to September), why we choose to study this difference.

The hydrographic information is primarily used to deal with the purely steric part of the SLAs, caused by the seasonally varying thermal expansion of the water column. The data set utilized was provided by the World Ocean Database 2001 in the form of a gridded seasonal climatology with a spatial resolution of 0.3×0.3 degrees and the temperature-salinity distribution given at standard levels throughout the entire water column. As will be seen, this hydrographic climatology is not only useful for correcting

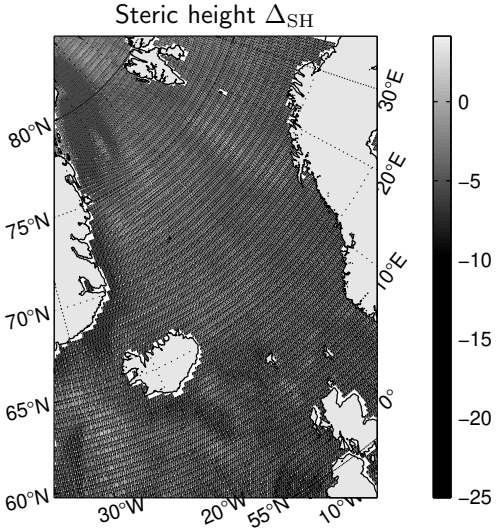

FIGURE 1: The winter-to-summer difference of the steric height in cm.

the SLA-based estimates of the barotropic velocity field, but also for direct determination of the baroclinic transports, cf. the appendix.

3 Analysis

A straightforward way of illustrating the seasonal fluctuations of the sea-surface height is to calculate the winter-to-summer difference of the SLA. (This approach has the further advantage of facilitating a direct comparison with recent result due to Jakobsen et al., 2003.) These sea-surface elevation differences are caused by two processes: *pro primo*, changes of the buoyancy in the water column, commonly referred to as the steric-height anomaly (primarily due to a varying heat content). *Pro secundo*, horizontal displacements of mass. This is to a large extent forced by seasonal changes of the large-scale atmospheric circulation.

3.1 The entire region

First we will consider the winter-to-summer steric-height difference Δ_{SH} estimated using the seasonal climatological hydrographic data. The results

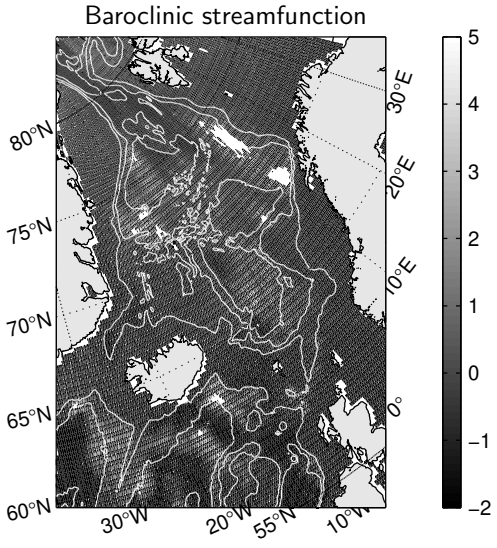

FIGURE 2: The winter-to-summer difference of the baroclinic streamfunction in Sv. The white lines represent equidistant isobaths with 1000 m spacing.

are shown in Fig. 1. Note that, just as in the case of the SLA, the steric height is given in terms of an anomaly, since the choice of reference is somewhat arbitrary. As expected, the steric height tends to be lower during winter than in summer, this due to a reduced oceanic buoyancy content. The results due to Mork and Skagseth (2005) show that in the bulk of the Nordic Seas, the steric height attains its maximum around September and that the annual cycle of this quantity is primarily forced by local air-sea heat exchange. An interesting exception is, however, that found in Fig. 1 along the Barents-Sea shelf slope north of the Lofoten peninsula in Norway. A closer inspection of the original data set reveals that this is caused by a winter-time maximum, presumably due to an enhanced advection of "warm" Atlantic water. This, in turn, is associated with the Norwegian Atlantic Slope Current being stronger during winter due to an increased wind forcing (Skagseth, 2004).

The changes of the stratification, which cause the steric-height anomalies, also give rise to anomalies in the potential energy of the water column. These affect the circulation, since the depth-integrated baroclinic flow is directly related to the horizontal gradients of the column-integrated potential

energy (cf. the appendix). Fig. 2 illustrates the winter-to-summer difference of the depth-integrated baroclinic flow, i.e. the difference in transport associated with the hydrographic changes. (Note that the results in Fig. 2 are represented in terms of a horizontal transport streamfunction, which is proportional to the winter-to-summer difference in column-integrated potential energy.) In the Nordic Seas, the anomalies of the depth-integrated baroclinic flow attain a magnitude of about 5 Sv. The results furthermore manifest a tendency towards regions dominated by positive values, implying local anomalies with an anticyclonic circulation. Fig. 2 reveals that the baroclinic flow anomalies generally are associated with cross-isobath transports. Off Lofoten, the hydrographic changes thus displace the baroclinic flow towards the central basin during winter. It should be emphasized, however, that the baroclinic anomalies of the bottom velocity are by definition aligned with the bathymetry (cf. the appendix) and hence do not induce vertical velocity anomalies.

We now subtract Δ_{SH} from the winter-to-summer difference of the "raw" SLA fields, resulting in a depth-independent seasonal pressure difference Δ_{SLA} referred to as barotropic, cf. the appendix. (Note that Δ_{SLA} is proportional to the bottom pressure anomaly.) This quantity is shown in Fig. 3, in connection with which it may be noted that the steric contribution is generally only a small part of the "raw" winter-to-summer SLA difference. From the figure it is seen that in the central basin of the Nordic Seas the sea level is lower during winter that in summer, whereas the opposite holds true adjacent to the coasts, the sea level here being higher during winter. From the graph it is also evident that Δ_{SLA} is strongly correlated with the bathymetry. We thus conclude that the seasonal change of the barotropic currents essentially takes place in a direction parallel with the isobaths, as indeed expected on dynamical grounds. We furthermore note that a particularly pronounced gradient of the Δ_{SLA} is encountered near the 1000-m isobath on the eastern side of the basin. This feature can be traced from the Atlantic proper all the way to the region north of Lofoten, consonant with previous results due to Skagseth et al. (2004).

It may also be noted that in an overall sense the sea level is depressed in the Nordic Seas during winter. Evidently this is linked to a large-scale redistribution of mass, why we next focus on the seasonal changes in transports which can be deduced from gradients of the Δ_{SLA} on the basis of assuming that the flow takes place in a geostrophic fashion. In particular, we are interested in examining the inflow of Atlantic water across the Iceland-Scotland Ridge and to possibly determine whether this transport can be separated from the re-circulation taking place within the south-

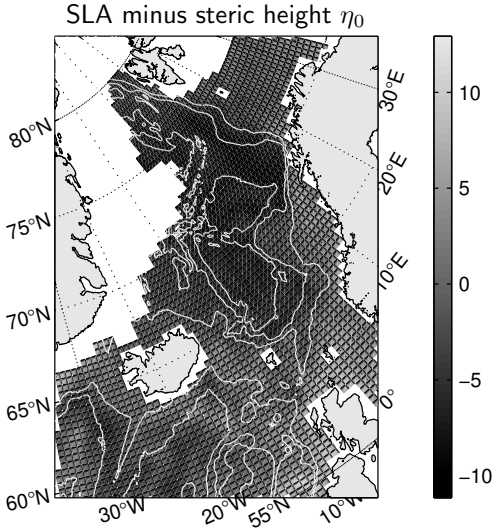

FIGURE 3: The winter-to-summer difference of SLA minus the steric height in cm. The white lines represent equidistant isobaths with 1000 m spacing. No SLA data are available in ice-covered areas.

eastern part of the Nordic Seas, cf. Isachsen et al. (2003). With this in mind, we choose to study two sections in greater detail, both located in the southern part of the Norwegian Sea (cf. Fig. 4). One of them to a large extent coincides with the classical Svinøy hydrographical section traversing a region of considerable oceanographic interest, cf. Mosby (1959). The other extends north-northeastwards from the Faroe Islands, and represents an oceanographically important transect (Hansen et al., 2003) which in what follows will be denoted the Faroe section.

3.2 The Svinøy section

We start by examining conditions along the Svinøy section, which for our purposes is taken to extend from the coast of Norway northwestwards into the Norwegian Sea to a depth of 3600 m. It is located athwart two important pathways of the Atlantic inflow to the Nordic Seas, viz. the Norwegian Atlantic Current and the Norwegian Atlantic Slope Current (Orvik et al., 2001; Orvik and Niiler, 2002).

After having retrieved Δ_{SH} and Δ_{SLA} along the section, we first examine

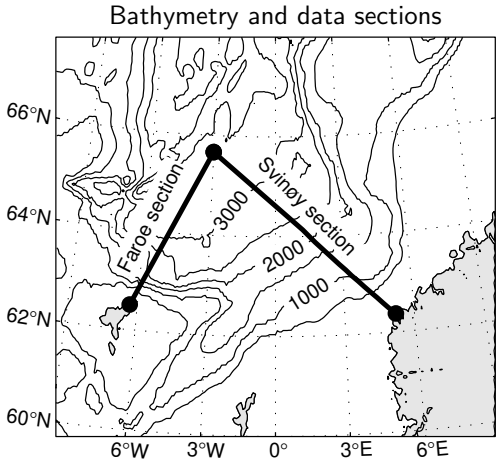

FIGURE 4: The bathymetry of the Nordic-Sea region with equidistant isobaths with 500 m spacing. The location of the Svinøy and Faroe sections are marked in the figure. The Faroes, Shetland and a small part of western Norway is gray shaded.

the winter-to-summer anomaly of the total surface-layer velocity normal to the Svinøy transect. This is calculated using the geostrophic assumption and is shown in Fig. 5, where northeastwards-directed flow anomalies are seen to dominate the section with the exception of one distinct zone. This region, where the surface-current anomaly is directed southwestwards, is found at bottom depths of around 2500 m approximately 300 km from the coast. It can, most likely, be identified with a similar feature visible in the analogously represented drifter data reported by Jakobsen et al. (2003).

We hereafter direct attention towards the depth-integrated transport anomalies which ultimately lead to a re-distribution of mass within the basin. They are determined by applying the analytical methods outlined in the appendix to Δ_{SLA} and Δ_{SH}. In Fig. 6 the winter-to-summer barotropic and baroclinic transport anomalies across the Svinøy section are shown in cumulative form, cf. the transport streamfunction defined in the appendix.

The accumulated barotropic transport anomaly is on the order of 10 Sv, a seasonal deviation exceeding Worthington's (1970) classical 7-Sv estimate of the yearly-averaged Iceland-to-Scotland surface-water inflow to the Norwegian Sea. The most likely reason for this unexpected state of affairs is that the altimetric transect also encompasses an as yet undefined fraction of

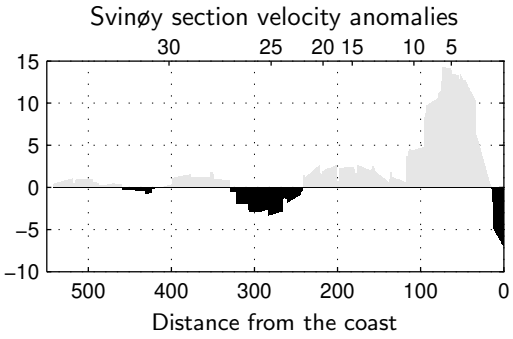

FIGURE 5: The winter-to-summer difference of the surface velocities at the Svinøy section in cm/s. Positive values are directed northeastwards. The distance from the coast is given in km. The upper scale shows the depth in hm.

the re-circulation characterizing the interior of the Nordic Seas (Jakobsen et al., 2003; Isachsen et al., 2003), a topic to be dealt with in greater detail in section 4 of the present study. A closer examination of the depth interval between 500 and 1000 m in Fig. 6 (displayed to better advantage in Fig. 10) reveals a northwards-directed winter-to-summer transport anomaly of the magnitude 5 Sv, in reasonable agreement with estimates based on direct current measurements reported by Orvik et al. (2001).

The accumulated baroclinic transport anomaly shown in Fig. 6 (derived from an interpolated hydrographic climatology) can be compared with the seasonally averaged transports obtained by applying the dynamic method (Fomin, 1964) to 1955–1996 synoptic hydrographic data from the Svinøy section proper (Mork and Blindheim, 2000). The two sets of results are found to be in broad agreement, indicating that the hydrographic climatology (WOD 2001) is adequate for correcting the "raw" SLA results with regard to steric-height effects. In this context it also deserves mention that the presently calculated annually averaged baroclinic flow across the Svinøy section agrees reasonably well with classical results from the Sognefjord section (Helland-Hansen, 1934), even though the locations of the two transects differ somewhat.

3.3 The Faroe section

As we discuss the results from the transect extending 500 km north-northeastwards from the Faroe Islands, it must be kept in mind that this setting differs considerably from that previously encountered along the Svinøy sec-

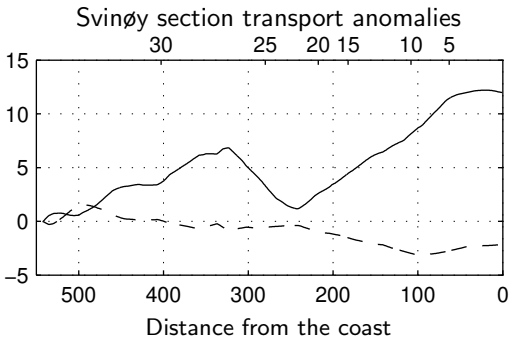

FIGURE 6: The winter-to-summer difference of the barotropic (solid line) and baroclinic (dashed line) parts of the cumulative transport anomalies through the Svinøy section in Sv. The distance from the coast is given in km. The upper scale shows the depth in hm.

tion. The most important dissimilarity is that the Faroe section traverses the Iceland-Faroe front (Hansen and Meincke, 1979). The surface location of this permanent feature of the southern Norwegian Sea is generally identified with that of the 35 isohaline, whereas in the vertical the front terminates more-or-less on the crest of the Iceland Faroes ridge. Fig. 7 shows the winter and summer location of the 35 isohaline in the Faroe section, illustrating that Atlantic water accumulates adjacent to the Faroe Islands during winter. An intrusion of warm and high-saline water of Atlantic origin thus characterizes the southern reaches of the Norwegian Sea, although it must be noted that the precise location of the front is subject to considerable variations (Hopkins, 1991).

As regards the Faroe section (cf. Fig. 4) an interesting consequence is that the Iceland-Faroe branch of the Atlantic inflow is orientated almost due eastwards immediately north of the Faroes. Particularly during winter this climatologically important transport manifests itself hydrographically as a distinct wedge of Atlantic water overlying the deeper water masses of mainly northerly origin (Hansen et al., 2003), and is also, as will be seen, clearly discernible in the altimetric results.

On the basis of Δ_{SH}- and Δ_{SLA}-data retrieved along the section, we start by looking at the winter-to-summer anomaly of the total surface-layer velocity normal to the Faroe transect (which terminates at a depth of 3400 m). Fig. 8 thus shows the geostrophically determined total surface-layer velocity anomaly. Here easterly-directed velocity anomalies dominate except for a zone at around 200 km from the Faroe coast, where the velocity

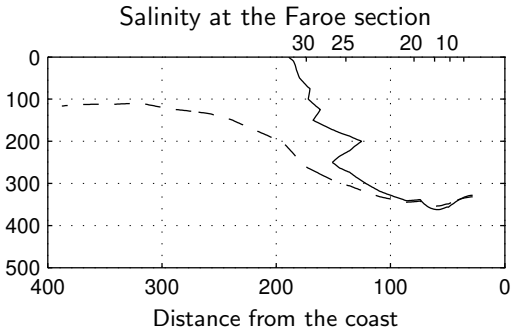

FIGURE 7: The location of the 35 isohaline during winter (solid line) and summer (dashed lines) at the Faroe section. The distance from the coast is given in km. The upper scale shows the depth in hm.

anomalies have the opposite direction. This feature may be related to the abovementioned presence of the Iceland-Faroe front, which due to stronger forcing is more pronounced during winter than in summer. However, as to be further discussed in next section, it is also possible that the basin-wide forcing along the 2500-m isobath plays a role for maintaining this "reverse-flow" anomaly. (In this context it deserves to be underlined that the negative velocity anomaly is a barotropic phenomenon since the seasonal change in stratification tends to produce positive velocity anomalies in this zone.) A direct comparison between the overall results summarized in Fig. 8 and the analogously represented drifter data assembled by Jakobsen et al. (2003) proved somewhat inconclusive; it must, however, be noted that no overtly contradictory features were discernible in the two data sets.

Using the techniques described in the appendix we now examine the depth-integrated winter-to-summer transport anomalies, cf. Fig. 9. The cumulative barotropic transport across the Faroe transect is seen to be on the order of 10 Sv, viz. roughly of the same magnitude as in the Svinøy-section case. Particular note should be taken that immediately adjacent to the Faroe coast a direct comparison with current-meter results is feasible, since an ADCP-array has been operational here since the mid-1990s (Hansen et al., 2003). Fig. 9 thus shows that the integrated barotropic seasonal transport anomaly over the depth interval terminating at around 1500 m is $3 \sim 4$ Sv. This is in rough agreement with results due to Hansen et al. (2003), viz. that the seasonal transport difference was around 2 Sv, when account is taken of the fact that the current measurements reported by these authors were focused on the upper 600 m of the water column.

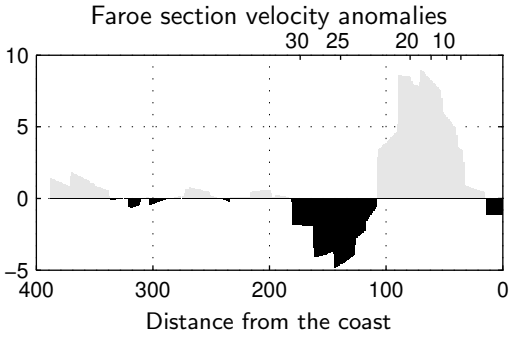

FIGURE 8: The winter-to-summer difference of the surface velocities at the Faroe section in cm/s. Positive values are directed eastwards. The distance from the coast is given in km. The upper scale shows the depth in hm.

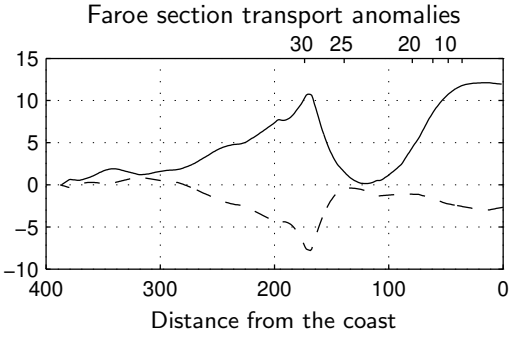

FIGURE 9: The winter-to-summer difference of the barotropic (solid line) and baroclinic (dashed line) parts of the cumulative transport anomalies through the Faroe section in Sv. The distance from the coast is given in km. The upper scale shows the depth in hm.

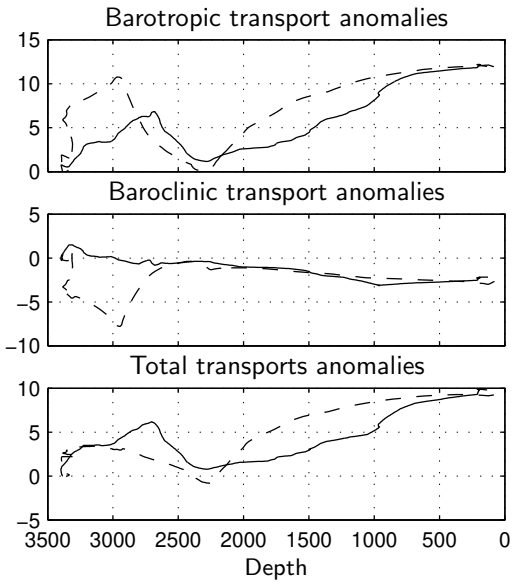

FIGURE 10: The winter-to-summer difference of the barotropic part of the cumulative transport through the Svinøy (solid) and Faroe (dashed) sections in Sv as functions of the bottom depth, given in m.

It can also be remarked that the cumulative barotropic transport anomaly shows a local maximum at 150 $\sim$ 200 km from the Faroe coast, approximately coinciding with the location of the Iceland-Faroe front.

As we direct attention to the accumulated baroclinic transport anomaly in Fig. 9, it may be noted that also these results appear to be affected by the Iceland-Faroe front, cf. the "dip" at 150 $\sim$ 200 km from the coast. This minimum reflects the seasonal variation of the front, cf. Fig. 7. Furthermore, we note that the seasonal changes in baroclinic transport are more pronounced in the Faroe section than in the Svinøy section, where the winter-to-summer difference in the hydrography is less pronounced.

4 Discussion

In order to facilitate an overview of the circulation in the southern part of the Norwegian Sea, we commence by a direct comparison between the results from the Svinøy and Faroe sections. Since the requirement of con-

served potential vorticity tends to restrict oceanic flows to a specific isobath, the two sets of transport-anomaly results have in Fig. 10 been graphed versus local bottom depth. On the basis of this representation in terms of the bathymetry, the distributions of the transport anomalies over the two sections are qualitatively similar. Note, however, that the baroclinic results differ for depths above 2500 m due to the seasonal variations of the Iceland-Faroe front (a feature which does not have any counterpart on the Svinøy section where the seasonal changes of the hydrography are insignificant, cf. the middle panel of Fig. 10). This baroclinic deviation characterizing the outer parts of the Faroe section serves to compensate for the analogous barotropic local maximum, yielding approximately similar total-transport anomalies for the two sections. However, the resolution and accuracy of the present data are presumably not high enough to capture the full details of how the transport anomaly along an isobath varies between the Faroe and Svinøy sections. As an example it can be noted that for the 1500-m isobath, Fig. 10 reveals a difference in barotropic transport anomaly between the two sections of 4 Sv, indicating a cross-isobath transport anomaly of the same magnitude. We note that along an isobath it would require a mere 2 cm surface-height difference to generate a cross-isobath transport anomaly on this order. A straightforward estimate, however, shows that a cross-isobath flow of 4 Sv would induce a vertical velocity anomaly on the order of 10^{-4} m/s. This is about 100 times stronger than the mean wind-induced Ekman pumping in the region (Nøst and Isachsen, 2003). An error of one to two cm is to be expected over the shelf slope, where the dynamics are inadequately resolved by the gridded SLA data employed for the present study. Thus, the differences in barotropic transport anomaly between the two sections for the same isobaths may be attributable to an error of the estimated along-isobath SLA difference.

In the region with depths exceeding around 3000 m the transport anomalies are, according to Fig. 10, positive. This result is expected, since the circulation in the central Norwegian Sea is strongly controlled by topography and mainly forced by the wind. The deep isobaths here form closed contours around the Norwegian Sea and Lofoten basin and the prevailing cyclonic wind forcing is stronger during winter than in summer (Isachsen et al., 2003).

Fig. 10 shows that in the zone with bottom depths between 2300 and 3000 m there are significant and conspicuous negative transport anomalies, corresponding to the previously discussed negative velocity anomalies (cf. Fig. 5 and 8). It should be noted that these comparatively well-localized negative anomalies are not identified in the studies due to Isachsen et al.

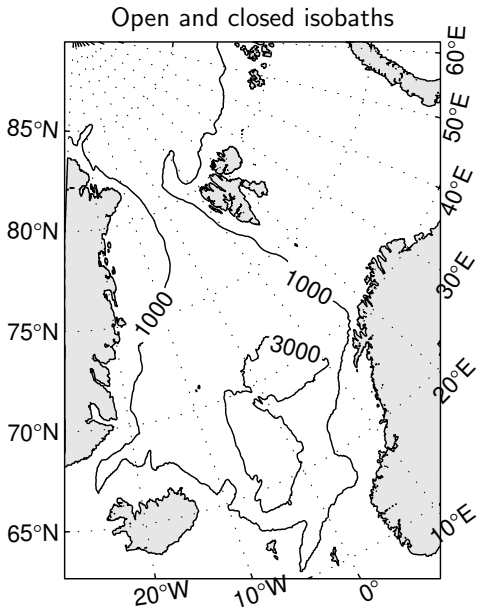

FIGURE 11: Open 1000-m and closed 3000-m isobath contours in the Nordic Seas. Irrelevant isobath contours are not included in the figure.

(2003) and Mork and Skagseth (2005). (The former study only took into account the leading EOF of the SLA, which is dominated by the large spatial scales. The latter investigation applied spatial smoothing the the SLA field, thereby suppressing small-scale features.) The negative transport anomalies are of the same order of magnitude as the positive anomalies for bottom depths greater than around 3000 m, why they to a large extent cancel one another. Hence, the net volume transport anomalies for depths greater than 2300 m are almost zero. There is a distinct possibility that this feature can be explained by the geographic distribution of the isobaths over this intermediate bottom-depth range. In contrast to the deeper isobaths, which form closed contours within the Norwegian Sea and Lofoten Basin, the closed contours associated with the more shallow isobaths extend well into the Arctic Basin, cf. Fig. 11. The flow, which is topographically guided, is forced by the wind stress acting around the entire closed depth contour under consideration (Nøst and Isachsen, 2003; Isachsen et al., 2003). Thus the flow is governed by the global characteristics of the wind, rather than those of a purely local nature. Accordingly, the negative transport anomalies may reflect that over the depth contours that girdle the Arctic and Nordic Seas, the integrated surface stress is weaker during winter than in summer. It must, however, at all time be kept in mind that the transports discussed here only represent deviations from a mean flow in an over-all north-eastwards direction (Nøst and Isachsen, 2003; Jakobsen et al., 2003).

Where the bottom depths are less than 2300 m the transport anomaly is positive. This zone may conveniently be divided into two subregions: One deeper than the $400 \sim 500$ m threshold constituted by the Greenland-Scotland Ridge and one where the isobaths communicate directly with the Atlantic proper south of the ridge. To pursue the analysis along lines consonant with these characteristics, it proves convenient to examine the cumulative barotropic transport anomaly distributions $\Delta M(S)$ across the sections as functions of the salinity (cf. the Appendix). (Accordingly $\Delta M(S = 35)$ represents the total barotropic transport of waters with $S \leq 35$ through the transect, i.e. 8 Sv). Based on the previously employed seasonal hydrographic climatologies, the results are shown in Fig. 12 encompassing the pertinent salinity range 34.85 to 35.25. Two features of the flow anomalies $\Delta M(S)$ should be particularly noted. To begin with, the functions $\Delta M(S)$ are nearly identical for the two sections, in contrast to the barotropic transport anomalies graphed versus the depth in Fig. 10. The underlying reason is that the isohalines are nearly horizontal, implying that the transport anomaly over a certain salinity range is made up of constituents from locations that are distributed laterally over the sections. This horizontal

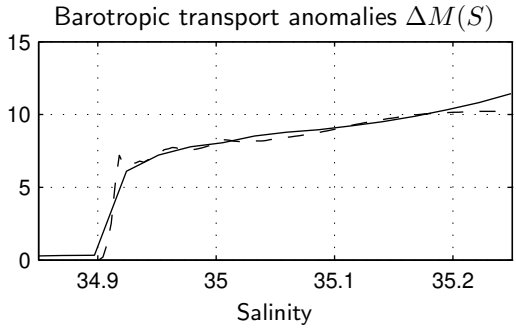

FIGURE 12: The winter-to-summer difference of the barotropic part of the cumulative transport distributions through the Svinøy (solid) and Faroe (dashed) sections in Sv as functions of salinity.

integration reduces the sensitivity to SLA errors. Second, the conspicuous negative flow anomalies in Fig. 10 are absent in Fig. 12. It is the horizontal integration in the construction of the function $\Delta M(S)$ that yields a net positive transport anomaly for each salinity, although negative anomalies are encountered locally over both sections.

The integrated volume transport anomaly for low-saline water ($S < 34.91$) is virtually zero, the minor contribution arising from the comparatively fresh Norwegian Coastal Current on the Svinøy section being negligible. Between the salinities 34.91 and 34.92 there is, however, an abrupt change of almost 7 Sv in the cumulative transport anomaly. This corresponds to the transport of Norwegian Sea Deep Water, which constitutes the bulk of the interior basin water due to its great depth and horizontal extent (Mosby, 1959). The waters originating in the Nordic Seas are characterized by salinities below 35 (Swift, 1986). The cumulative volume transport anomaly of these water masses is around 8 Sv, which evidently is associated with the re-circulation in the interior of the Nordic Sea basin and furthermore is in broad agreement with quantitative numerical-model results as well as empirical evidence reported by Isachsen et al. (2003).

The cumulative transport anomaly for more saline waters ($S > 35$) is undoubtedly related to variations of the Atlantic inflow. It is, however, important to emphasize that Fig. 12 does not represent the total inflow variation since, *pro primo*, baroclinic flow is not included and, *pro secundo*, interactions between the mean flow and the seasonal variations of the hydrography are not taken into account, cf. the appendix. To illuminate the latter effect, it is instructive to consider Fig. 7: Suppose that there is a

uniform positive mean velocity over the entire section. In this situation, it is evident that the transport of water having a salinity higher than 35 would be diminished in winter, when area of occupied by the wedge of high-saline water is reduced. Since this effect is not accounted for in the result shown in Fig. 12, it will act to cancel out the 2-Sv seasonal cycle of high-saline waters ($S > 35$). The seasonality of the total barotropic transport of these water masses will be more consonant with previous estimates (Hansen et al., 2003) of the Atlantic inflow based on ADCP measurements, which do not show any seasonal cycle.

Fig. 12 shows that across the Svinøy section the barotropic transport of high-saline waters ($S > 35$) is somewhat more than 3 Sv higher during winter than in summer. (Note that this result does not include the contribution from the mean flow, since the altimetric data set only provides anomalies.) This is in the same order of magnitude as transport estimates based on measurements (Orvik et al., 2001).

In this context it may also be worth underlining that the salinity is not only a useful parameter when, as here, analyzing more-or-less local features of the flow. From a larger-scale perspective provided by the global thermohaline circulation, the salinity properties of the Atlantic inflow to the Nordic Seas are crucial for determining whether winter-time convection in the Greenland Sea will take place.

5 Conclusions

On the basis of hydrographic and altimetric data, we have studied the winter-to-summer flow difference in the Nordic Seas, with emphasis on the Faroe and Svinøy sections. We find that the volume transports across the two sections are some 10 Sv stronger in winter than in summer. The winter-time enhancement of the flow is primarily of a barotropic character, presumably a response to the seasonal cycle of the wind forcing. However, at the Faroe section hydrographic changes yield significant baroclinic transport anomalies, tending to counteract those of a barotropic character. The present analysis furthermore reveals that at the Svinøy section the seasonal cycle of the baroclinic transport is relatively weak. Off Lofoten the baroclinic transport has a much more pronounced seasonal variation.

To summarize, the investigation presented here shows that the winter-to-summer changes of the transport within the Nordic Seas previously derived from current-meter records is reproducible with reasonable accuracy from altimetric data and climatological hydrography. Due to an unknown mean flow and inadequately resolved near-shore velocity anomalies, the

present study is, however, not capable of directly estimating the seasonal transport variation of Atlantic water along across the Faroe section.

Along the closed isobaths in the interior of the Nordic Seas a barotropic re-circulation is encountered, which is around 8 Sv stronger in winter than during summer. However, both on the Svinøy and the Faroe sections there is a range of bottom depths which are characterized by negative barotropic transport anomalies. The present study has not focused on identifying the physical mechanisms giving rise to these negative anomalies. A plausible explanation may, however, be that the isobaths in this range of bottom depths (between 2300 and 3000 m) extend well into the Arctic basin, where the wind-forcing characteristics differ from those in the Nordic Seas. (Note that due to permanent sea ice, parts of the Arctic basin are shielded from the direct effects of the wind forcing.) These issues will be addressed in a forthcoming study, where also the correlation between the transports and the wind forcing will be analyzed with respect to its time-scale dependence.

Acknowledgments

The work herein reported was undertaken on the basis of a grant from the Swedish National Space Board. The altimeter products were made available by the CLS Space Oceanography Division as part of the Environment and Climate EU ENACT project (EVK2-CT2001-00117) and with support from CNES. We also thank Thomas Rossby for interesting and rewarding discussions.

Appendix

We will here derive some relations pertaining to stratified flows in hydrostatic and geostrophic balance. The hydrostatic equation is given by

$$\frac{\partial p}{\partial z} = -g\rho_r(1-q), \tag{1}$$

where $\rho_r = \rho(34.9, 0, P)$ is a reference density characterizing the deep water and $q = q(x, y, z, t)$ is a measure of the density anomaly. We integrate the hydrostatic equation upwards from the bottom, which yields

$$p(x, y, z) = g\rho_r \int_{-H}^{z} q \, \mathrm{d}z + p_0(x, y) - g\rho_r z. \tag{2}$$

Here $H(x, y)$ is the depth and p_0 is the "barotropic" pressure anomaly. Note that $p_0 = p_b - g\rho_r H$, where p_b is the bottom pressure; see the discussion given in Nilsson et al. (2005).

The (linearized perturbation) surface pressure is related to the sea-surface height (say η) according to $p(z=0) = g\rho_r\eta$. Thus, eq. (2) yields the relation

$$\eta = \int_{-H}^{0} q \, \mathrm{d}z + p_0/(g\rho_r). \tag{3}$$

This motivates us to introduce

$$\eta_q = \int_{-H}^{0} q \, \mathrm{d}z; \; \eta_0 = p_0/(g\rho_r), \tag{4}$$

where η_q will be denoted the steric-height anomaly and η_0 is the contribution to sea-surface height associated with the barotropic pressure anomaly. In the main body of the present study focus is on $\eta_q(\text{winter}) - \eta_q(\text{summer}) = \Delta_{\text{SH}}$ and $\eta_0(\text{winter}) - \eta_0(\text{summer}) = \Delta_{\text{SLA}}$.

We assume that the flow obeys the geostrophic balance

$$f\mathbf{k} \times \mathbf{u} = -{\rho_r}^{-1} \nabla_h p, \tag{5}$$

where $\mathbf{u} = (u, v)$ is the horizontal velocity component, f the Coriolis parameter, $\mathbf{k}$ a vertical unit vector, and ∇_h the horizontal gradient operator. By using this relation and eq. (2), we obtain

$$\mathbf{u} = \frac{g}{f}\mathbf{k} \times \nabla_h \int_{-H}^{z} q \, \mathrm{d}z + \frac{1}{f\rho_r}\, \mathbf{k} \times \nabla p_0. \tag{6}$$

The r.h.s. of this expression is constituted by a baroclinic and barotropic velocity component, to be denoted $\mathbf{u}_q$ and $\mathbf{u}_0$, respectively. Straightforward calculations show that the depth-integrated flow associated with $\mathbf{u}_q$ is described by the baroclinic-transport streamfunction

$$\psi_q = -\frac{g}{f} \int_{-H}^{0} z \cdot q \, \mathrm{d}z. \tag{7}$$

(Note that $f \cdot \psi_q$ equals the column-integrated potential energy.)

For a specified transect (e.g. the Faroe or the Svinøy section), we define the following volume transport function (cf. Walin, 1982)

$$M(S,t) = \iint_{A(S)} v(x,y,z,t) \, \mathrm{d}A,$$

where v is the velocity normal to the section and $A(S)$ is the area in the section where the salinity is less than S. Thus, $M(S)$ represents the volume

transport through the section of water having a salinity less than S. We are concerned with the winter-to-summer difference of $M(S)$, i.e. $\Delta M(S) = M_w(S) - M_s(S)$ where the subscripts w and s refer to the winter and the summer season, respectively.

$$\Delta M(S) = \iint_{A_w(S)} v_w(x, y, z)\,\mathrm{d}A - \iint_{A_s(S)} v_s(x, y, z)\,\mathrm{d}A. \tag{8}$$

We introduce $\overline{v} = (v_w + v_s)/2$ and $\Delta v = (v_w - v_s)/2$, which allows us to write

$$\Delta M(S) = \iint_{A_w(S)-A_s(S)} \overline{v}\,\mathrm{d}A + \iint_{A_w(S)} \Delta v\,\mathrm{d}A + \iint_{A_s(S)} \Delta v\,\mathrm{d}A. \tag{9}$$

As we do not have knowledge of the mean flow $\overline{v}$, we have in the main body of the present study only calculated the contributions to $\Delta M(S)$ from the last two r.h.s.-terms of eq. (9).

Bibliography

Dietrich, G., 1967. The international "overflow" expedition (ICES) of the Iceland-Faroe ridge, May–June 1960. Rapports et Procès-Verbaux des Réunions Conseil International pour l'Exploration de la Mer 157, 268–274.

Fomin, L. M., 1964. The Dynamic Method in Oceanography. Elsevier Publ. Co.

Hansen, B., Meincke, J., 1979. Eddies and meanders in the Iceland-Faeroe Ridge area. Deep-Sea Research 26, 1067–1082.

Hansen, B., Østerhus, S., Hátún, H., Kristiansen, R., Larsen, K. M. H., 2003. The Iceland-Faroe inflow of Atlantic water to the Nordic Seas. Progress in Oceanography 59 (4), 443–474, doi:10.1016/j.pocean.2003.10.003.

Helland-Hansen, B., 1934. The Sognefjord Section. Oceanographic observations in the northernmost part of the North Sea and the southern part of the Norwegian Sea. In: James Johnstone Memorial Volume. University Press of Liverpool, UK, pp. 257–274.

Helland-Hansen, B., Nansen, F., 1909. The Norwegian Sea, its physical oceanography. based on the Norwegian researches 1900–1904. Report on Norwegian fishery and marine investigations 2 (2), 1–359.

Hopkins, T. S., 1991. The GIN sea — a synthesis of its physical oceanography and literature review 1972–1985. Earth Science Reviews 30, 175–318.

Hátún, H., McClimans, T. A., 2003. Monitoring the Faroe Current using altimetry and coastal sea-level data. Continental Shelf Research 23 (9), 859–868, doi:10.1016/S0278-4343(03)00059-1.

Isachsen, P. E., LaCasce, J. H., Mauritzen, C., Häkkinen, S., 2003. Wind-driven variability of the large-scale recirculating flow in the Nordic Seas and Arctic Ocean. Journal of Physical Oceanography 33 (12), 2534–2550, doi:10.1175/1520-0485(2003)033<2534:WVOTLR>2.0.CO;2.

Jakobsen, P. K., Ribergaard, M. H., Quadfasel, D., Schmith, T., Hughes, C. W., 2003. Near-surface circulation in the northern North Atlantic as inferred from Lagrangian drifters: Variability from the mesoscale to interannual. Journal of Geophysical Research 108 (C8), 3251, doi:10.1029/2002JC001554.

Mork, K., Skagseth, Ø., 2005. Annual sea surface height variability in the nordic seas. In: Climate Variability in the Nordic Seas. Geophysical Monograph Series, AGU. American Geophysical Union, in press.

Mork, K. A., Blindheim, J., 2000. Variations in the Atlantic inflow to the Nordic Seas, 1955-1996. Deep Sea Research Part I 47 (6), 1035–1057, doi:10.1016/S0967-0637(99)00091-6.

Mosby, H., 1959. Deep water in the Norwegian Sea. Geophysica Norvegica 21 (3), 1–62.

Nilsson, J., Broström, G., Walin, G., 2005. Steady f-plane circulation arising from a prescribed buoyancy distribution in basins with sloping boundaries; or the role of bottom friction for creating a thermohaline circulation, submitted to Journal of Marine Research.

Nøst, O., Isachsen, P., 2003. The large-scale time-mean ocean circulation in the Nordic Seas and Arctic Ocean estimated from simplified dynamics. Journal of Marine Research 61 (2), 175–210, doi:10.1357/002224003322005069.

Orvik, K. A., Niiler, P., 2002. Major pathways of Atlantic water in the northern North Atlantic and Nordic Seas toward Arctic. Geophysical Research Letters 29 (19), 1896, doi:10.1029/2002GL015002.

Orvik, K. A., Skagseth, Ø., 2003. The impact of the wind stress curl in the North Atlantic on the Atlantic inflow to the Norwegian Sea toward the Arctic. Geophysical Research Letters 30 (17), 1884, doi:10.1029/2003GL017932.

Orvik, K. A., Skagseth, Ø., Mork, M., 2001. Atlantic inflow to the Nordic Seas: current structure and volume fluxes from moored current meters, VM-ADCP and SeaSoar-CTD observations, 1995-1999. Deep Sea Research Part I 48 (4), 937–957, doi:10.1016/S0967-0637(00)00038-8.

Skagseth, Ø., 2004. Monthly to annual variability of the Norwegian Atlantic Slope Current: Connection between the northern North Atlantic and the Norwegian Sea. Deep-Sea Research Part I 51 (3), 349–366, doi:10.1016/j.dsr.2003.10.014.

Skagseth, Ø., Orvik, K. A., Furevik, T., 2004. Coherent variability of the Norwegian Atlantic Slope Current derived from TOPEX/ERS altimeter data. Geophysical Research Letters 31, doi:10.1029/2004GL020057.

Swift, J. H., 1986. The Arctic Waters. In: Hurdle, B. G. (Ed.), The Nordic Seas. Springer-Verlag, pp. 129–153.

Walin, G., 1982. On the relation between sea surface heat flow and thermal circulation in the ocean. Tellus 34 (2), 187–195.

Worthington, L. V., 1970. The Norwegian Sea as a Mediterranean basin. Deep-Sea Research 17, 77–84.

Paper IV

Inter-annual variability of the along-isobath flow in the Norwegian Sea

Rezwan Mohammad

Stockholm University, Department of Meteorology,
DM-report 94, 2005

Abstract

The present investigation is focused on barotropic wind-driven circulation along closed isobaths on a f-plane. A relationship has been derived between the surface wind stress and the along-isobath flow, the latter which can also be estimated using satellite-altimetric methods. The re-circulation gyre in the central Norwegian Sea proved amenable to this mode of analysis, since the isobath-averaged flow estimates based on sea-level anomalies and wind data were compared and found to be essentially the same, indicating that this re-circulation predominantly is locally forced. Additionally the along-isobath flow associated with the Norwegian Atlantic Slope Current (NwASC), which originates in the Atlantic proper, was also estimated using satellite-altimetric data. These NwASC results were compared with the corresponding closed-isobath circulation in the central Norwegian Sea, whereby it was found that there were periods when the variabilities of the two flows appeared to be decoupled. It is argued that this may be caused by the wind forcing of the NwASC being exerted along the full stretch of the 500-m isobath originating in the Atlantic proper, whereas the central Norwegian Sea re-circulation gyre is more-or-less locally forced. This inference is to some extent justified on the basis of a comparison between the NwASC results, the North Atlantic Oscillation (NAO) index, and the wind stress integrated along the 500-m isobath from 50°N to 67°N.

1 Introduction

The present study is focused on the low-frequency variability of the circulation in the Nordic Seas. Here the term low-frequency is used to denote time-scales ranging from a few months up to several years. The primary concern of the investigation is with the Nordic-Seas variability associated with changes of the large-scale wind-stress forcing.

Already Helland-Hansen and Nansen (1909) recognized that the time-mean circulation in the Nordic Seas is strongly guided by the basin topography. This observed tendency of the near-surface flow to follow the isobaths throughout the Nordic Seas and the Arctic Ocean has recently been examined theoretically by Nøst and Isachsen (2003). For sufficiently low frequencies, also the time-dependent component of the flow tends to be aligned with the depth contours (Isachsen et al., 2003; Mohammad et al., 2005). When considering the response of the flow to low-frequency variations of the wind stress acting on the Nordic Seas, it is conceptually advantageous to distinguish between regions having closed isobaths[1] and those where the isobaths extend into the Arctic basin and/or over the Greenland-Scotland Ridge into the North Atlantic proper. In more-or-less limited regions with closed depth contours, there is a relatively straightforward relationship between the low-frequency flow and the wind stress. As has been demonstrated by Isachsen et al. (2003); Nøst and Isachsen (2003) as well as Nilsson et al. (2005), to lowest order of approximation the flow follows the isobaths and its strength is controlled by the wind stress integrated around the closed isobaths. On closed isobaths, the low-frequency flow is thus related to the wind forcing in a non-local fashion. However, the area where the wind forcing affects the flow is limited and well defined.

The *nexus* between the flow along isobaths extending into the Atlantic and the wind forcing appears to be more complex. A primary reason is that the flow along such isobaths is affected by the wind forcing over a much larger and less well-defined region. The study due to Orvik and Skagseth (2003a) suggests that the flow in the Norwegian Atlantic Slope Current (NwASC) across the Svinøy section may be significantly correlated with the wind forcing that acted on the North Atlantic some 15 months earlier. Specifically, these authors identified a connection between the strength of the NwASC and the curl of the wind stress integrated across the Atlantic Basin at 55°N.

The discussion above suggests that the NwASC (found on isobaths com-

[1] More generally closed H/f contours, where H is the depth and f the Coriolis parameter.

municating with the Atlantic) and the re-circulating gyres in the Nordic Seas (encountered in regions of closed isobaths) are forced from different geographical regions and by possibly different mechanisms. It should be pointed out that "closed" and "open" isobaths converge in a narrow zone along the Norwegian coast. In this region it is conceivable that the flow along deeper isobaths to some extent evolves independently from the flow associated with the more shoreward "open" isobaths. One question to be pursued in this study is thus to what degree the low-frequency variabilities of the flow associated with the closed gyres and along the open isobaths in the Nordic Seas are decoupled.

In next section the theoretical background to the considerations above will be outlined. Hereafter the relationship between the large-scale wind forcing and the flow on the isobaths that close themselves around the Norwegian Sea and the Lofoten Basin will be analyzed on the basis of satellite-altimetric data and observed wind stress. A detailed analysis of conditions along the Svinøy section extending north-westwards from the Norwegian coast is also carried out, whereafter the study is concluded by an overview and a discussion.

2 Theoretical background

In what follows, use will be made of some ideas originally presented by Walin (1972), who demonstrated that on closed isobaths, the low-frequency wind forcing primarily generates a barotropic flow along the depth contours. Recently, these results have been generalized and applied in studies by Isachsen et al. (2003), Nøst and Isachsen (2003) as well as Nilsson et al. (2005). An outline of the mathematical derivation is given in an appendix to the present study. Here, the starting point of the physical considerations is volume continuity for a region (say A) encircled by a closed curve C, on which H/f (i.e. the depth divided by the Coriolis parameter) is constant. It is further assumed that the flow is in hydrostatic balance and governed by linear dynamics. Under these assumptions, the volume budget of A is given by (see the appendix)

$$\frac{\partial}{\partial t}\iint_A \eta \,\mathrm{d}A = \frac{\partial}{\partial t}\oint_C \frac{\mathbf{U}}{f}\cdot \mathrm{d}\mathbf{s} + \oint_C \frac{\nabla Q}{f}\cdot \mathrm{d}\mathbf{s} - \frac{1}{\rho_0}\oint_C (\tau_\mathrm{w}/f - \tau_\mathrm{b}/f)\cdot \mathrm{d}\mathbf{s}. \quad (1)$$

Here η is the free surface, $\mathbf{U}$ the vertically-integrated flow, τ_w and τ_b the surface and the bottom stress, respectively, $\mathrm{d}\mathbf{s}$ the length element along C,

and Q the potential energy anomaly, the latter defined as

$$Q(x,y,t) = -g \int_{-H}^{0} zq \, \mathrm{d}z, \tag{2}$$

where g is the acceleration of gravity and q the buoyancy anomaly. Eq. (1) shows that the volume inside the curve C can be changed by (i) acceleration of the depth-integrated flow around the curve, (ii) baroclinic north–south flow[2], (iii) Ekman boundary-layer transports across C. In view of the forthcoming analysis of conditions in the Nordic Seas, eq. (1) is now simplified by making the following assumptions:

1. The variation of f is neglected. This is expected to be a reasonable approximation as the present focus is on an area of limited geographical extent, where furthermore the variations of H dominate the H/f geometry.

2. It is assumed that
$$\frac{\partial}{\partial t} \iint_A \eta \, \mathrm{d}A \approx 0.$$
The underlying motivation is that when the barotropic Rossby radius is significantly larger than the length-scale characterizing the flow, the rate of change of the depth-integrated circulation generally dominates over the rate of change of the volume (Gill, 1982). In the present case, this assumption was corroborated by an analysis based on the sea-surface height data retrieved from satellite altimetry, showing that the rate of change of circulation is typically two orders of magnitude greater the rate of change of volume.

3. The variability of the depth-integrated flow is assumed to have a barotropic character, i.e. the flow is taken to be depth-independent. Walin (1972) showed that the flow response to low-frequency wind forcing should be barotropic outside the costal zone. A *caveat* is necessary, however: Walin considered the flow response in a basin where the buoyancy field was taken to be horizontally uniform. In the Nordic Seas, on the other hand, strong lateral buoyancy gradients are encountered.

By making use of these assumptions, eq. (1) can be simplified as

$$H \frac{\partial}{\partial t} \oint_C \mathbf{u} \cdot \mathrm{d}\mathbf{s} = \frac{1}{\rho_0} \oint_C (\tau_\mathrm{w} - \tau_\mathrm{b}) \cdot \mathrm{d}\mathbf{s}. \tag{3}$$

[2]This term is related to divergence/convergence induced by the variation of f.

Next assume that the flow is geostrophic to lowest order, i.e.

$$\mathbf{u} = \frac{g}{f}\mathbf{k} \times \nabla\eta, \tag{4}$$

where $\mathbf{k}$ is the vertical unit vector. The free-surface height is decomposed as

$$\eta(x, y, t) = \overline{\eta}(H, t) + \eta'(x, y, t),$$

where η' is the free-surface height anomaly on the closed isobath $C(H)$ and $\overline{\eta}$ is the mean free-surface height defined as

$$\overline{\eta}(H, t) = \frac{1}{L}\oint_C \eta(x, y, t)\, \mathrm{d}s. \tag{5}$$

It is now assumed that the flow is aligned with the topography, i.e. $|\overline{\eta}| \gg |\eta'|$, implying that

$$\mathbf{u} \approx \frac{g}{f}\frac{\partial\overline{\eta}}{\partial H}\mathbf{k} \times \nabla H. \tag{6}$$

Using this result, it is found that

$$\oint_C \mathbf{u} \cdot \mathrm{d}\mathbf{s} = -\frac{g}{f}\frac{\partial\overline{\eta}}{\partial H}\oint_C |\nabla H|\, \mathrm{d}s. \tag{7}$$

A mean isobath-following velocity is now defined as

$$\overline{\mathcal{V}}(H, t) = -\frac{g}{fL(H)}\frac{\partial\overline{\eta}}{\partial H}\oint_C |\nabla H|\, \mathrm{d}s, \tag{8}$$

where $L(H)$ is the circumference length of $C(H)$.

To apply eq. (3), the bottom stress has to be specified. Here, the following linear relationship is used:

$$\tau_\mathrm{b} = \rho_0 u_* \mathbf{u}, \tag{9}$$

where u_* is a friction velocity. Hereafter eq. (3) can be formulated as

$$\frac{\partial\overline{\mathcal{V}}}{\partial t} + r\overline{\mathcal{V}} = \frac{1}{\rho_0 HL}\iint_A \mathrm{curl}\, \tau_\mathrm{w}\, \mathrm{d}A, \tag{10}$$

where $r = u_*/H$.

For notational convenience, when altimetric data is used to estimate the isobath-following velocity defined by eq. (8) it will be denoted $\overline{\mathcal{V}}_\mathrm{SLA}$. Furthermore, when wind-stress data are employed to solve eq. (10) the result will be denoted $\overline{\mathcal{V}}_\mathrm{w}$.

3 Data-set description

The present study, encompassing the years 1992–2004, makes use of two data sets from the Nordic Seas as well as from the north-eastern North Atlantic; the sea-surface height and the sea-level wind. The former of these data sets is based on satellite-altimetric measurements yielding anomalies from an average state, whereas the latter consists of wind data from a re-analysis based on an atmospheric weather forecast model.

The Sea-Level Anomalies (SLAs) were made available by the CLS Space Oceanography Division. They are assimilated from various satellite missions and are provided on a spatial grid better than 0.34×0.22 degrees and a temporal resolution of one week. Unfortunately there is a major data gap between January 1994 and March 1995 north of 67.8°N as well as minor *lacunae* scattered throughout the time series. Note that the effects of the data gaps have been taken into consideration when statistical techniques have been applied to this data set. It should also be pointed out that the SLAs comprise seasonal steric effects. These have not been eliminated since the spatial and temporal variations of the hydrography in the Nordic Seas are insufficiently known to permit this.

The wind data have been retrieved from the ERA-40 re-analysis project conducted by the European Center for Medium Range Weather Forecasts. They are provided in gridded form (0.5×0.5 degrees) with a temporal resolution of 6 hours.

Additionally a bathymetry with $5' \times 5'$ resolution assembled by the US National Geophysical Data Center has been used for the analyses.

4 Data analysis and results

The present investigation will focus on two regions: *Pro primo*, the part of the Norwegian Sea enclosed by the 2500-m isobath around Norwegian and Lofoten basins. *Pro secundo*, the region around the 500-m continental-slope isobath which starts at 67°N, transgresses the Svinøy section, and ends south-west of Ireland at 50°N. Both isobaths are shown in Fig. 1.

4.1 The Norwegian and Lofoten basins

Examining the spatial structure of the sea-surface height anomalies it was found (Mohammad et al., 2005) that these are strongly linked to the bathymetry. Conservation of potential vorticity constrains the flow to follow the contours of constant depth, the variation of f being negligible in the Nordic

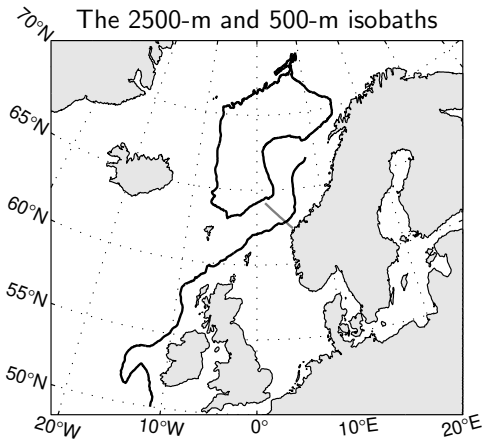

FIGURE 1: Map of the north-eastern Atlantic Ocean showing the closed 2500-m isobath encompassing the Norwegian and Lofoten basins as well as the 500-m isobath following the continental slope. The classical Svinøy section is indicated by a gray line.

Seas region. This state of affairs suggests that the theoretical framework presented in section 2 can be used to calculate the SLA distribution once the wind field is known. The present investigation has its focus on large-scale properties, leading us to disregard the small-scale variations associated with e.g. baroclinic instability (cf. Mysak and Schott, 1977). Therefore an attempt will here be made to use the isobath-following averaging method summarized by eq. (8) for isolating the large-scale variability from the raw SLA time series.

The forthcoming analysis will first deal with conditions along various depth contours enclosing the Lofoten and/or Norwegian basins. The locations of these isobaths were determined by applying horizontal interpolation to the $5' \times 5'$ gridded bathymetry, and SLA and wind data from as close as possible to these contours were used.

The two upper panels of Fig. 2 show the degree of spatial variation of the sea-surface height anomalies on two different closed isobaths (2600 m and 3100 m) in the Nordic Seas. The SLA time series pertaining to individual points on the isobaths show a significant degree of scatter around the isobath average $\overline{\eta}$. The variation of SLA between the individual points is large along the isobath girdling the Lofoten and Norwegian basins (cf. the

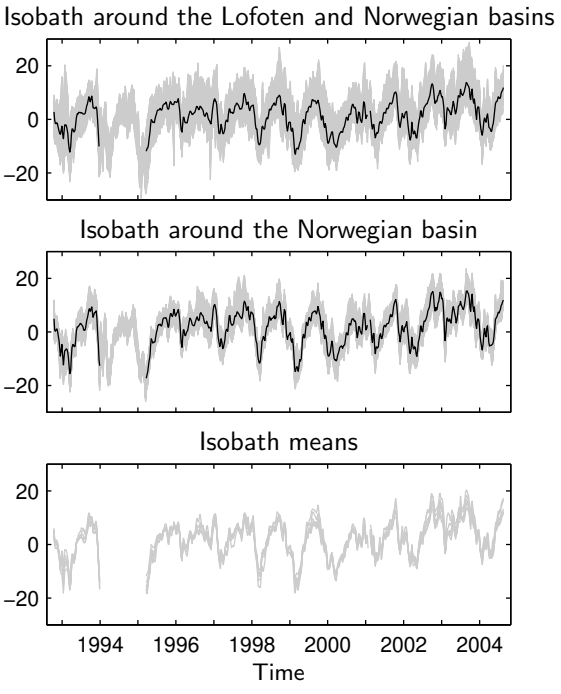

FIGURE 2: The SLA at each point along a closed isobath (gray) and the mean SLA of all points on the isobath (black) as functions of time. The upper panel pertains to the 2600-m isobath around both the Lofoten and Norwegian basins, the middle panel shows the results for the 3100-m isobath around the Lofoten basin. The bottom panel represents the isobath-averaged SLA for seven different closed isobaths in the Lofoten and Norwegian basins. The SLA is given in cm and the time in years.

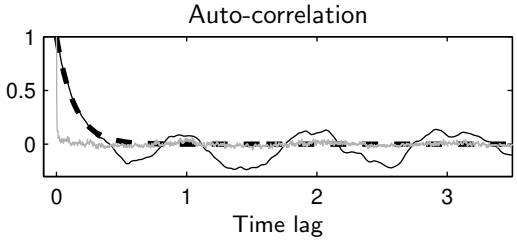

FIGURE 3: The normalized auto-correlations for $\overline{\mathcal{V}}_{\mathrm{SLA}}$ (black solid line) and the integrated wind stress curl in the Norwegian Sea (gray line). $\frac{\partial \overline{\eta}}{\partial H}$ evaluated using the 2500 and 3000-m isobaths. Both data sets have been detrended before calculating the auto-correlations. Additionally an exponential decay function with an e-folding time of 50 days is included in the diagram as a heavy dashed line. The time lag is given in years.

top panel in Fig. 2) as well as on the one encompassing only the Norwegian basin (cf. the middle panel in Fig. 2). Similar analyses undertaken for other closed isobaths in the Lofoten and/or Norwegian basins yielded the same results. In order to focus on large-scale properties it proved convenient to study the along-isobath SLA averages $\overline{\eta}$ (cf. the bottom panel of Fig. 2) which do not vary spatially to the same degree as do the results from individual contour points. Thus it has been concluded that the isobath-averaging method is capable of isolating a large-scale coherent signal from the SLA data.

In what follows focus will mainly be on the 2500-m isobath enclosing the Lofoten as well as the Norwegian basins. The averaged along-isobath velocity anomalies $\overline{\mathcal{V}}$ calculated from the SLA gradient and from the wind field using eq. (8) and eq. (10) will be compared. To do this it is, however, necessary to specify the damping parameter r, the choice of which is not trivial. To assess the magnitude of this quantity, the inherent damping time of the flow is estimated from a statistical analysis of the SLA data. Fig. 3 thus shows the normalized auto-correlation for the detrended $\overline{\mathcal{V}}_{\mathrm{SLA}}$ time series and also an exponential decay function with an e-folding time of 50 days. As seen there is good agreement for lags below three months between the auto-correlation of the SLA data and the decay function, which indicates that 50 days is a realistic damping time-scale (in turn yielding $r \approx 1/50$ days^{-1}). Since the diagram additionally includes the auto-correlation of the surface wind stress, it can be recognized that the "memory" of the wind field is rather short compared to that of the sea-surface height field, this since the characteristic meteorological damping time-scale is on the order of one day. Note, furthermore, that in these

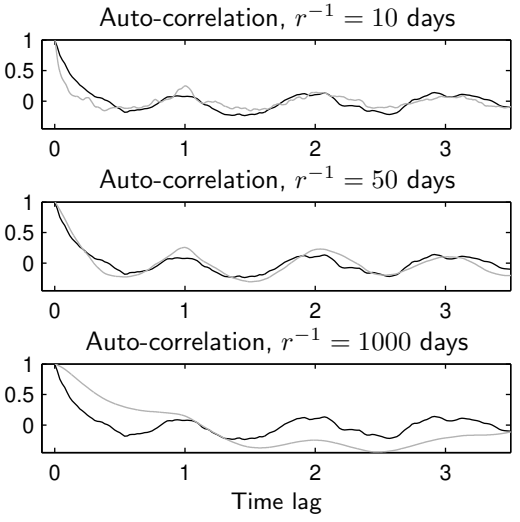

FIGURE 4: Normalized auto-correlations for $\overline{\mathcal{V}}_{\mathrm{SLA}}$ (black) and $\overline{\mathcal{V}}_{\mathrm{w}}$ (gray) in the Norwegian Sea. The data have been detrended before calculating the auto-correlations. The upper, middle and lower panels show $\overline{\mathcal{V}}_{\mathrm{w}}$ as the solution of eq. (10) for $r^{-1} = 10$, 50, and 1000 days, respectively. The time lag is given in years.

latter auto-correlation results, the atmospheric seasonal cycle is submerged by high-frequency noise. It, however, becomes manifest when this auto-correlation instead is calculated from the low-passed time series, this since the energy of the seasonal cycle, although being of narrow-band character, is one order of magnitude larger then the rest of the frequency-domain power spectrum.

If a linear differential equation of type (10) is solved with white-noise forcing, the auto-correlation of the solution proves to be an exponential function of the form e^{-rt}. Since the wind data have white-noise characteristics, $\overline{\mathcal{V}}_{\mathrm{w}}$ is expected to decay exponentially with an e-folding time r. Comparing (cf. Fig. 4) the auto-correlation of $\overline{\mathcal{V}}_{\mathrm{SLA}}$ with that of $\overline{\mathcal{V}}_{\mathrm{w}}$ obtained from eq. (10) for different values of r, the optimal damping time-scale is found to be on the order of 50 days. It may be noted that this choice of r is consonant with the estimated linear bottom drag coefficient employed by Isachsen et al. (2003).

At this stage the results estimated from eqs. (8) and (eq. 10) can be compared. Here this is done on the 2500-m isobath girdling the Lofoten

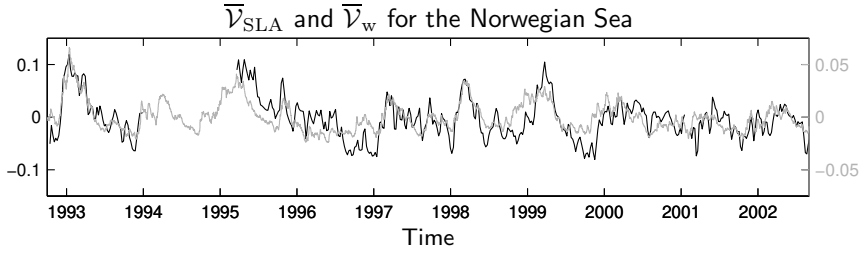

FIGURE 5: Isobath-averaged velocities $\overline{\mathcal{V}}_{\mathrm{SLA}}$ (black) and $\overline{\mathcal{V}}_{\mathrm{w}}$ (gray) in the Norwegian Sea. The velocities are in m/s and calculated using SLA data from the 2500- and 3000-m isobaths (cf. eq. 8) and wind data (cf. eq. 10), respectively, taking r^{-1} to be 50 days. The scales of $\overline{\mathcal{V}}_{\mathrm{SLA}}$ and $\overline{\mathcal{V}}_{\mathrm{w}}$ are on the left- and right-hand vertical axes, respectively. The time is given in years.

and Norwegian basins. When evaluating eq. (8), $\frac{\partial\overline{\eta}}{\partial H}$ is discretized using the difference between the isobath-averaged SLAs on the isobaths of 2500- and 3000-m divided by 500 m. (Although focus is on conditions along the 2500-m isobath, this choice of interval for estimating the derivative was dictated by the insufficient resolution of the SLA data sets.) This velocity is to be compared to the one obtained from the linear differential equation (10) using the wind data. When solving eq. (10), its right-hand member is evaluated by integrating the wind-stress anomalies over the area confined within the 2500-m isobath and furthermore the damping parameter r is taken to be $1/50$ days^{-1}.

Fig. 5 shows the resulting isobath-following means of the velocity anomalies $\overline{\mathcal{V}}_{\mathrm{SLA}}$ and $\overline{\mathcal{V}}_{\mathrm{w}}$. Although the low-frequency variations of the two time series are seen to be essentially the same, the amplitudes differ by factor of two. This discrepancy can have a number of causes, the most likely ones being steric and baroclinic effects. Other possible reasons are the estimate of r, the discretization of $\frac{\partial\overline{\eta}}{\partial H}$, and the grid resolution of the SLA and wind fields (particularly in regions with steep bathymetry). It may furthermore be noted that the variations of the SLA-based time series are more pronounced than those of the wind-based series, since applying the linear differential equation (10) curtails the high frequencies inherent in the time series of the integrated wind stress.

The overall conclusion to be drawn from these analyses is, nevertheless, that the Norwegian-Sea re-circulation gyre is predominantly forced by local wind stress.

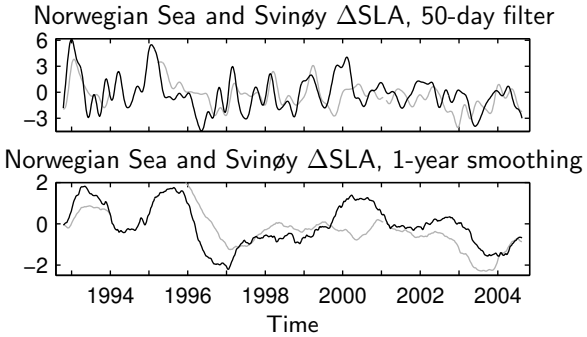

FIGURE 6: Isobath-averaged SLA difference for the Svinøy transect (black) and in the central Norwegian Sea (gray). For the Svinøy transect the isobath-averages along the 500- and 1000-m isobaths between 61°N and 67°N have been used, whereas the results for the central Norwegian Sea are based on the closed 2500- and 3000-m isobaths. In the upper panel the data have been low-passed using a Butterworth filter with a 50-day cut-off, whereas in the lower panel 1-year running means have been applied. The SLA differences are given in cm and the time in years.

4.2 The Svinøy section

After having studied the region with closed depth contours in the central parts of the Norwegian Sea, focus will now be on the Svinøy section (cf. Fig. 1) where the Norwegian Atlantic Slope Current (NwASC) is located over the depth interval 300–800 m (Skagseth, 2004), i.e. well separated from the previously discussed central circulation gyre. It should be noted that here the isobaths shallower than ∼700 m extend into the Atlantic proper via the Faroe-Shetland channel. The NwASC is part of an almost-barotropic shelf-edge current system extending from the Irish-Scottish shelf to the Fram Strait. Observations show that the low-frequency temporal variations of this slope current tend to be coherent along its entire stretch (Skagseth et al., 2004). Furthermore, it can be noted that the low-frequent variability of NwASC in the Svinøy section exhibits a spatial coherence in the cross-stream direction (Orvik and Skagseth, 2003b).

Based on the observational characteristics presented above, it is anticipated that the NwASC should to some extent be influenced by remote conditions in the Atlantic. To investigate this matter, the variability of the NwASC will first be compared to that of the interior re-circulation in the Norwegian Sea. For this purpose an altimetry-based proxy of the NwASC is constructed. Specifically, the SLA difference between the 500-

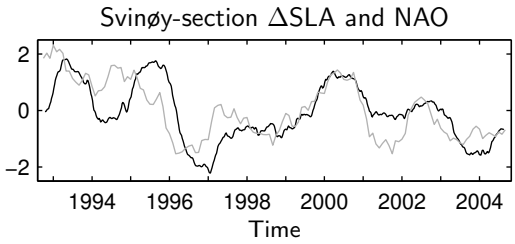

FIGURE 7: Isobath-averaged SLA difference for the Svinøy transect (black) and the NAO index (gray). The Svinøy-transect SLA difference was calculated as in Fig. 6. Both time series normalized with their standard deviations and smoothed with 1-year running means. The time is given in years.

and 1000-m isobaths is used to characterize the flow strength. Note that to eliminate the small-scale high-frequency variability, along-isobath averaging has been undertaken over a distance extending some 500 km on each side of the Svinøy section. The instrumentality of this proxy was estimated by comparing with the direct current measurements in the Svinøy section reported by Orvik and Skagseth (2003a). The two data sets were found to be in general correspondence, although the altimetric proxy, due to the limited spatial resolution, fails to reproduce the full details of the current-meter records, e.g. the pronounced transport peak registered in early 2002.

Fig. 6 thus shows low-passed time series of the Norwegian-Sea and the Svinøy-transect SLA differences. From this graph it is seen that there are periods when the flow on the closed isobaths co-varies with the flow on the isobaths communicating with the Atlantic. However, and perhaps more significantly, there are also instances when the flow variabilities appear to be decoupled. This behavior could indicate changes of the circulation in the Norwegian Sea. Shifts of this type are, most likely, associated with changes of the large-scale wind forcing.

To further pursue these notions, the extent to which the altimetric proxy for the NwASC co-varies with the large-scale wind forcing affecting the North Atlantic is investigated. Focus is initially on the North Atlantic Oscillation (NAO) index, reflecting the basin-scale atmospheric flow (Hurrell, 1995). As shown in Fig. 7, there is fair degree of correspondence between the time evolution of the altimetric NwASC proxy and the NAO index, particularly the latter part of the period under consideration. (Similar conclusions have previously been drawn by Skagseth et al. (2004) on the basis of a comparison between altimetric PCs and surface-pressure EOFs.) This indicates that the NwASC is subjected to non-local influences from the atmospheric conditions prevailing over the northern North Atlantic Ocean.

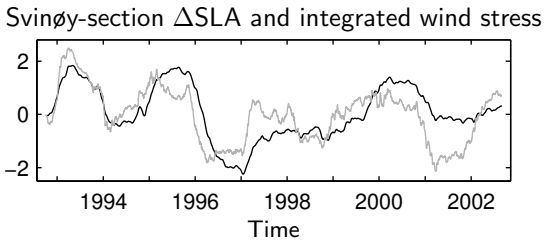

FIGURE 8: Isobath-averaged SLA difference for the Svinøy transect (black) and the integrated wind stress (gray) along the 500-m isobath from 50°N (south-west off Ireland) to 67°N (north-west off the Svinøy transect). The Svinøy SLA difference is calculated as in Fig. 6. Both data sets are normalized with their standard deviations and smoothed with 1-year running means. The time is given in years.

Next, some tentative ideas having their roots in the theoretical framework pertaining to along-isobath flow (cf. section 2) will be examined, this as an attempt to relate the NwASC variability to the characteristics of the wind forcing. It must be emphasized that closed isobaths are at the heart of the analytical model derived in section 2. However, it can be expected that also on open isobaths, there will be some degree of correspondence between the flow and the along-isobath wind stress. The underlying physics are that steep topography forces the flow to be nearly parallel with the isobaths. As a consequence, the along-isobath momentum equation is anticipated to entail an approximate balance between the wind- and bottom-stress, at least when averaged along the continental slope. It should further be noted that it is the wind stress acting upstream (defined in a topographic-wave propagation sense) that is of relevance here. To test these qualitative considerations, a time series is constructed from the wind stress, integrated along the 500-m isobath from 50°N to 67°N, viz. from south of the British Isles to the Svinøy section. This is compared to the altimetric proxy for the NwASC in Fig. 8, where 1-year running means have been applied to the data sets. There is a fair degree of agreement between the two time series, where it may be noted that during the early part of the observational period, the correspondence is better than that between the NwASC proxy and the NAO in Fig. 7.

It may finally be remarked that Orvik and Skagseth (2003a) found a significant degree of lagged coherence between current-meter records of the NwASC and the zonally integrated wind stress curl over the North Atlantic at 55°N. Although Skagseth et al. (2004) concluded that the altimetric data do not exhibit this coherence (presumably due to baroclinic effects and the

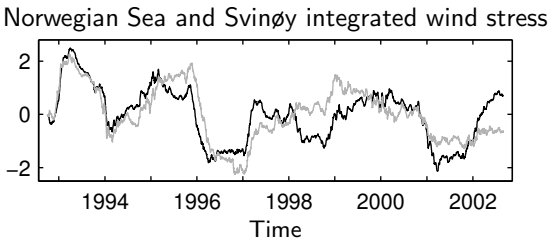

FIGURE 9: Integrated wind stress along the eastern boundary (black) and in the central Norwegian Sea (gray). The data sets are normalized with their standard deviations and 1-year running means have been applied. The time is given in years.

limited resolution of the altimetric data), the present results indicate that an alternative representation of the more-or-less remotely acting wind stress may serve to cast some doubts on this inference.

5 Discussion

The present study has examined low-frequency flow variability in the Norwegian Sea on the basis of satellite altimetry. To facilitate a physical interpretation of the altimetry data, a linear model has been employed to estimate the wind-forced variability on closed isobaths in the central Norwegian Sea. Moreover, the flow features along these closed isobaths have been compared to those characterizing the NwASC in the Svinøy section. It deserves to be re-iterated that the NwASC is located over isobaths that are open, viz. extend into the Atlantic proper. While there exists a relatively straightforward theory for wind-forced flows on closed isobaths, no such relation is available for flows on open isobaths, where a generalized Sverdrup relation determines the along-isobath pressure variations (Skagseth, 2004). It is, however, difficult to derive an appropriate upstream boundary condition corresponding to the eastern boundary condition in Sverdrup's classical analysis. Nevertheless, elementary dynamical considerations suggest that the strength of NwASC should be influenced in a non-local fashion by the wind stress acting along the continental slope in the north-eastern Atlantic.

Thus, the wind-driven variability of the NwASC and the re-circulating gyre in the Norwegian Sea are expected to be forced from different geographical regions. The question then is whether the present analysis serves to corroborate this view. To begin with, the altimetric data demonstrate

that the flow on the closed isobaths to some extent is decoupled from that on the open isobaths extending into the Atlantic. However, it is by no means obvious that this decoupling is attributable to a difference of the underlying wind-forcing patterns. To further pursue this question it is relevant to examine Fig. 9, showing the time evolution of the abovementioned eastern-boundary wind stress and the central Norwegian Sea wind-stress curl. As can be seen, there are instances when even the signs of these wind-stress indices differ. Accordingly, the atmospheric circulation over the central Norwegian Sea is to some extent a regional phenomenon, which is not entirely governed by the large-scale conditions prevailing over the North Atlantic. Overall, this state of affairs appears to support the view that the partial decoupling of the NwASC and the re-circulation gyre is a manifestation of a difference between the forcing wind-stress fields. However, it should be noted that there seems to be no straightforward relation between the decoupling of these wind stresses and the decoupling of the two flow branches.

It must be underlined that although the NwASC is predominantly a barotropic phenomenon, it is also affected by baroclinic features such as the stratification in the north-eastern North Atlantic (Orvik and Skagseth, 2003a; Nilsson et al., 2005). It is expected that variations of the wind forcing give rise to a nearly instantaneous barotropic response of the NwASC, whereas the impact of baroclinic changes may demonstrate a considerable time-lag, e.g. reflecting advection of buoyancy anomalies along the continental slope (Furevik, 2001). Thus it is not only disjunct wind-stress forcing which may cause the NwASC and the re-circulating gyre to evolve in an independent manner.

One may speculate that alterations of the hydrographic conditions along the continental slope contribute to the partial decoupling of the times series displayed in Fig. 8: Initially, the integrated eastern-boundary wind stress and the NwASC proxy evolve in concert, while the two time series are less coherent towards the end of observational period. If the eastern-boundary wind stress would be the main agent forcing the NwASC, one anticipates that the good correlation between the two time series would persist throughout the entire period. Consequently, this behavior may reflect interannual variability of the hydrography in the north-eastern North Atlantic. It is interesting to note that the correlation between the NAO index and the NwASC proxy tended to increase after 1998, cf. Fig. 7. This state of affairs furthermore underscores that the relation between the atmospheric forcing and the flow along the open isobaths in the Nordic Seas is far from straightforward.

Keeping in this *caveat* in mind, it can nevertheless be concluded that the present results, although not immediately useful for predictive purposes, show that fundamental dynamical questions can be addressed using altimetric techniques.

Acknowledgments

The work herein reported was undertaken on the basis of a grant from the Swedish National Space Board. The altimeter products were made available by the CLS Space Oceanography Division as part of the Environment and Climate EU ENACT project (EVK2-CT2001-00117) and with support from CNES. I would also like to thank to Peter Sigray for valuable discussions and comments concerning signal processing.

Appendix

Here an outline of the derivation of the theoretical results presented in section 2 is provided. Essentially, the results due to Nilsson et al. (2005) are generalized by allowing for time-dependent flow and a variable Coriolis parameter. The linear dynamics of a rotating stratified fluid in the hydrostatic limit are considered. It is assumed that viscous effects are confined to thin Ekman boundary layers adjacent to the bottom and the free surface. The vertically integrated continuity equation can be written as

$$\frac{\partial \eta}{\partial t} = -\nabla \cdot \mathbf{U} - \nabla \cdot (\mathbf{m}_w + \mathbf{m}_b), \tag{11}$$

where η is the free surface, $\mathbf{U}$ the vertically-integrated flow and $\mathbf{m}_w$ and $\mathbf{m}_b$ are the boundary layer transports in the top and the bottom Ekman layers, respectively. Note that

$$\mathbf{U} = \int_{-H}^{0} \mathbf{u}\, \mathrm{d}z,$$

where $\mathbf{u} = (u, v)$ is the horizontal velocity component. The Ekman boundary layer transports are related to the surface wind stress τ_w and the bottom stress τ_b according to $\mathbf{m}_w = -\mathbf{k} \times \tau_w/(\rho_r f)$, $\mathbf{m}_b = \mathbf{k} \times \tau_b/(\rho_r f)$ (e.g. Pedlosky, 1987).

The hydrostatic equation is given by

$$\frac{\partial p}{\partial z} = -g\rho_r(1 - q), \tag{12}$$

where g is the acceleration of gravity, ρ_r the deep water density, and q the density anomaly. By integrating the hydrostatic equation upwards from the bottom, one obtains (Nilsson et al., 2005)

$$p(x,y,z,t) = g\rho_r \int_{-H}^{z} q \,\mathrm{d}z + p_0(x,y,t) - g\rho_r z. \tag{13}$$

Here, $H(x,y)$ is the basin depth and p_0 is a barotropic pressure anomaly, defined as $p_0(x,y) = p_b(x,y) - g\rho_r H$, where p_b is the bottom pressure. The linearized surface pressure is given by $p(z=0) = g\rho_r\eta$. Thus, eq. (13) leads to the relation

$$\eta(x,y,t) = \int_{-H}^{0} q \,\mathrm{d}z + p_0/(g\rho_r), \tag{14}$$

where the first term on the right-hand side is known as the steric height anomaly and the second one is the contribution to sea-surface height due to the barotropic pressure anomaly p_0. The notation $\eta = \eta_q + \eta_0$ is introduced, where

$$\eta_q = \int_{-H}^{0} q \,\mathrm{d}z, \;\; \eta_0 = p_0/(g\rho_r). \tag{15}$$

The vertically-integrated momentum equation, pertaining to the inviscid flow outside the Ekman layer, can be written as

$$\frac{\partial \mathbf{U}}{\partial t} + f\mathbf{k}\times\mathbf{U} = -{\rho_r}^{-1} H \nabla p_0 - \nabla Q, \tag{16}$$

where Q is the potential energy anomaly (see eq. 2). By dividing eq. (16) with f and integrating around a closed curve C, on which H/f is constant, one obtains

$$\frac{\partial}{\partial t}\oint_C \frac{\mathbf{U}}{f}\cdot\mathrm{d}\mathbf{s} + \oint_C \mathbf{U}\cdot\mathbf{n}\,\mathrm{d}s = -\oint_C \frac{\nabla Q}{f}\cdot\mathrm{d}\mathbf{s}. \tag{17}$$

Combining this result with the continuity equation yields

$$\frac{\partial}{\partial t}\iint_A \eta \,\mathrm{d}A = \frac{\partial}{\partial t}\oint_C \frac{\mathbf{U}}{f}\cdot\mathrm{d}\mathbf{s} + \oint_C \frac{\nabla Q}{f}\cdot\mathrm{d}\mathbf{s} - \oint_C (\mathbf{m}_w + \mathbf{m}_b)\cdot\mathbf{n}\mathrm{d}s \tag{18}$$

By making use of the three main approximations discussed in section 2, straightforward calculations yield

$$\frac{\partial}{\partial t}\oint_C \mathbf{U}\cdot\mathrm{d}\mathbf{s} + u_*\oint_C \mathbf{u}_b\cdot\mathrm{d}\mathbf{s} = \frac{1}{\rho_r}\iint_A \mathrm{curl}\,\tau_w \,\mathrm{d}A,$$

where $\mathbf{u}_b$ is the bottom velocity. Note that the Stokes theorem has been used here and that the boundary-layer transports $\mathbf{m}_w$ and $\mathbf{m}_b$ have been been rewritten in terms of the stresses. As a next step, it is assumed that the flow to leading order is in geostrophic balance. By using eq. (13), one obtains

$$\mathbf{u} = \frac{g}{f}\mathbf{k} \times \nabla_h \int_{-H}^{z} q \, \mathrm{d}z + \mathbf{u}_0, \tag{19}$$

where

$$\mathbf{u}_0 = \frac{1}{f\rho_r} \, \mathbf{k} \times \nabla p_0.$$

By integrating eq. (19) vertically over the entire water column, one obtains

$$\mathbf{U} = \frac{1}{f}\mathbf{k} \times \nabla Q + H\mathbf{u}_0. \tag{20}$$

If the bottom buoyancy is essentially constant along the isobaths (a reasonable assumption for the closed isobaths in the Norwegian Sea), then $\mathbf{u}_b \approx \mathbf{u}_0$ (Nilsson et al., 2005). Using this and the expression for the geostrophic flow, the integral relation can be written as

$$\frac{\partial}{\partial t} \oint_C \mathbf{u}_0 \cdot \mathrm{d}\mathbf{s} + r \oint_C \mathbf{u}_0 \cdot \mathrm{d}\mathbf{s} = F \tag{21}$$

where

$$F = -\frac{1}{fH}\frac{\partial}{\partial t} \oint_C \mathbf{n} \cdot \nabla Q \, \mathrm{d}s + \frac{1}{H\rho_r} \iint_A \operatorname{curl} \tau_w \, \mathrm{d}A.$$

To judge the relative importance of the two terms in the forcing function F, the estimate of the seasonal variation of Q/f in the Nordic Seas presented by Mohammad et al. (2005) is utilized. Their Fig. 5 shows that the seasonal cycle of Q/f is on the order of 5 Sv. In combination with the integrated wind-stress data, this yields the following rough estimate:

$$\frac{1}{f}\frac{\partial}{\partial t} \oint_C \mathbf{n} \cdot \nabla Q \, \mathrm{d}s \cdot \left(\frac{1}{\rho_r} \iint_A \operatorname{curl} \tau_w \, \mathrm{d}A \right)^{-1} \approx 0.1.$$

Provided that the approximations made here provide the leading-order picture of the flow, eq. (10) can now be used to estimate the contribution of the sea-surface height anomaly related to η_0. It must be recognized, however, that the total sea-surface height anomaly is given as $\eta = \eta_0 + \eta_q$.

Bibliography

Furevik, T., 2001. Annual and interannual variability of Atlantic water temperatures in the Norwegian and Barents Seas: 1980–1996. Deep Sea Research Part I 48 (2), 383–404, doi:10.1016/S0967-0637(00)00050-9.

Gill, A. E., 1982. Atmosphere-ocean dynamics. Vol. 30 of International geophysics series. Academic Press, Inc.

Helland-Hansen, B., Nansen, F., 1909. The Norwegian Sea, its physical oceanography. based on the Norwegian researches 1900–1904. Report on Norwegian fishery and marine investigations 2 (2), 1–359.

Hurrell, J. W., 1995. Decadal trends in the North Atlantic Oscillation: Regional temperatures and precipitation. Science 269, 676–679.

Isachsen, P. E., LaCasce, J. H., Mauritzen, C., Häkkinen, S., 2003. Wind-driven variability of the large-scale recirculating flow in the Nordic Seas and Arctic Ocean. Journal of Physical Oceanography 33 (12), 2534–2550, doi:10.1175/1520-0485(2003)033<2534:WVOTLR>2.0.CO;2.

Mohammad, R., Nilsson, J., Lundberg, P., 2005. An altimetric study of the nordic-sea region seasonal cycle, submitted to Deep Sea Research Part I.

Mysak, L. A., Schott, F., 1977. Evidence for baroclinic instability of the norwegian current. Journal of Geophysical Research 82 (C15), 2087–2095.

Nilsson, J., Broström, G., Walin, G., 2005. Steady f-plane circulation arising from a prescribed buoyancy distribution in basins with sloping boundaries; or the role of bottom friction for creating a thermohaline circulation, submitted to Journal of Marine Research.

Nøst, O., Isachsen, P., 2003. The large-scale time-mean ocean circulation in the Nordic Seas and Arctic Ocean estimated from simplified dynamics. Journal of Marine Research 61 (2), 175–210, doi:10.1357/002224003322005069.

Orvik, K. A., Skagseth, Ø., 2003a. The impact of the wind stress curl in the North Atlantic on the Atlantic inflow to the Norwegian Sea toward the Arctic. Geophysical Research Letters 30 (17), 1884, doi:10.1029/2003GL017932.

Orvik, K. A., Skagseth, Ø., 2003b. Monitoring the Norwegian Atlantic Slope Current using a single moored current meter. Continental Shelf Research 23 (2), 159–176, doi:10.1016/S0278-4343(02)00172-3.

Pedlosky, J., 1987. Geophysical Fluid Dynamics, 2nd Edition. Springer-Verlag.

Skagseth, Ø., 2004. Monthly to annual variability of the Norwegian Atlantic Slope Current: Connection between the northern North Atlantic and the Norwegian Sea. Deep-Sea Research Part I 51 (3), 349–366, doi:10.1016/j.dsr.2003.10.014.

Skagseth, Ø., Orvik, K. A., Furevik, T., 2004. Coherent variability of the Norwegian Atlantic Slope Current derived from TOPEX/ERS altimeter data. Geophysical Research Letters 31, doi:10.1029/2004GL020057.

Walin, G., 1972. On the hydrographic response to transient meteorological disturbances. Tellus 24, 169–186.